# Optimization of Optical Tissue Clearing Protocols

Dekan: Prof. Dr. med. Sergij Goerdt
Referent: Prof. Dr. med. Norbert Gretz

# Table of Contents

Table of Contents

# Introduction

Optical Tissue Clearing (OTC) refers to a wide set of techniques aiming to make large and fixed biological tissues optically transparent. The meaning of "large" is related to thick sections of tissue, organoids, up to whole organs or organisms (for example, entire mouse or rat)[1]. The increasing need of a deeper understanding of morphogenetic and developmental processes, in organs and whole organisms, has been leading biologists to push the research for establishing methodologies related to volumetric imaging[2]. In this background, many researches and testing have been done, for very long time, only on brain, in order to reconstruct the neuronal connections and understand the mechanisms of development[3].

Moreover, the three dimensional (3D) imaging has been more and more often required also in medical and diagnostic fields, to overcome the limitations of the two dimensional (2D) structural analysis, performed on thin sections (in the range of a few μm) of biological material. A small portion, in fact, could provide only little structural information and, additionally, the spatial resolution is a very limiting factor (Spatial resolution: number of pixels used for image reconstruction. Usually, a higher spatial resolution image corresponds to a greater number of pixels)[2, 4]. In order to obtain 3D information, different approaches have been described, such as serial sectioning of samples, followed by volumetric reconstruction[5, 6] or the "blockface" approach which involves the imaging of the surface of a block of tissue, followed by a sequential shaving of the surface itself[7, 8]. In reality, these options are highly labor-intensive and the 3D reconstruction is extremely cumbersome and prone to error. The third alternative is to image the volume without tissue slicing, accelerating, in this way, all the process and preventing also all the inaccuracies resulting from the sectioning. In theory, this could be possible by using confocal, light sheet or multiphoton microscopies. However, the more focus goes in depth, the more the quality of the imaging deteriorates incredibly[1]. This is mainly due to the lack of transparency of biological samples that is related to many factors. The first is the tissue composition and the phenomenon of light scattering. This occurs whenever light, after being absorbed by a medium, does not travel in straight lines, as theoretically it should do, but rather it is deviated and reflected by the components of the medium[2]. Tissues are, in fact, mixtures of different biomolecules, differing to each other for many properties and among them there is the refractive index (RI), defined as how much slow the light propagates through a certain medium, compared to the vacuum[1]. All the biomolecules are characterized by specific RI values[4]: proteins RI~1.43; lipids RI~1.44; water RI~1.33, where the overall tissue RI is generally set equal to 1.4-1.5[9, 10]. Moreover, many

pigments confer an overall tissue colouration, as haemoglobin in the blood circulation, myoglobin in the skeletal muscle and melanin, which is the primary pigment in hair and skin[2]. Due to their chemical structure, this set of molecules is considered as the main responsible of visible light absorption in tissue[2]. Another additional trouble regards intrinsic fluorescent molecules, involved in arising tissue autofluorescence up and, in the same time, masking the fluorescent signal from external labelling. This is the case with NaDPH, collagen, flavins or molecules introduced by the formation of Schiff's bases, caused by fixation with aldehydes[2]. Collectively, all of these components create a lack of homogeneity in tissue, resulting in a milky and opaque appearance of the tissue itself[2]. Moreover, the consequent RI mismatch, occurring within the tissue, does not allow light pass through the sample and this negatively influences the 3D imaging. One example is the spherical aberration, which is a type of image degradation, resolving in sharp and unclear images. This happens whenever the matching of RIs between sample, mounting solution and objective lens fails[2]. Considering this context, OTC, combined to 3D imaging is the optimal solution, providing many benefits to the modern biology. Of course, OTCs could not completely remove the light scattering phenomenon, but they can, anyway, minimize that. In fact, the general strategy of OTCs is to homogenize the RI of a sample, by removing or replacing the components providing the highest rate of light scattering from the tissue, in order to make that optically transparent and give, in this way, a better transition of light and, consequently, a final volumetric imaging[1]. Due to their high RI and their tendency to create aggregates (principal cause of the tissue milky appearance), lipids from cells membrane bilayers are defined as the major source of light scattering and, therefore, the main component removed or solvated by OTCs[9]. However, prior to any OTC method, perfusion to remove blood (and, therefore, haemoglobin) is often required. Whenever this could not be an option, other techniques may be used, as, for instance, hydrogen peroxide to de-colour haemoglobin[2].

## 1.1 Different OTCs techniques for large samples

The pioneer of OTC is considered to be Walter Spalteholz, who, in 1914, had developed a mixture of benzyl alcohol and methyl salicylate to clear large samples[11].

Nowadays, OTCs are grouped into three different categories, based on their mode of action[1, 2, 4]: 1) simple RI matching; 2) delipidation and dehydration/hyperhydration followed by RI matching; 3) tissue-gel hybridization followed by delipidation and RI matching.

Figure 1.1 represents a schematic overview of all the OTCs described until 2016.
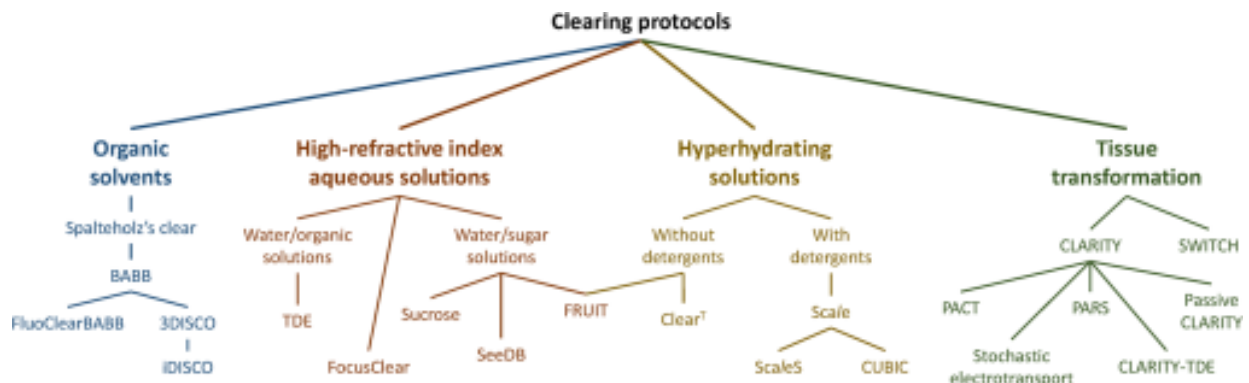
**Figure 1.1**: Schematic overview of all the OTC techniques updates until 2016. Image taken from[12].

## SIMPLE IMMERSION AND RI MATCHING

The specimens to be cleared are immersed in high RI solutions, which diffuse passively into them, without delipidation[2]. Many clearing solutions have been described and these act mainly by replacing water, allowing the clearing as well as the RI matching [2, 4]. Moreover, the majority of them are characterized by a quite high RI, in a range between 1.44-1.49[4]. Examples are sucrose, fructose (SeeDB technique), glycerol and formamide[7, 13-16]. These solutions are easy to implement, economic and the process is totally reversible[2, 4]. On the other hand, the clearing efficacy is not so high and this clearing is obtained after a long time of incubation. In addition, due to their high viscosity, there is the risk of their precipitation at room temperature (RT) and incorporation of air bubbles[2]. Another drawback regards how these retain fluorescent molecules: for instance, since the formamide destroys the fluorophores, it may easily quench the signal from the inherent fluorescent proteins (FPs)[4]. Therefore, in order to overcome these limitations and to lower the viscosity of the previous solutions, new solutions have been created, as FocusClear[TM], Refractive Index Matching Solution (RIMS) or FRUIT (a mixture of urea and fructose); in particular, the latter as replacement of the first SeeDB solution, to overcome its limitations[17-20].

## DELIPIDATION AND DEHYDRATION/HYPERHYDRATION FOLLOWED BY RI MATCHING

These methods are based either on high RI (~1.56) organic solvent or on aqueous solutions: these latters work to lower the overall RI of the tissue, to ~1.38[1, 4]. In both cases, the optical transparency and the RI matching are achieved.

Organic solvents work by removing and/or solvating lipids. In terms of speed and efficacy of clearing, these techniques are better than the aqueous solutions[4]. On the other hand, the tissue

shrinkage caused by the dehydration prior to the clearing (for example by using increasing series of alcohol, as methanol or ethanol) might provoke an important shrinkage of the tissue and, consequently, decrease quality of the final imaging, despite the advantage of imaging a large volume more easily[2]. Additionally, in many cases, a little retention of the fluorescent signal has been observed: for instance, after performing 3DISCO, which uses a dibenzyl ether (DBE) and tetrahydrofuran (THF), a survival of the green fluorescent protein (GFP) of only 1,2 days has been noticed[21]. Moreover, the toxicity of the used substances is another disadvantage. On the other hand, aqueous solution also remove lipids, but with less toxicity and quenching issues. Although they might damage the tissue by hyperhydration, the main benefits of these substances are the ease of implementation and the reduced harmfulness[1, 2, 4]. Some examples are given by Triton X-100 (non-ionic detergent), urea (denaturant), which are used, for example, in CUBIC (Clear, Unobstructed Brain/Body Imaging Cocktails and Computational analysis) or Sca*l*eA2 (glycerol combined to urea and Triton)[22, 23].

## TISSUE-GEL HYBRIDIZATION FOLLOWED BY DELIPIDATION AND RI MATCHING

To protect the biomolecules that could be lost with the use of stringent concentrations of organic solvents or detergents, some other techniques have been described. These include the use of tissue embedding in tissue gel, followed by delipidation and, then, by incubation in a RI matching solution. This is the case with CLARITY (Clear Lipid-exchange Acrylamide-hybridized Rigid imaging in situ hybridization-compatible Tissue Hydrogel)[24]: here, tissues are embedded in a mixture of acrylamide and bis-acrylamide, delipidation is performed by sodium dodecyl sulphate (SDS) and RI matching in RIMS contributes to clear the whole organ. The delipidation could be achieved either by passive incubation in SDS (for some weeks[25]) or by electrophoresis[24]. Thanks to the primary embedding, the protein structures are well preserved, as well as the fluorescence from intrinsic and extrinsic molecules.

In summary, the choice of the most correct OTC methodology is really important to prevent a premature FPs quenching[26]. In fact, solvent based clearing, as BABB (Benzyl Alcohol/ Benzyl Benzoate), iDISCO or 3DISCO (<u>DISCO</u>: dimensional imaging of solvent-cleared organs) can easily quench the fluorescence, differently from aqueous clearing solutions, as many FPs need a hydrophilic environment to fluoresce[26]. This is the reason why, in order to maintain the fluorescent signal (for example from immunofluorescent labels) for a longer time, for some organic clearing solution a pre-treatment is often required[26], whereas the

fluorescence survival has been clearly demonstrated in aqueous based techniques, as CLARITY, PACT (Passive Clarity technique); SeeDB, immunofluorescent labeling[2, 4, 26].
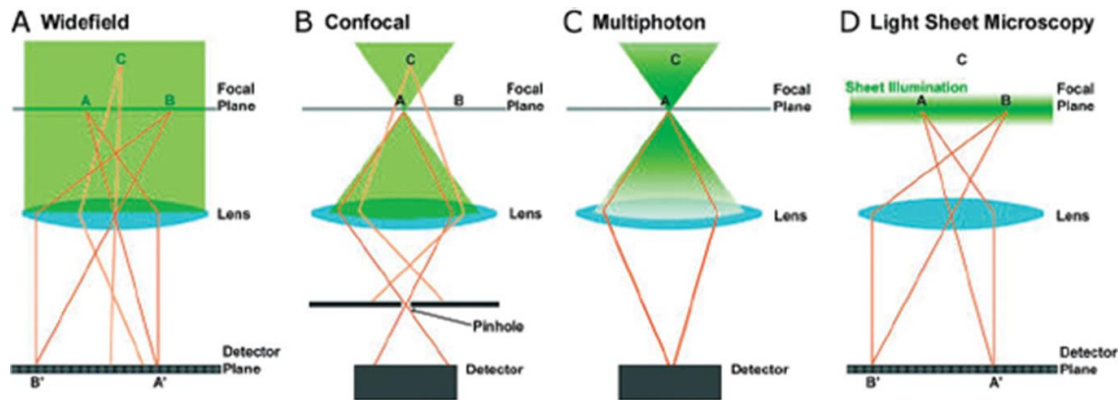
## 1.2 Microscopy

The detection of fluorescent signals has always been a great tool for tracking proteins in living cells. Although many and different microscopies have been used for the 2D visualization, with the advent and the increasing request of volumetric imaging and OTCs, fluorescence microscopy has been growing more and more in importance[26, 27].

Basically, a fluorescent microscope is strictly related to the mode of action of fluorophores (Fluorophore: molecule able to re-emit light after absorbing it. Usually, fluorophores contain aromatic rings and groups and are characterized by many $\pi$ bonds[28]). These are molecules that absorb a specific wavelength and, because of that, the electrons are promoted to a higher electron energy state. After a range of time between 1 and 100 ns, these electrons return to their stationary state and emit a longer wavelength known as fluorescence[27]. So, a simple fluorescent microscope is characterized by: 1) a light source that allows the molecules to fluoresce (most common: mercury lamp; more advanced: lasers); 2) excitation filter, selecting the excitation wavelength from the light source; 3) dichroic mirror, which separates the excitation and emission light; 4) emission filter, that directs light into the 5) detector, which diffuses the light to the sample[27, 29, 30]. Many types of fluorescent microscopes exist. They are classified on the bases of how the light hits the sample[27]. One of the most common is the wide-field microscope (WFM), where the excitation light hits the whole sample and the fluorescence could be visible through the oculars (Fig.1.2 A). Moreover, it would also be possible to post-process the final image by deconvoluting it, bringing further ameliorations[27]. Indeed, to deal with the 3D imaging, advanced fluorescent microscopes have been developed, as Confocal, Multiphoton and Light Sheet: together these are better known as scanning illumination microscopes[27] (Fig.1.2 B, C, D). Confocal Microscopy (CM) is a non-invasive method of optical imaging, which had been developed to face two relevant issues: 1) prevention of out-of-focus and 2) imaging in 3D[27, 29, 31]. CM uses a pinhole in order to block the out-of-focus emission light, whereas the in-focus one can pass to the detector (in particular photomultiplier tube- PMT) and, thus, illuminates the sample. Any single plane of the specimen is scanned back and forth in 2D. Therefore, the final image is assembled as a set of pixels for each single plane and, then, as a sum of all the planes scanned[27, 29]. This process is known as point-source scanning, which involves the oscillation of a horizontal and a vertical mirrors, generating, respectively, x,y scan: the vertical mirror (y) moves much slower

than the horizontal one (x). On the other hand, the speed of the latter is extremely reduced because of its inertia. Totally, the movement of both mirrors contributes to the slowness of imaging, one of the worst drawbacks of this microscopy[29]. Other relevant troubleshooting of CM regards the resolution and the high risk of photobleaching. In his work, Hell demonstrated that CM fails in distinguishing objects that are more closely than 500-800nm[32]. This is mainly due to the focal spot of a lens, which is 3-4 times longer than its with[32] and as the excitation light is not axially confined. This results in a longer exposure of the sample to the excitation light, which potentially could lead to a very fast photobleaching[33]. Despite of that, CM has been becoming a very useful tool not only in the research field, but also in the routine pathology. In their work of 2014, Ragazzi and co-workers demonstrated that it was possible to use CM both on normal and pathologic tissue (breast cancer, pathologic lymph nodes and papillary carcinoma – the most frequent thyroid malignancy), obtaining high resolution with haematoxylin-eosin (H&E) staining[31].

On the other hand, the new frontier of microscopy is represented by the Light Sheet Microscopy (LSM), especially for the improvements in the speed of imaging and the reduced photobleaching[33-35]. There are many types of LSMs, although the concept behind is always to illuminate the sample from the side, in a well-defined volume, located around the focal plane of the detection optics[33]. This microscopy has been bringing many benefits: first of all this is much faster compared to other fluorescent microscopes and offers higher resolution (up to subcellular level) on thicker tissues; furthermore, the risk of photodamage and bleaching is dramatically reduced[33, 35]. In general, in LSM, the excitation and emission lights are split in two different paths, which are orthogonal to each other[33].

Among the different types of LSM, in 2008, Keller and co-workers developed the digital scanning laser light sheet fluorescence microscopy (DLSM), in order to image entire embryos of zebrafish[34]. The logic behind is to have a plane of light, beginning from a side, hitting the whole sample[34]. One of the tools used to achieve that is the "mirror cup", surrounding the detection objective. This is formed by two mirrors, 45° orientated. The laser hits one of the two mirrors; the light is then reflected to the other one and in this way a real light sheet is generated, which illuminates each line of the specimen with the same intensity[34]. This is ideal for the imaging of large specimens. Given the high speed of imaging, the low risk of bleaching and the signal-to-noise ratio, equal to 1000:1[34], DLSM is a real good candidate for the future of the 3D imaging.

**Figure 1.2**: Schematic representation of the light pathway in A) WFM; B) CM, C) Multiphoton Microscopy and D) LSM. In all diagrams, points A and B are situated in the focal plane of the lens while point C is outside the focal plane. Among them, only LSM works to create an excitation light plane, coincident with the focal plane of an imaging objective. Image taken from[36]

### 1.3 Brief description of organs used in this PhD project

Both wild type (WT) and pathologic organs were analysed during the PhD project. Discussing in detail about the anatomy of the studied organs would be beyond the scope of this thesis; for this reason, in order to better identify the different structures further described, only a brief anatomic and histologic overview both of WT and pathologic samples will be given.

#### 1.3.1 WT organs

**KIDNEY**

Kidneys are involved in fluid balance, osmolarity and pH regulation, as well as blood filtration, for solutes reabsorbing and excretion of metabolism end products and drugs[37]. The basic structural and functional unit of the vertebrate kidney is the nephron. In human, the number of nephrons, for each kidney, is estimated to be between 0.8 and 1.5 million[38]. To accomplish all the tasks, the nephron has highly specialised segmentation, whose development could differ from species to species[38]. In mammals, the main nephron segments are the proximal tubules, loop of Henle and distal tubules. In addition, the nephron is characterized by specific elements, as solute transporters and tight junctions, which enable the fine-tuning salt and electrolyte levels in the body[38]. The Bowman's capsule is located before the tubules. The nephron starts with the Bowman's capsule and the capillary tuft together with the tubules come into play. This is the kidney filtering unit, described as a bundle of capillaries, coming from the branching of the afferent artery[39]. Since these are the only

capillaries not surrounded by interstitial tissue, different layers are present in order to maintain their structures, as the proximal layer, characterized by fenestrated endothelium (70-100nm in diameter), the glomerular basement membrane (GBM), and the distal layer, composed by the podocytes[39].

**HEART**

From a histologic point of view, the three main cardiac tissues are: pericardium[40], myocardium[41] and endocardium[41]. The myocardium is characterized by striated and multinucleated cells, composing the functional unit of the cardiac contraction, the sarcomere[41]. The endocardium is the inner cardiac layer, which defines the chambers of the heart. It is involved in different roles, as the control of myocardial contractility, the electrophysiological environment of the cardiomyocites.

Normally, the heart vasculature is classified based on the diameter of the blood vessels, where the two coronary arteries (left and right), have the widest diameter[42]. The arteries spread out into smaller and smaller blood vessel, which are the capillaries, with the smallest diameter[42]. Together, this set of blood vessels supply all the heart[41, 42].

**LUNG**

The most important task of lung is the gas exchange, by delivering oxygen and removing carbon dioxide from blood circulation. Surrounded by the external visceral pleura, to accomplish this task, its inner part is organized as three-like system of conducting airways ventilating the gas exchange area, made by bronchi and bronchioles[43]. The functional unit of the lung is called alveolus, which represents the terminal bronchioles and is located in the lung parenchyma. From the outside, these are composed by an epithelial layer and extracellular matrix, surrounded by a set of blood capillaries. Within the alveoli is a very thin air-blood barrier for gas exchanges[43]. In addition, the bronchi follow the pattern of the pulmonary arteries, which are surrounded by connective tissue[44].

Many and different cell types are found in the lung[44]:

- Ciliated cells, whose main role is to remove foreign microorganism;
- Goblet cells, located in the larger bronchi, but not in the bronchioles;
- Basal cells, which are pluripotential reserve cells, which assure the reconstruction of the bronchial mucosa;
- Alveolar cells type I and II, which are on the wall and on the surface of the alveoli.

**LIVER**

The liver is the biggest gland of the mammalian organism, with many functions in the organism, above all in the metabolism of glucose. It is involved in detoxifying metabolites from blood, glycogen storage, synthesizing plasma proteins as well as in the production of bile, which is important for digestion. From an anatomic point of view, the liver is divided in left and right lobes, where each lobe may be classified as the liver functional unit[45, 46].

Concerning its vasculature, it receives up to 25% of total cardiac output, where the hepatic artery receives between 25% and 30% of the blood supply, and the portal vein all the rest of the blood supply. Both of them converge within the hepatic sinusoids before draining into the systemic circulation via the hepatic venous system[46]. In addition, the biliary drainage is made by the intrahepatic biliary tree, characterized by several ducts, involved in the formation and transport of bile from the liver to the duodenum, by following the portal venous system[46]. Each liver lobule is formed by hepatocytes (parenchymal cells, which occupy 80% of the entire total volume of the liver and represent the 60% of the total cells), performing the majority of liver functions) and non-parenchymal cells which occupy only 6.5% to the liver volume)[47]. The non-parenchymal cells include different type of cells, as sinusoidal endothelial cells, which cover the fenestrated endothelium; Kupffer cells: macrophages allocated in the hepatic sinusoids; hepatic stellate cells (alternatively called Ito cells). The cytoplasm of these cells particularly abounds in lipid vesicles rich with vitamin A[47].

**SPLEEN**[48]

The spleen is classified as a hollow organ, belonging to the immune system. Its main function is filtering blood. From the outside, the spleen is surrounded by a capsule of connective tissue, which works to supply its bloodstream. The main elements of the spleen are the red and white pulps, the capsule of connective tissue and the marginal area. The red pulp is composed by a high specialised venous system which gives to that the unique red colour. Arterial blood comes into cords of connective tissue, known as Cords of Billroth. These create an open blood system without any endothelial coating. Its primary role is to filter microorganism and antigens from blood by the mechanism of erytrhophagocytosis, made above all by macrophages. This is extremely important both for the turnover of erythrocytes and recycling of iron. The structure of the white pulp reminds to a lymph node. This hosts lymphocytes as T and B cells; the arteriole is centrally located within pulp. The marginal area comes between the two pulps: this is a massive transit area, which allows the migration of haematopoietic cells from the bloodstream to the lymphoid regions and back. The maintaining of its integrity

is assured by resident cells. From a microscopic point of view, the amount of blood vessels defines the brightness of the components. Therefore, due to the less quantity of blood vessels and the greater concentration of lymphatic tissue, the white pulp results darker than the red one.

### 1.3.2 Pathologic organs

**KIDNEY INJURY CAUSED BY CISPLATIN TREATMENT**

Cisplatin is a powerful chemotherapy drug, it may provide many side effects; one of the most relevant is nephrotoxicity, leading to acute and chronic kidney injury (AKI; CKI)[49]. In particular, the consequences of cisplatin-induced AKI have been proven in tubular injury (cell damage and dilatation), alteration of the levels of inflammatory cytokine and chemokine (for example TNFα), increase of macrophages levels (M1 and M2 – respectively pro and antyinflammatory macrophages, which are the key mediators of AKI), profibrotic factors (as TGFβ and CTGf), as well as Bowman's capsules and capillary changes[49] .

**AUTOSOMAL DOMINANT POLYCYSTIC KIDNEY (ADPCK)**

One of the most common genetic causes of renal failure is Polycystic Kidney Disease (PKD)[50]. From a histological point of view, renal cysts are found between cortex and medulla, arising from every segment of the nephron (this is, actually, the distinctive feature only of the dominant form and not of the recessive one). Depending on the progression of the disease, they may appear in different colours: from clear to yellow to brown (which is a clear sign of haemorrhages)[51]. In addition, the cysts may contain different ions ($Na^+$, $Cl^-$, $K^+$), growth factors (as, for example, epithelial growth factor), proteases and erythropoietin[51]. Moreover, in the final stage of the disease, glomerular atrophy and interstitial fibrosis may appear, but with no inflammatory infiltrates associated to[51].

# 2. Aims of the study

The goal of this PhD project was to optimize and develop new approaches for visualizing and 3D-imaging tissues and whole organs. Essentially, these approaches were based on optimizing OTC methodologies in combination to the use of CM and LSM.

The core of this research was about the Ethyl Cinnamate-based OTC: starting from a recently published protocol[52], we worked in order to speed up and automate all the procedures, making it suitable for further studies. Initially we started with the clearing only of mouse kidneys and, then, the procedure was extended to other tissues (normal and pathological tissues) not previously analysed yet.

Additionally, we enhanced this methodology, with its application for different scopes, as "re-vitalization" of old paraffin samples and 3D immunohistochemistry for visualizing finer and inner structures.

Our clearing protocol was also tested, for some preliminary studies, on human tissue, with promising results. In parallel, we also tried to figure out the best conditions for the use of both CM and LSM, in order to acquire 2D and 3D images for very large samples.

# 3. Animals, material and methods

### 3.1 Animals

All animal experiments were conducted in accordance with the German Animal Protection Law and approved by the local authority (Regierungspräsidium Nordbaden, Karlsruhe Germany in agreement with EU guideline 2010/63/EU), under anaesthesia.

Unless stated otherwise, 16 weeks old female C57BL/6 wild type mice were used.

The anaesthesia was induced by intra-peritoneal injection of Ketamine and Xylazine (16 mg/kg BW xylazin and 120 mg/kg BW ketamine).

### 3.2 General workflow of Optical Tissue Clearing

OTC general workflow consists of three major steps:

- Pre-processing, which is the animal perfusion;
- Processing, the OTC itself;
- Post-processing, i.e. samples analysis through the microscope.


In Figure 3.1 all the equipment used during the PhD project is shown, as a general overview of the protocol. In order to reach all the organs of the body of the animal, a retrograde perfusion protocol was set up, using a pressure (200mbar) and volume controlled system[53]. The equipment consists in a compressor (Jun-Air compressor, Rio Grande, 117301). To keep the pressure constant and under control, tubes of 0.58 mm of diameter were used. The compressor is connected to two bottles, containing a mixture of NaCl/heparine (0.9% NaCl, pH=7.4; heparin 5 IU/mL) and 4% paraformaldehyde (PFA) respectively. In addition, the device is connected to a syringe pump (Chemyx, Fusion 100 infusion pump) for dye injection. This pump controls the amount of the dye, so that it could be administered at a constant rate, which was set to 1ml/min. This tubing system is, furthermore, connected to a three-way valve, linked to a G25 butterfly needle. Under anesthesia, the abdominal skin and muscle of the animal is cut and then, the needle is inserted into the bifurcation of the aorta and the vena cava is opened. The first step is to remove all the blood from the animal body by flushing with NaCl/heparine (~40ml) in 6 minutes. The presence of the heparin avoids the blood coagulation. Then the dye is injected, at a rate of 1ml/min. In order to eliminate the excess of the unlinked dye, the animal body is flushed a second time with NaCl/heparine for 1minute. Optionally, a second dye is injected, followed by another minute of saline. Lastly, all the

organs are fixed by using 4%PFA for 6 minutes (~40ml). For this project kidneys, heart, liver, lungs, spleen were taken out and stored in 4%PFA at 4°C, until further processing.
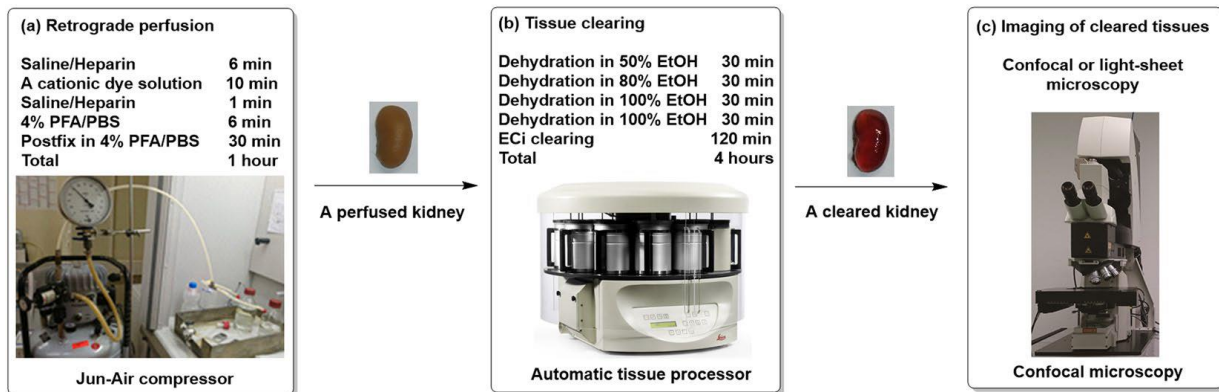


**Figure 3.1**: General overview of the equipment, for the OTC protocol, used during the whole PhD project. On the left side the compressor linked to the bottles for the perfusion; in the middle the instrument for clearing and on the right the confocal microscopy i.e. one of the two microscopes used for 3D imaging. Image taken from[53].

## Ethyl Cinnamate Based OPTICAL TISSUE CLEARING

A new clearing procedure has been recently described by Klingberg et al. in 2017[52], based on the use of ethyl-3-phenylprop-2-enoate (Ethyl Cinnamate – ECi – Fig.3.2). Chemically, ECi is the ester of cinnamic acid and ethanol and this is the principal component of cinnamon essential oil. It is an organic solvent and a lipophilic reagent. It is considered a nontoxic chemical and it is already used as food and cosmetic additive, according to the approval from Food and Drug Administration (FDA)[54]. The ECi-based clearing procedure, provided by Klingberg's group, is described by two major steps: a dehydration step, by using different increasing ethanol concentrations, at 4°C, for lipid extraction and the following clearing, made by the ECi at RT. The total procedure is conducted in a gentle shaking movement and lasts between 16 and 20 hours[52].

One of the aims of this PhD project was to optimize this protocol, in order to make it faster and easier to perform. One of the first steps was to automate it, performing the whole protocols in a tissue processor (TP1020, Leica Biosystem, Nußloch, Germany), which works with vacuum and RT. All the equipment, subsequently mentioned, is related to the tissue processor and was provided directly with it. The specimen are placed into metal boxes and, then, into a basket, which moves, automatically, into different containers, where the first four are filled with ethanol in increasing concentrations (50%,80%,100%,100%) pH 9.0, for the

dehydration steps. Each passage lasts 45 minutes. Lastly, the clearing step by ECi (Sigma-Aldrich, Germany, STBH5252, R.I. 1.558 at 25°C) occurs, for 2 hours, although the samples might stay longer in the solution, i.e. overnight. After completing the procedure, the specimen are collected and stored in ECi, at RT, until imaging. At this point it could also be possible to allow them to stay under gentle shaking, in order to let the ECi penetrate more deeply.
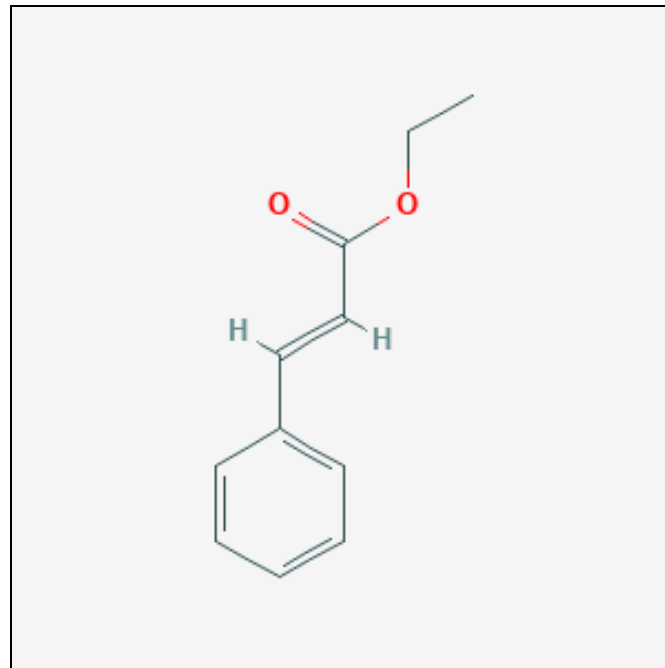


**Figure 3.2**: ECi Chemical structure.
**www.pubchem.ncbi.nlm.nih.gov**

**MICROSCOPY**

The post-processing involves the microscopy: both Confocal (Leica TCS SP8, provided by Leica Biosystem, Mannheim, Germany) and LightSheet (Leica TCS SP8 DLS, provided Leica Biosystem, Mannheim, Germany) microscopes were used for tissue analysis. In the following, a brief description regarding the microscope settings will be given.

The following table (Tab. 3.1) illustrates the working distances of the different objectives used as well as all the mounting media and their own RIs.

| MICROSCOPE | OBJECTIVE | WORKING DISTANCE (mm) | MOUNTING MEDIUM |
|---|---|---|---|
| Confocal | 63x ( HC PL APO 63x/1.40 Oil CS2 – Leica Microsystems, Germany) | 0.14 | Immersion Oil Type F (Leica microsystems [TM]); Glycerol (OmniPur® Glycerol, Merck, Darmstadt, Germany) R.I: 1.518 at 23°C; R.I:1.475 at 20°C[55] |
| Confocal | 20x (HC PL 20x/075 IMM CORR CS2 – Leica Microsystems, Germany) | 0.68 | Immersion Oil Type F (Leica microsystems [TM]); Glycerol (OmniPur® Glycerol, Merck, Darmstadt, Germany) R.I: 1.518 at 23°C; R.I:1.475 at 20°C[55] |
| Confocal | 10x (HCX APO L 10x/0.30 W U-V-I – Leica Microsystems, Germany) | 3.60 | Distilled Water R.I: 1.33[56] |
| LightSheet | 5x(HC PL FLUOTAR 5x/0.15 IMM DLS, Leica Microsystems, Germany) | 1.5 | Glycerol (OmniPur® Glycerol, Merck, Darmstadt, Germany); ECi R.I: 1.475 at 20°C ([55]); 1.558 at 25°C[57] |
| Table 3.1: Description of the different objective used and their features (working distances, immersion media and refractive indexes). | | | |

Moreover, another important issue is how to properly mount the specimen, in order to avoid troubles, regarding the z-dimension. Depending on the microscope used, two ways of sample fixation were settled:

**Confocal Microscope**: <u>Fixation by needle</u>. On the border of a 60mm tissue culture dish (Orange Scientific, Belgium) was attached some adhesive paste (HAMA), in order to fix a $G27_{1/2}$ needle to anchor the specimen. After positioning the specimen, the dish was filled with immersion oil (R.I.:1.518 at 23°C), until the specimen was completely covered. This approach may alternatively use the pasting of the tissue on the centre of the dish, by using a big drop of super glue (UHU).

**LightSheet Microscope**: <u>Fixation with parafilm</u>. The objective of this type of microscope is surrounded by a mirror cap, where the mirrors are orientated at 45° and, due to that, the specimen should fit in the spaces created by this orientation. Another aspect regards the height of the sample which should not exceed 0.5mm in order not to touch the lens of the objective. Keeping in consideration these two pre-requisites, the most suitable method to anchor the samples based on sticking a piece of parafilm of 0.1mm in thickness in the centre of a glass bottom cell culture dish (35mm high, 60μm in diameter, IBIDI, Martinsried, Munich, Germany). On that, a piece of the specimen, maximum 0.4mm in width and 0.5mm in height was used to be pasted, by using the superglue. Finally, the dish was completely filled by either ECi or 88% glycerol (R.I.:1.475 at 20°C[55]). The parafilm helps in making the specimen higher, in order to allow it to be easier reachable by the mirrors and to avoid their direct contact with the bottom of the dish. In fact, this could be a risk in breaking the dish.

## IMAGING SETTINGS

Data from both microscopes were acquired by Las X software (Leica Biosystem, Nußloch, Germany).

**Confocal Microscope**: in order to balance the acquisition time and the quality of the pictures, three parameters were kept constant: the format (resolution) 1024*1024; the speed 600Hz and the scan direction X set to Bidirectional X.

**LightSheet Microscope**: due to the working distance of the objective of this microscope, it is possible to reach a maximum depth of 1.5mm. The settings were settled, keeping in consideration an additional issue: the amount of generated data, which depends on different criteria: a) the resolution (in terms of binning); b) the possibility to work either with the left or right mirror singularly or with both of them; c) the size and the depth of the region of interest to be scanned. Due to that, the usual resolution was set to 2*2 binning at 600 Hz of speed.

**Storage data**: All the data acquired from Confocal and LightSheet microscopy were stored in the Scientific Data Storage (SDS), provided by the Computing Center of University of Heidelberg (Germany).

## 3.3. Staining

In the following sections, a list of all the dyes used is reported. Except for the antibody staining, performed by incubation, all dyes were injected during the perfusion at a constant rate of 1ml/min.

### 3.3.1 MHI148-PEI

The cationic MHI148-PEI (since now on named Cy7-PEI – Fig.3.3) was used to stain anionic structures[53]. This is a near-infrared (NIR) dye (Fig.3.4), coming from the combination of heptamethine cyanine dye (MHI148) and branched polyethylenimine (PEI), synthetized at the Zentrum für Medizinische Forschung (ZMF), Universitätsmedizin Mannheim (Germany), and patented according the code WO/2018/100089. This dye had been designed in order to visualize in 3D vasculature and glomeruli[53]. In order to design this dye, different biological components have been taken in consideration:

-   The negative charge of the glycosaminoglycans (GAGs), main constituents of the blood vessels endothelium;
-   The structure of the glomerular capillary wall, made by a fenestrated endothelium, is 70-90nm in size, a basement membrane of 2-8nm and a fenestrated epithelium, surrounded by podocytes, whose extension is 4-11nm in length;
-   The cut-off of the renal basal membrane is supposed to be 50kDa. That suggests that under normal conditions molecules bigger than this weight cannot overcome the membrane.

The main features of the Cy7-PEI are:

-   A very strong positive charge, due to the presence of the amino groups on the PEI. So, the dye works exclusively for strong electrostatic interactions, binding all the negative charged elements;
-   The absorption and emission spectra. These have been measured in 1x PBS, respectively 654 and 762nm; (Fig.3.4). That ensures a higher penetration depth, reducing the impact of autofluorescence;
-   The molecular weight of the entire molecule (50-100kDa), preventing the passage of the dye into the renal tubules and allowing it to stain the glomeruli as well as the blood vessels.

A variant of Cy7-PEI is the Cy7PEI-opt (optimized), where the only difference is related to the bigger molecular weight (in a range between 50 and 150KDa).

The PEI component works by electrostatic interactions to recognize and bind the negatively charged GAGs; in the meantime, the Cy7 component provides the fluorescent staining, which will be detected by CM and/or LSM. The dye is in a powder form, whose stock concentration was set to be 3mg/ml, to be solved in 1xPBS, followed by the measurement of its wavelengths (absorbance and excitation) at the spectrofluorometer (Tecan Infinite M200, provided by Tecan Austria GmbH, Salzburg, Austria).

During the perfusion, a 10 minutes injection was used (according at the rate of 1ml/min; totally, 10 ml).
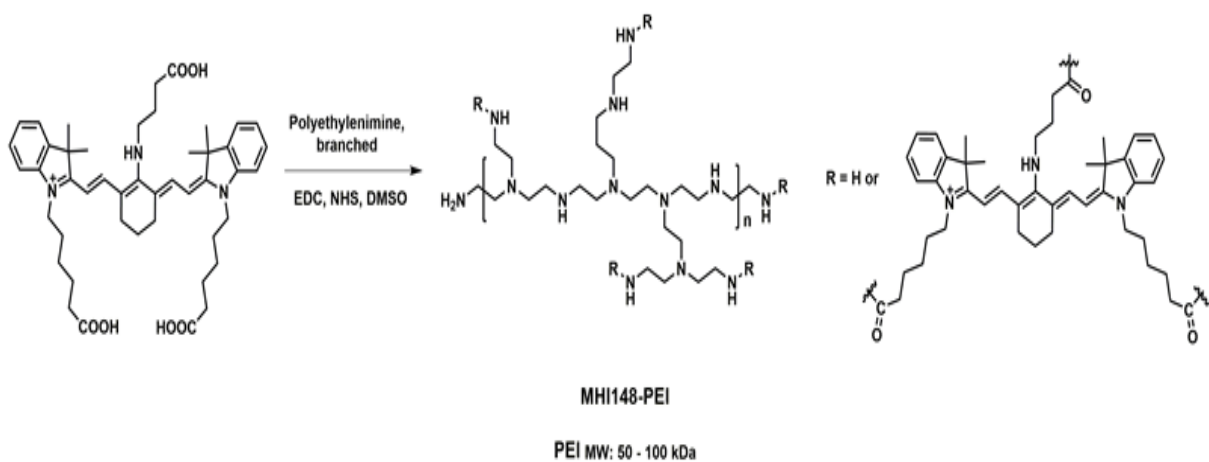


**Figure 3.3**: Molecular structure of MHI148-PEI. The figure summarizes the chemical procedure to obtain the MHI148-PEI. Image taken from[53].
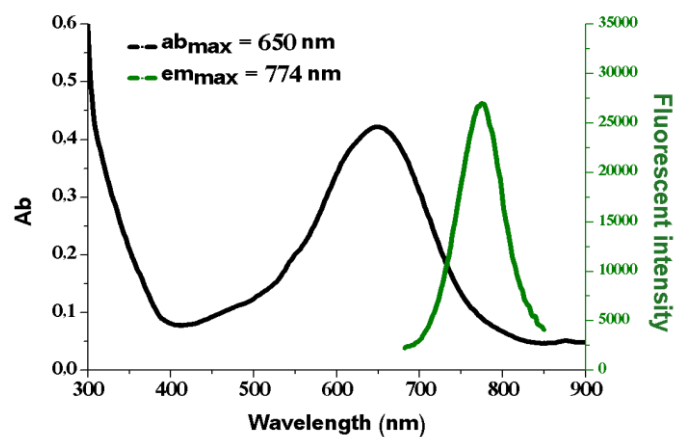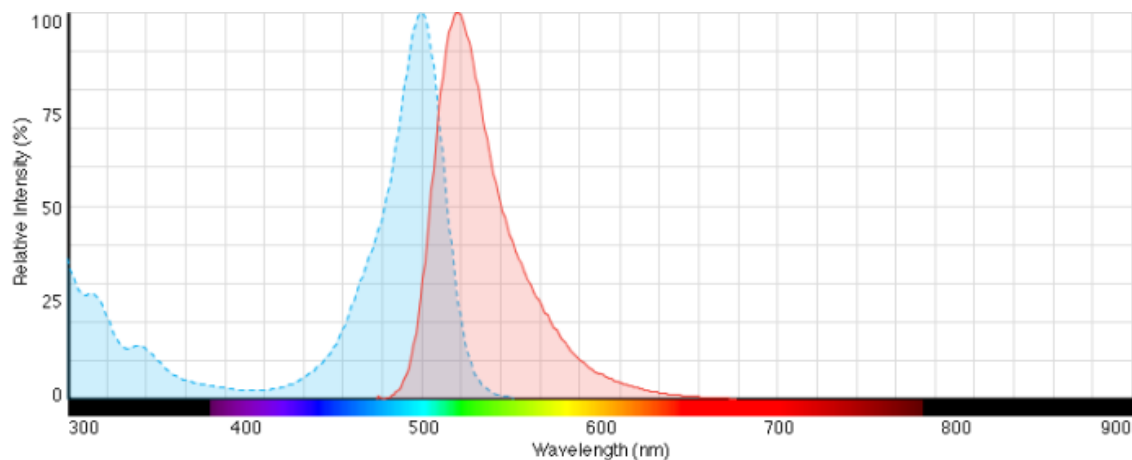
**Figure 3.4**: Fluorescence spectra of MHI148-PEI. The figure shows the absorption (black curve, on the left side) and emission (green curve, on the right side) spectra. As pointed out from the graph the maximum absorption is at 650nm and the emission at 774nm, listing the dye in the NIR region of the visible spectrum. Image taken from[53].

### 3.3.2 Wheat Germ Agglutinin

Wheat Germ Agglutinin (WGA) is a lectin. Lectins are a big family of ubiquitous proteins, carbohydrate-binding. These are known both in animals and in plants. Normally, the lectins recognize and bind to polysaccharides of the cells membranes. In plants, they are supposed to activate the complement system. WGA is a wheat specific lectin, which protects the wheat from insects, yeasts and bacteria by linking itself to N-acetylnerumaninc acid, as components of carbohydrates from cells membranes[58]. Due to their ubiquity, it is possible to find lectins everywhere: this peculiarity has been exploited to make a way of staining, by adding fluorescent molecules, easily microscopically detected.

In our case, WGA was used as conjugated to AlexaFluor™ 488 (W11261, ThermoFischer Scientific, Germany). Its absorption and emission peaks are 490 nm and 520 nm respectively (Fig.3.5), assigning it in the green region of the visible spectrum. The stock concentration was 1mg/ml, diluted at 1:1000 in a final volume of 20ml. During the perfusion, it was used as both single dye and second dye, like a counterstaining. In both cases, it was injected for 10 min and (rate 1ml/min, totally 10ml).



**Figure 3.5**: Fluorescence spectra of Wheat Germ Agglutinin AlexaFluor™ 488 conjugate. The figure shows the absorption (blue light curve, on the left side) and emission (red light curve, on the right side) spectra. As pointed out from the graph the maximum absorption is at 490nm and the emission at 520nm, assigning the dye in the green region of the visible spectrum: **www.thermofisher.com**.

### 3.3.3 Haematoxylin and Eosin (H&E)

H&E staining is one of the most important and frequently used staining in histology usually used on 3-4μm sections of paraffin embedded tissues, previously de-waxed in xylene and hydrated in water[59]. This is a differential staining, where haematoxylin is used to stain cellular nuclei and eosin to counterstain the cell cytoplasm. Both dyes are fluorescent. In particular, haematoxylin binds to basophilic molecules into the cells nuclei (such as DNA and RNA) and, in the staining, appears purple/blue in colour. Haematoxylin itself is a colourless flavonoid, extracted from the logwood tree *Haematoxylon campechianum*[59]. When it is exposed to air, it is oxidized to haematein (Fig.3.6) and this is the compound which truly works for the staining. Chemically speaking, this form is also amphotheric, becoming red at acid pH and blue at basic pH. The oxidation occurs by combining the haematoxylin with sodium iodate, as oxidant agent, plus potassium sulphate as mordant[59]. Since the beginning of the XX century, many mordants have been described such as ammoinium or potassium aluminum sulfates, potassium alum, mercuric oxide and ammonium alum, ferric ammonium sulphate[59].
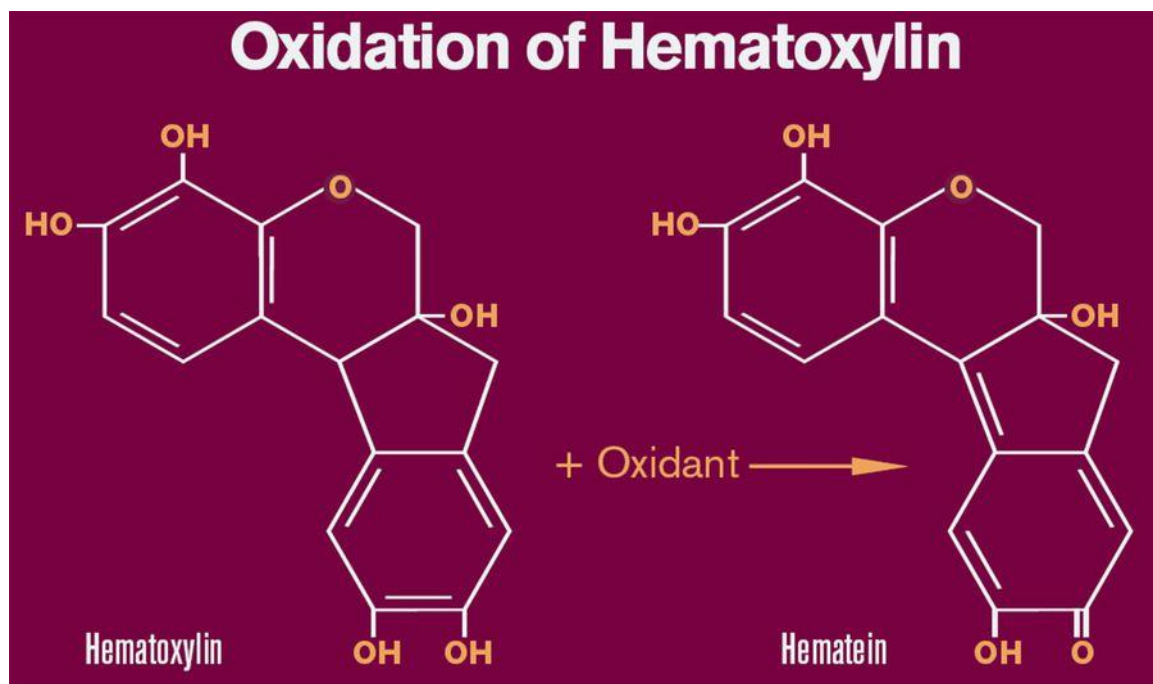


**Figure 3.6**: The chemical process of the oxidation of the haematoxylin in haematein, so that the compound which, truly, works in the process of the staining: **www. leicabiosystems.com**

In turn, eosin was discovered in 1874 by Heinrich Caro, who added bromine to fluorescin[60]. Eosin, in fact, defines a group of fluorescent molecules binding eosinophilic compounds like

proteins with high percentage of arginine or lysine, as amino acids. The most known eosin molecules are the Y and B forms (Fig.3.7 A and B), respectively a tetrabromo and dibromo derivatives of the fluorescin. As counterstaining, the most used is the Y variant, which makes the cytoplasm coloured in pink/reddish.

**A**                                                                                           **B**
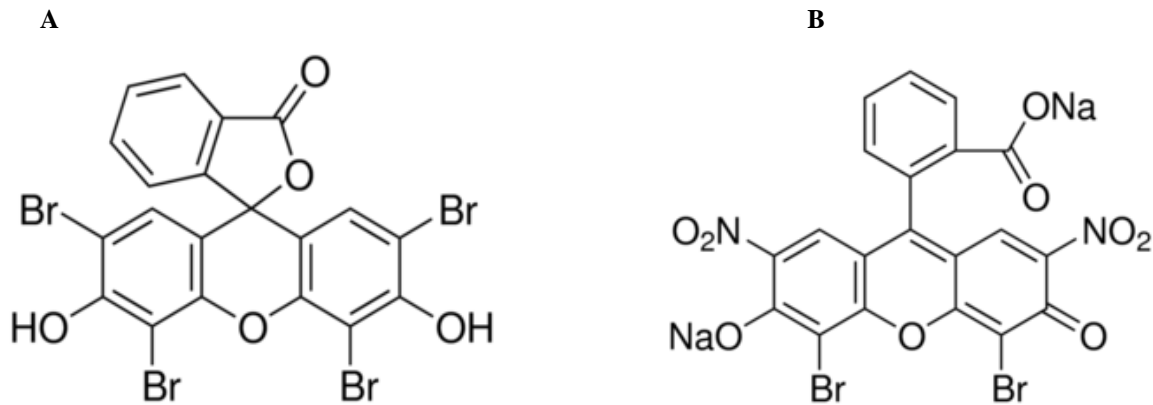
Figure 3.7: The two forms of eosin. A): Y form, which is a tetrabromo derivate. B): B form, a dibromo derivate: **www. sigmaaldrich.com**

Taking into account the fluorescence of these dyes, some mouse, rat and human kidney 5µm slides, stained with the standard H&E protocols of staining, were imaged with CM.

For this purpose, two protocols were used: one from the ZMF, Universitätsmedizin Mannheim (Tab. 3.2 a) and the second from the Pathology Department of Universitäts Klinikum of Mannheim (Tab. 3.2 b).

| ZMF H&E staining protocol | |
|---|---|
| Protocol performed in the Autostainer XL, provided by Leica Biosystem, Mannheim, Germany | |
| **Reagent** | **Time (min)** |
| Xylol | 1 (x4) |
| 99% Ethanol | 1 |
| 96% Ethanol | 1 |
| 80% Ethanol | 1 |
| 70% Ethanol | 1 |
| dd $H_2O$ | 1 |
| Hematoxylin | 4 |
| dd $H_2O$ | 10 |
| 0.5% aqueous Eosin | 2 |
| 96% Ethanol | 1 (x2) |
| 99% Ethanol | 1 (x3) |
| Xylol | 1 (x2) |
| **Material** | |
| Hematoxylin | Hämalaun sauer nach Mayer |
| Eosin | Eosinlösung 0.5% wässrig |

**Table 3.2 a**: Description of the H&E staining protocol 1

| Pathology Department H&E staining protocol | |
|---|---|
| **Reagent** | **Time (min)** |
| Xylol | 2.30 (x2) |
| 100% Ethanol | 1 |
| 96% Ethanol | 1 |
| 80% Ethanol | 1 |
| dd $H_2O$ | 1 |
| Hematoxylin | 2 (x2) |
| Water bath | 3 |
| 0.5% aqueous Eosin | 1 (x2) |
| Water bath | 1 |
| 96% Ethanol | 1 (x2) |
| 100% Ethanol | 1(x3) |
| **Material** | |
| Hematoxylin | Hämalaun sauer nach Mayer |
| Eosin | Eosinlösung 0.5% wässrig |

**Table 3.2 b**: Description of the H&E staining protocol 2

Furthermore, some experiments on whole mice and rats were performed, in order to figure out the effect of this staining on whole organs. Different combinations of H&E (Dr. K.Hollborne & Söhne GmbH & Co Kg, Leipzig, Germany) were injected during the perfusion, by keeping the pressure constant and following the usual rate at 1ml/min. The diverse trials are summarized in Table 3.3.

| TRIAL N. | MOUSE N. | REAGENT | TIME (min) | VOLUME (ml) |
|---|---|---|---|---|
| 1 | 1 | NaCl pH 7.4 + hep | 6 | ~40 |
| | | Cy7PEI | 10 | 10 |
| | | NaCl pH 7.4 + hep | 1 | ~7 |
| | | Haematoxylin | 5 | 5 |
| | | NaCl pH 7.4 + hep | 1 | 1 |
| | | Eosin | 5 | 5 |
| | | NaCl pH 7.4 + hep | 1 | ~7 |
| | | 4%PFA | 6 | ~40 |
| 2 | 1 | NaCl pH 7.4 + hep | 6 | ~40 |
| | | Haematoxylin | 5 | 5 |
| | | NaCl pH 7.4 + hep | 1 | ~7 |
| | | 4%PFA | 6 | ~40 |
| 2 | 2 | NaCl pH 7.4 + hep | 6 | ~40 |
| | | Eosin | 5 | 5 |
| | | NaCl pH 7.4 + hep | 1 | ~7 |
| | | 4%PFA | 6 | ~40 |
| 3 | 1 | NaCl pH 7.4 + hep | 6 | ~40 |
| | | Haematoxylin | 3.5 | 3.5 |
| | | NaCl pH 7.4 + hep | 1 | ~7 |
| | | Eosin | 1.5 | 1.5 |
| | | NaCl pH 7.4 + hep | 1 | ~7 |
| | | 4%PFA | 6 | ~40 |
| 3 | 2 | NaCl pH 7.4 + hep | 6 | ~40 |
| | | Haematoxylin | 1.5 | 1.5 |
| | | NaCl pH 7.4 + hep | 1 | ~7 |
| | | Eosin | 3.5 | 3.5 |
| | | NaCl pH 7.4 + hep | 1 | ~7 |
| | | 4%PFA | 6 | ~40 |

**Table 3.3**: Sum up regarding the three different trials about the perfusion made by H&E. The pressure has to be considered set at 200mbar.

### 3.3.4 3D Immunohystochemistry

In the following section a list of antibodies used is reported.

- Polyclonal Goat Anti-Nephrin primary antibody (AF3159), purchased by R&DSystems, Germany;
- Chicken Anti Goat Secondary Antibody AlexaFluo 647 conjugated (A21469), purchased by ThermoFisher Scientific, Germany;
- Normal Unconjugated Chicken Serum, purchased by Jackson ImmunoResearch Europe Ltd, UK;
- SYTOX$^{TM}$ Green Nucleic Acid Stain (S7020), purchased by ThermoFisher, Germany Scientific.

## 3.4 Validation data: comparison, shrinkage studies and lipid assay

In order to understand which of the two ECi-based OTCs could result in more shrinkage, some studies were conducted. By following the procedure, described by Araujo et al. in 2014[61], weight (g), area (in cm$^2$) and volume (cm$^3$) of the samples before and after the clearing procedures were measured. After positioning the samples on a graph paper (minimum unit of measurement 1mm), the three dimensions (length, width and thickness, referred as r1, r2, r3 respectively) of each sample were measured. The area was calculated by multiplying r1*r2, while the volume was calculated by applying the formula for the calculation of the volume of the ellipsoid: V=4/3 *π* (r1*r2*r3). Furthermore, also a lipid assay was performed before and after the clearing procedures by using the Phospholipids Assay Kit (Sigma-Aldrich, Germany, Catalog Number MAK122), in a final ratio buffer/tissue of 1ml:100mg.

## 3.5 Alternative uses of ECi-based OTC

### 3.5.1 De-paraffinization and clearing of paraffin blocks

Paraffin blocks were treated in a way to ensure, at the same time, both de-paraffinization and clearing of the specimens within them. For this purpose, a smaller tissue processor, the Leica EM TP (provided by Leica Biosystem, Nußloch, Germany), was used, which allowed to run a maximum of 4 samples in one go. The protocol is the following:

- Initially, the block was placed into an incubator at 60°C for ~20min, to allow the paraffin melting, so that it could easier be removed;
- After carefully removing the melted paraffin, the specimen was placed in the first vial of the machine, containing pre-heated (60°C) xylol, for 90min;

- Then, automatically, the sample moves to a second xylol vial (60°C; 90min); These two stages were introduced to remove all the residues of paraffin.

- A very strong dehydration was performed in the next three vials, containing 100% ethanol (35°C and 90min. for the first two ones; 35°C and 45min, for the last one);

- Finally the clearing was performed by moving the sample in three different vials containing ECi (35°C and 60min x2; 35°C and overnight x1).

Once completing the process, the specimens were stored in ECi at RT (optionally, on a roller), until the imaging. This was performed by using the same settings as previously described, both for CM and LSM.

### 3.5.2 ECi removal and 3D Immunohistochemistry

Starting from the protocols published by Dickie et al. in 2006[62] and Gleave et al. in 2013[63], a new 3D immunohistochemistry (3D-IHC) protocol after ECi-based OTC has been established. Before proceeding with the protocol itself, the innovative and essential step was to remove ECi, within the organs, and to perform a further second rehydration. In fact, the massive use of hydrophilic substances combined with the presence of ECi (hydrophobic) could have negatively affected the final results. The protocol has been tested on WT mouse kidney.

After perfusion and fixation in 4% PFA, sections of 1mm of kidney were cut, by using either a Vibratome (VT1200/S, provided by Leica Biosystem, Nußloch, Germany) or a rat heart matrice (65-2100, provided by AgnTho's AB, Lidingö, Sweden) before the clearing procedure. The ECi removal and the second rehydration consisted in the reverse process of the dehydration prior to the clearing, slightly changing the ethanol incubation times (99% 60min; 99% 45min; 80% 45min 50% 60min). The samples were, then, stored in 1xPBS at RT overnight. The next day, in order to better unmask the proteins, antigen retrieval was performed by incubating the sample in citrate buffer pH 6.0 at 37°C for 24 hours. Afterwards, a quenching step was required to reduce the autofluorescence and the background level from the samples. To do that, the samples were incubated in 500mM Glycine (Sigma-Aldrich, Germany, GE17-1323-01) for at RT 24 hours, by alternating the use of the roller for 2 hours and the sonicator for 15'. Lastly, the sample was incubated at 37°C overnight. The permeabilization step was performed, by using Triton X-100 (Sigma-Aldrich, Germany, 9002-93-1) in 1x PBS at 37°C, totally for 48 hours: 1% for the first 24 hours and 2% for the second 24 hours. The blocking in 5% Chicken Serum occurred at 37°C for 48 hours, by changing the solution every 24 hours. The primary antibody (Antibody against Nephrin; stock

concentration: 0.2mg/ml, diluted 1:100, in a final volume of 5ml) was incubated at 37°C 48 hours changing the solution every 24 hours, and, then, a washing step in 1x PBS at RT occurred. The secondary antibody (Antibody anti Goat AlexaFluo 647 conjugated - stock concentration 2 mg/ml, diluted 1:200, in a final volume of 5ml) was incubated at 37°C for 72 hours changing the solution every 36 hours. Finally, a 24 hours washing in 1x PBS at RT step was performed. Furthermore, a nuclear staining was performed, by using Sytox$^{TM}$ Green (stock concentration 5mM, diluted 1:20.000, in a final volume of 5ml), in PBS-T incubated at 37°C overnight. After washing in 1x PBS at RT, the sample was made ready for the imaging. The imaging was performed by CM, by using either 20x or 63x in 88% glycerol. The analysis was performed after incubating the slice in 88% glycerol for 24-48 hours, at RT, for RIs correction.

# 4. Results

## 4.1 Perfusion

In the following table (Tab.4.1) the two different perfusion trials tested, in order to set the exact parameters, are listed. To speed the whole procedure up, the second method of perfusion was chosen and kept for the overall period of the project.

| | REAGENT | TIME (min) | AMOUNT(ml) | PRESSURE(mbar) | TOTAL TIME(min) |
|---|---|---|---|---|---|
| 1st TRIAL | NaCl pH 7.4+ hep | 6.15 | ~41 | 300 | 28.30 |
| | DYE | 15 | 15 | 300 | |
| | NaCl pH 7.4+ hep | 1 | ~41 | 300 | |
| | 4% PFA | 6.15 | ~41 | 300 | |
| 2nd TRIAL | NaCl pH 7.4+ hep | 6 | ~40 | 200 | 23 |
| | DYE | 10 | 10 | 200 | |
| | NaCl pH 7.4+ hep | 1 | ~40 | 200 | |
| | 4% PFA | 6 | ~40 | 200 | |

**Table 4.1**: The table shows the two main trials regarding the perfusion procedure. The second method was kept during the whole project.

## 4.2 ECi-based Optical Tissue Clearing

In order to optimize and automate the whole Klingberg's procedure[52], the different approaches tested are shown and described in the following tables (Tab.4.2, 4.3, 4.4). All the modifications introduced are underlined in red and green.

**FIRST APPROACH**

| Klingberg et al., 2017 [52] | | | |
|---|---|---|---|
| REAGENTS | CONCENTRATION (%) | TIME (min) | TEMPERATURE (°C) |
| Ethanol | 30 | 240 | 4-8 |
| Ethanol | 50 | 240 | 4-8 |
| Ethanol | 70 | 240 | 4-8 |
| Ethanol | 100 | 240 | 4-8 |
| Ethanol | 100 | 240 | 4-8 |
| ECi | Absolute | 120 | RT |

| FIRST APPROACH (TP1020, Leica Biosystems) | | | |
|---|---|---|---|
| **REAGENTS** | **CONCENTRATION (%)** | **TIME (min)** | **TEMPERATURE (°C)** |
| Ethanol | **50** | 240 | **RT** |
| Ethanol | **80** | 240 | **RT** |
| Ethanol | 100 | 240 | **RT** |
| Ethanol | 100 | 240 | **RT** |
| ECi | Absolute | 120 | RT |

**Table 4.2**: The first approach of the optimization is presented. In red the most important modifications made to the original protocol.

In this first approach, the most important changes were:

- The use of the TP1020, in order to speed the whole process up;
- The optimized protocol starting from 50% ethanol, instead of 30%. The reduction of the number of ethanol steps helped in speeding the procedure up. In addition, to make the dehydration stronger, the second ethanol step was increased from 70 to 80%;
- The cool temperature (4°C) was substituted with RT (~21°C), to improve the diffusion coefficient of the different reagents.

## SECOND APPROACH

| ECi-based Optical Tissue Clearing (TP1020, Leica Biosystem) | | | |
|---|---|---|---|
| **REAGENTS** | **CONCENTRATION (%)** | **TIME (min)** | **TEMPERATURE (°C)** |
| Ethanol | **50** | **60** | **RT** |
| Ethanol | **80** | **60** | **RT** |
| Ethanol | 100 | **60** | **RT** |
| Ethanol | 100 | **60** | **RT** |
| ECi | Absolute | 120 | RT |

**Table 4.3**: The second approach of the optimization is presented. In red the previous modifications which have been kept and in green the new ones subsequently made.

In addition to the previous modifications, related to ethanol concentrations and temperature, in this second approach the times for the ethanol steps were further shortened, without changing the time for the ECi.

**THIRD APPROACH**

| ECi-based Optical Tissue Clearing (TP1020, Leica Biosystem) | | | |
|---|---|---|---|
| **REAGENTS** | **CONCENTRATION (%)** | **TIME (min)** | **TEMPERATURE (°C)** |
| Ethanol | **50** | **45** | **RT** |
| Ethanol | **80** | **45** | **RT** |
| Ethanol | 100 | **45** | **RT** |
| Ethanol | 100 | **45** | **RT** |
| ECi | Absolute | 120 **(o/n)** | RT |

**Table 4.4**: The third approach of the optimization is presented. In red the previous modifications which have been kept and in green the new ones made on the subsequently.

This is the protocol kept during the whole project. The times for the ethanol steps were further reduced to 45 min, without changing the ECi timing, kept to 120 min, although the samples may stay longer, for example overnight plus further gentle shaking, to allow ECi penetrate better and make the samples clearer.

**4.3 Imaging Settings**

Before listing all the attempts tested, it is needed to underline the difference, in terms of immersion media, between CM and LSM. In fact, speaking about CM, all of the attempts performed, to mount the samples, were done by using immersion oil, instead of ECi itself, as ECi evaporates rapidly. On the other hand, thanks to the much higher speed of data acquisition of LSM, it was possible to use ECi, as immersion medium, without facing the problem of evaporation. The ways of fixing are listed below:

a) **Glass slide plus coverglass**: after cutting a very thin portion from the sample with disposable scalpels (Swann-Morton, Sheffield S6 2BJ England), this was placed on a glass slide (Ca/env 76*26 mm, Menzel Gläser, Thermo Fisher Scientific Gerhard Menzel B.V. & Co., Germany) and covered by a cover glass (24*32 mm, Hirschmann Laborgeräte GmbH & Co., Germany). A quite big drop of immersion oil was placed on the top of the coverglass;

b) **Glass slide without coverglass**: the same procedure as point a), but without cover glass. Immersion oil was placed directly on the specimen;

c) **Agarose embedding**: a glass ring was attached on a glass slide (Ca/env 76*26 mm, menzel gläser, Thermo Fisher Scientific Gerhard Menzel B.V. & Co., Germany), by using silicon. The specimen was oriented in 500µl of melted 1% agarose (Invitrogen^TM UltraPure^TM Low Melting Point Agarose, Thermosfisher Scientific, Germany, 16520100) and positioned in the glass ring, by producing 1 or 2 layers. Everything was, then, closed by a round cover glass of 22*22mm in size (Thermo Fisher Scientific Gerhard Menzel B.V. & Co., Germany), plus immersion oil on top;

d) **Fixation by needle**: On the border of a 60mm tissue culture dish (Orange Scientific, Belgium) was attached some adhesive paste (HAMA) , in order to fix a $G27_{1/2}$ needle, which worked to anchor the specimen. After positioning the specimen the dish was filled by either immersion oil or some other hydrophilic mounting media, as PBS, distilled water or 88% glycerol, which completely covered the specimen. Alternatively, for tissues with a not homogeneous and fragile surface (i.e. liver), which could be easily damaged by the insertion of the needle, it was also possible to stich a part of that, in the centre of the dish, by using a big drop of super glue (UHU). These ways of fixation worked with both immersion oil and hydrophilic mounting media.

e) **Fixation with parafilm (LightSheet Microscope)**: The most suitable method to anchor the samples based on sticking a piece of parafilm of 0.1mm in thickness in the centre of a glass bottom Petri dish (35mm high, 60µm in diameter, IBIDI, Martinsried, Munich, Germany). On that, a piece of the specimen, maximum 0.4mm in width and 0.5mm in height was pasted, by using the superglue. Finally, the dish was completely filled with ECi.

Method d) for CM and method e) for LSM were used to fix the samples for the 3D imaging. Table 4.5 presents a list of advantages and trouble shootings.

| METHOD | ADVANTAGES | TROUBLESHOOTING |
|:---:|:---|:---|
| a | Easy to handle; does not require high quantity of material | The architecture of this approach cannot ensure the good quality of the scan for different reasons:<br>- The small amount of mounting medium is not enough for the objective;<br>- The sample cannot be well anchored to the glass slide;<br>- The presence of the coverglass, which cannot be well fixed, due to the thickness of the sample.<br>As result of all of these factors, the z direction often appears twisted and noisy, altering the structural data. |
| b | Easy to handle; does not require high quantity of material | Despite the removing of the coverglass from the specimen, the 3D image is still twisted and noisy. Losing many structural data in the 3D image. |
| c | This approach could solve the issue of the movement, blocking the specimen in a ring of agarose | Mismatch in RIs between ECi, agarose and immersion oil. Very high noise level. |
| d | No specimen movement; the z direction is straight and the objective can work with the right quantity of immersion oil (or, when requested, distilled water, PBS or glycerol) | Requires high quantity of material |
| e | The sample is well anchored on this support and all the sizes are very well respected | Not so easy to handle. |

**Table 4.5**: List of main advantages and trouble shootings of the different trials regarding the specimen mounting on the support.

## 4.4 Microscopy Results

This section will go through the different images, obtained from the aforementioned clearing method and the two different microscopes. Unless stated otherwise, the samples were harvested from WT mice, strain C57BL/6 and stained with Cy7-PEI in 3mg/ml as concentration.

### 4.4.1 ECi-based OTC: Results

The images regarding the first two approaches of the optimization of ECi-based OTC method are related mostly to kidney. They are shown in order to go through the different improvements and progresses obtained during the diverse phases of the protocol optimization, which involves also the one of the perfusion protocol. In fact, these first two trials of ECi-based OTC were used in combination with the first perfusion protocol.

On the other hand, the last approach, which was kept overall in the project and used to clear not only mouse organs, but also many other types of samples, has always been used with the second perfusion protocol.

### FIRST APPROACH

As indicated by blue arrows in Figure 4.1, the main elements of kidney, as glomeruli, renal tubuli and blood vessels are shown in both images: A) in 3D and B) in 2D. Although the background noise is still quite high, already from the first trial it is possible to visualise "through" in the correct way.
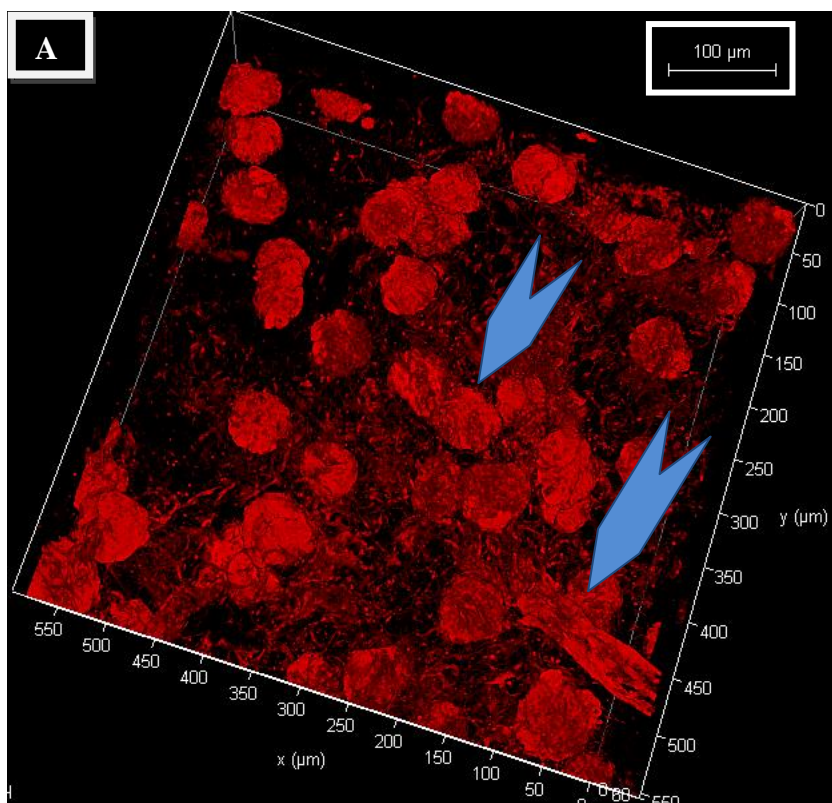


**Figure 4.1**: Sections of mouse kidney, acquired by CM, using a 20x objective in immersion oil and the 638 channel. A) 3D section. As indicated by the blue arrows, a renal blood vessel and glomeruli are visible and distinguishable. Scale bar: 100µm. B) 2D section. Again blue arrows are indicating structured glomeruli and tubules. Scale bar: 75µm
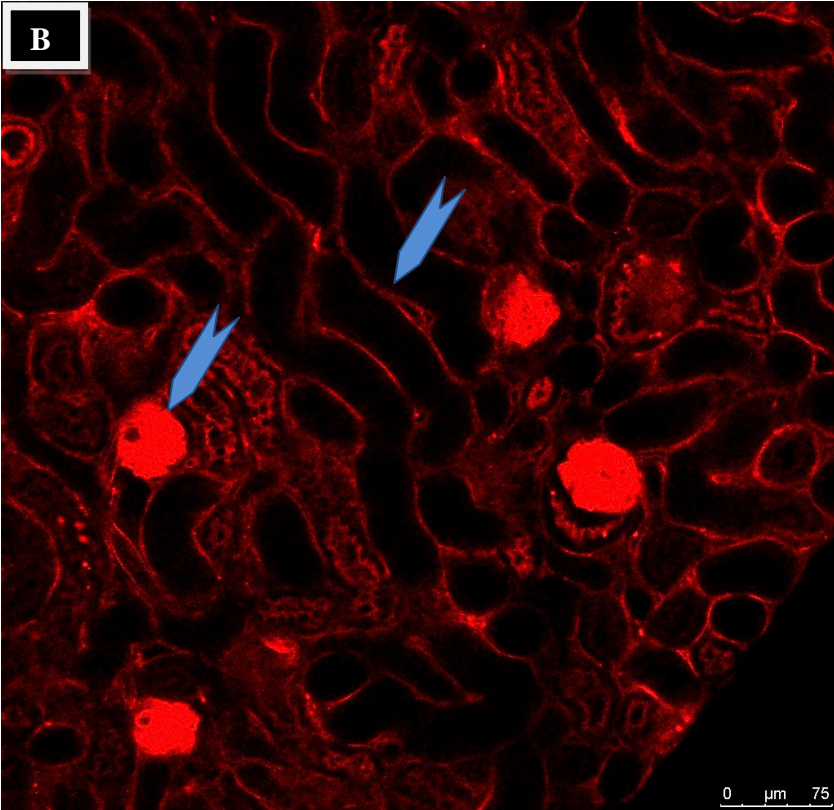
## SECOND APPROACH

Figure 4.2 shows a section of mouse kidney, in which the presence of glomeruli as well as blood vessels is well underlined, despite still the occurrence of background noise. As indicated by the light blue arrow, a renal blood vessel is connected to some glomeruli.
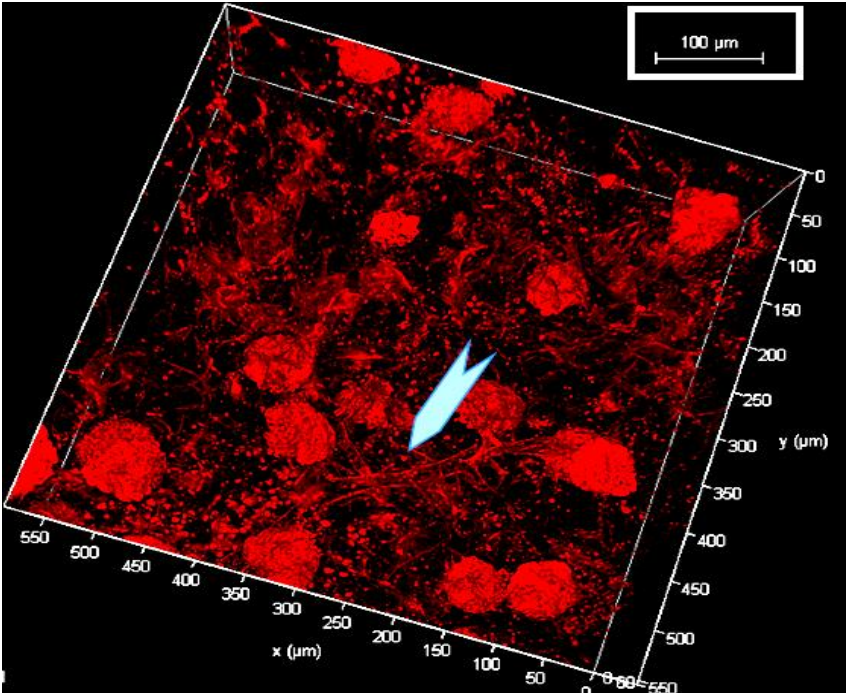


**Figure 4.2**: 3D section of mouse kidney imaged by CM, using a 20x objective in immersion oil and the 638 channel. Scale bar: 100μm.

**THIRD APPROACH**

This is the approach kept throughout the PhD project, as it allowed the imaging of many types of samples. In the following section, some examples of different organs cleared and imaged will be shown. In order to distinguish which type of microscopy was used (CM or LSM), in each caption objective, microscope, mounting medium and channel used will be indicated.

**Mouse Kidney: Confocal Microscopy**

Figure 4.3 is one of the first samples cleared by using the third approach, kept overall in the project. Characterized by a very low background noise level, this image reveals in a very clear way the glomeruli and renal blood vessels they are linked to. In addition, looking at the images in depth coding it is also possible to claim that the glomeruli are present in different depth points, confirming, therefore, the functionality of this protocol.
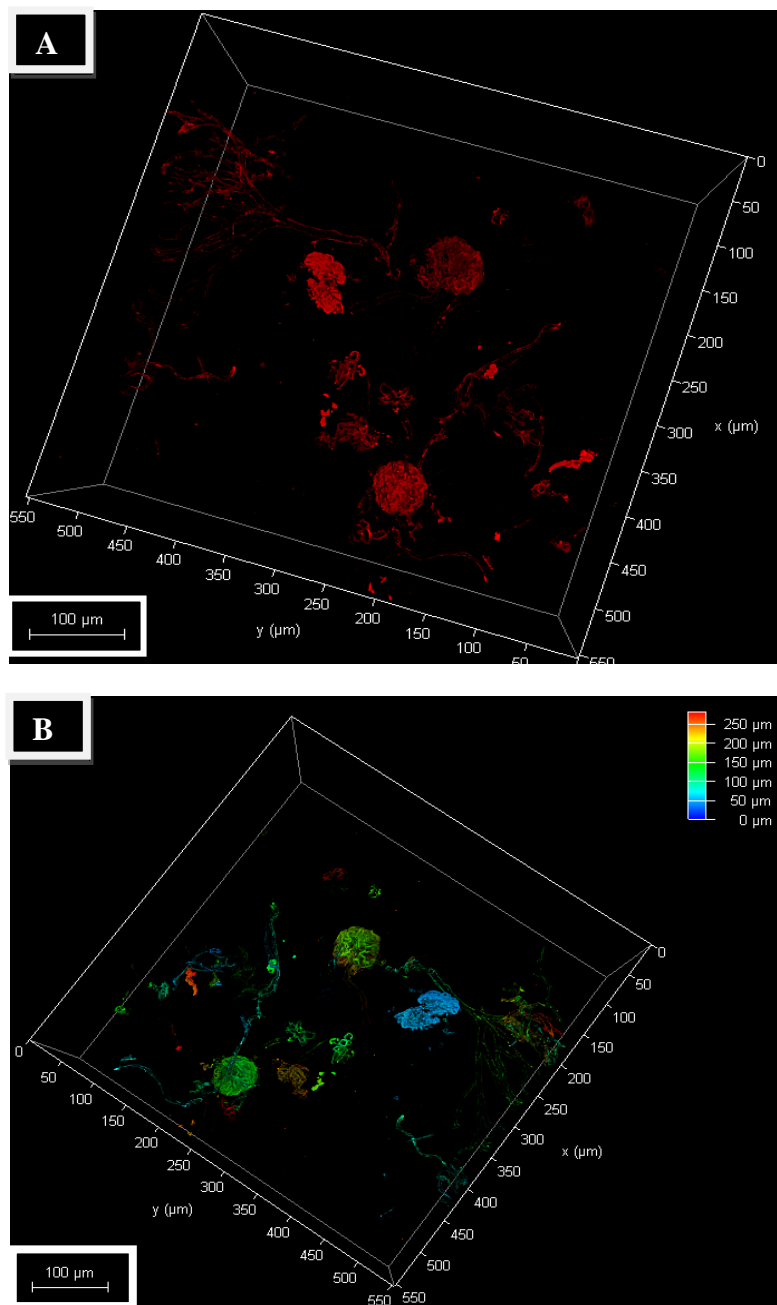


**Figure 4.3**: 3D Sections of mouse kidney, stained with Cy7-PEI-opt acquired by CM, using a 20x objective in immersion oil and the 638 channel. In A) and B) the view, respectively without and with depth coding, is presented. As indicated from the depth bar on the right side of the image B), the depth reached is 250 μm. This scale goes from the surface of the sample (0-100μm, in blue-light blue), middle part (100-200μm, in green) up to the deepest part of the region (200-250μm, in yellow-red). Scale bars: 100μm.

Figure 4.4 shows results from the WGA staining. Thanks to that, many and different structures were imaged in one go and without requiring a differential coloration. These images do not only show glomeruli, but even renal tubuli. The glomerular structure is very well defined, showing also the glomerular tuft in detail. Moreover, as underlined by the red rectangle on the bottom of Figure 4.4 C), a renal blood vessel and some erythrocytes inside are distinguishable. In Figure 4.4 D), the red arrow indicates a renal blood vessel linking to a very distinct glomerulus, and the presence of erythrocytes is very prominent.
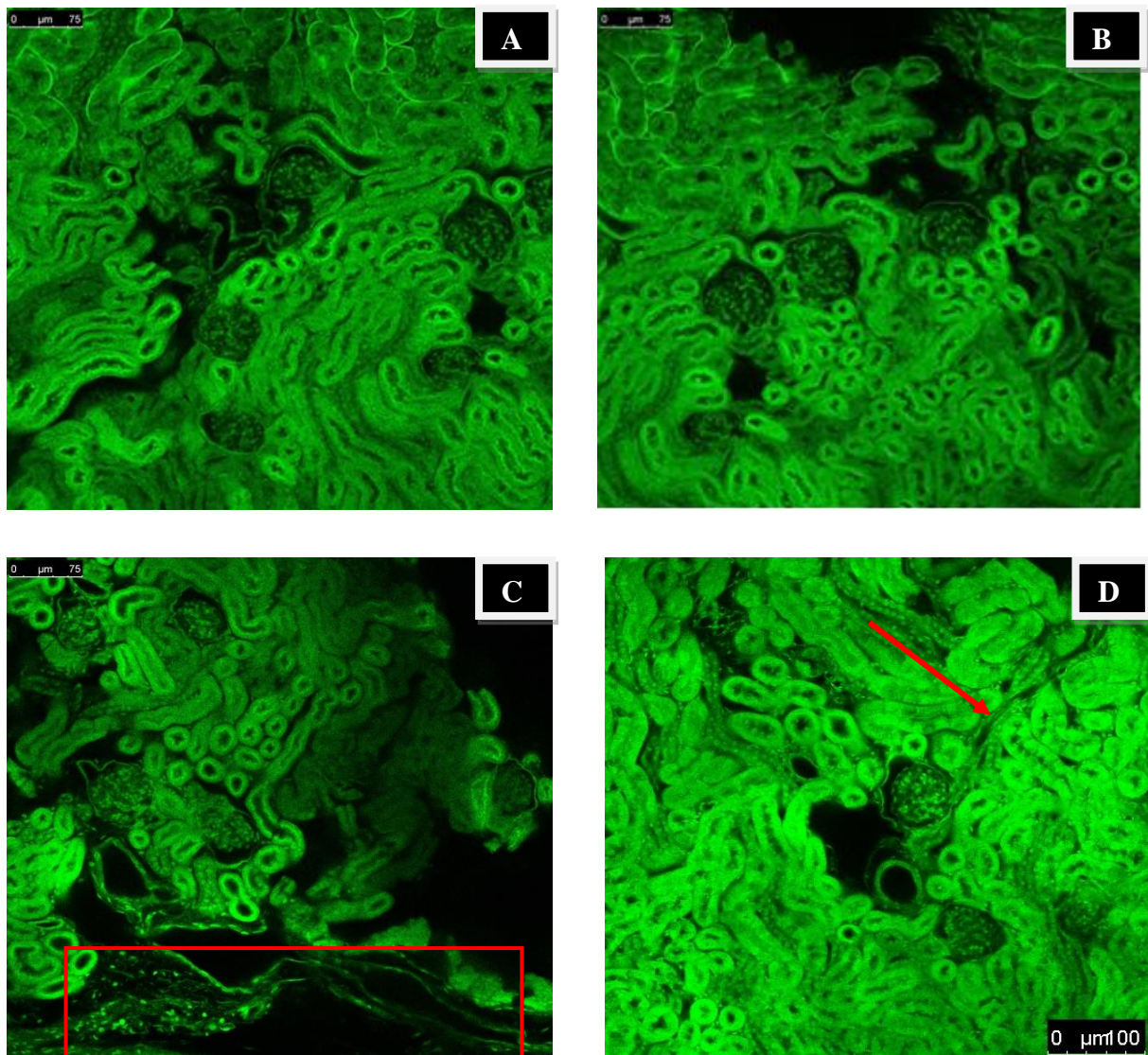


**Figure 4.4**: 2D Section of mouse kidney stained with WGA-AlexaFluo 488 conjugated (stock concentration 1mg/ml, diluted 1:1000 in a final volume of 20 ml of solution) and imaged by CM, using a 20x objective in immersion oil and the 488 channel. A), B), C), D): different views from the same section. Scale bars A), B), C): 75µm. Scale bar D):100µm

In Figure 4.5, an example of double and differential staining is shown, in which both dyes stain in a specific way different structural elements. The WGA is linked to the renal tubuli as well as to the glomeruli, while the Cy7-PEI to the renal vessels and glomeruli as well. The image in overlay comes from the overlap of the two colours, which gives orange shading on the elements that absorb both of dyes.
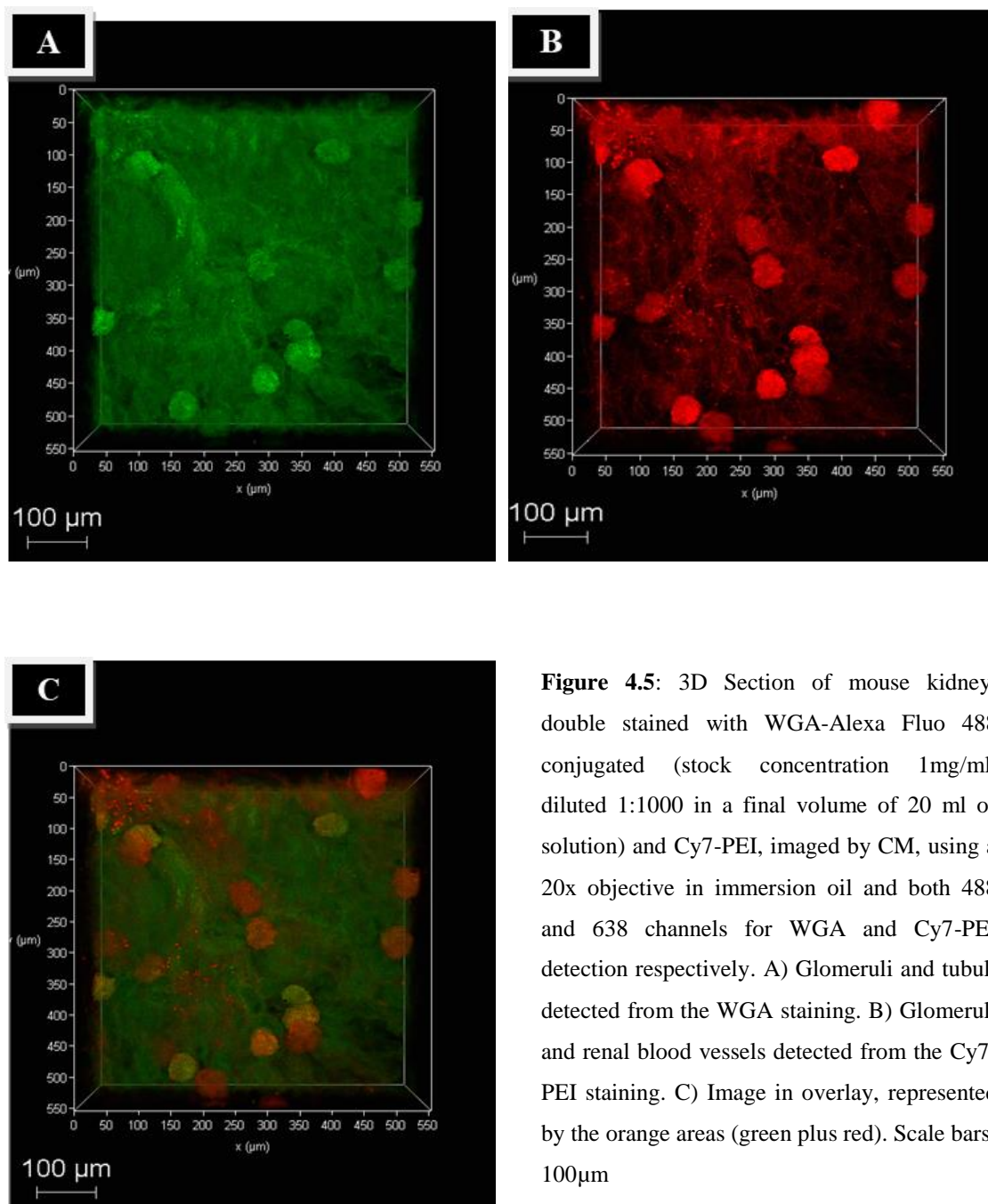






**Figure 4.5**: 3D Section of mouse kidney, double stained with WGA-Alexa Fluo 488 conjugated (stock concentration 1mg/ml, diluted 1:1000 in a final volume of 20 ml of solution) and Cy7-PEI, imaged by CM, using a 20x objective in immersion oil and both 488 and 638 channels for WGA and Cy7-PEI detection respectively. A) Glomeruli and tubuli detected from the WGA staining. B) Glomeruli and renal blood vessels detected from the Cy7-PEI staining. C) Image in overlay, represented by the orange areas (green plus red). Scale bars: 100μm

Figure 4.6 displays glomeruli as well as afferent renal vessels and some blood capillaries in a very clear way. In A), the original view is shown, with a very low background noise level, whereas in B) the depth coding, indicating the depth reached. As indicated by the depth coding, different depths have been detected.
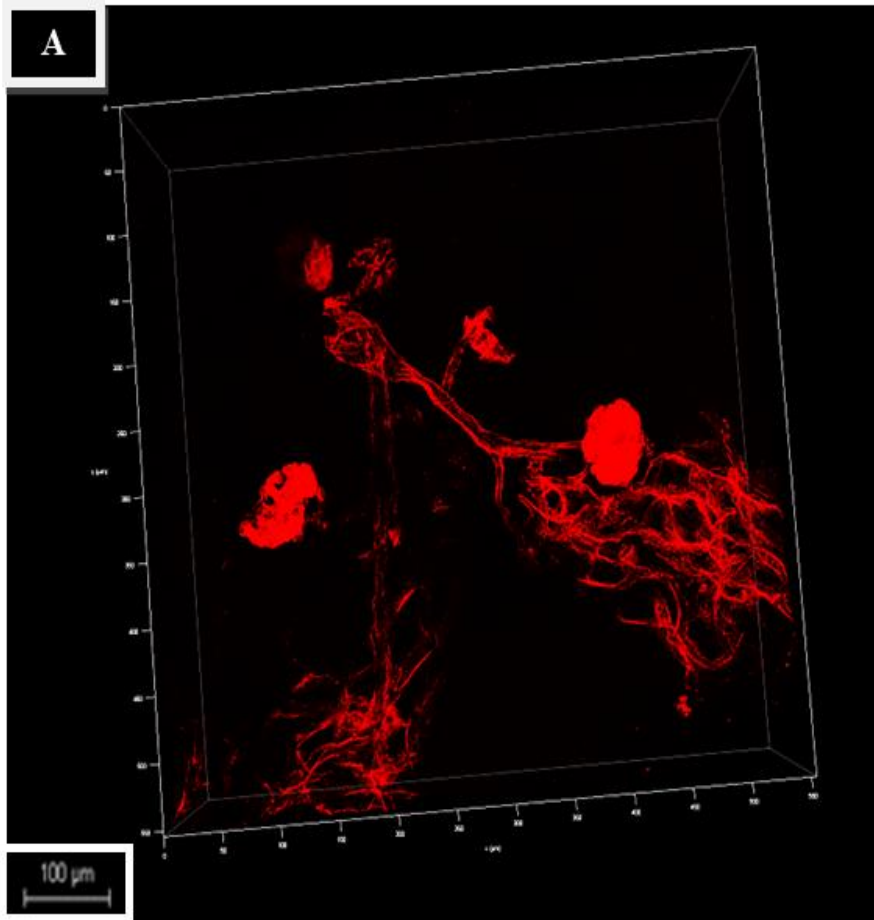


**Figure 4.6**: 3D Sections of mouse kidney, stained with Cy7-PEI-opt, acquired by CM, using a 20x objective in immersion oil and the 638 channel. A) and B) view, respectively without and with depth coding. As indicated from the depth bar on the right side of the image B), the depth reached is 220 μm. This scale goes from the surface of the sample (0-80μm, in blue-light blue), middle part (80-200μm, in green-yellow-orange) up to the deepest part of the region (200-220μm, in red). Scale bars: 100μm.
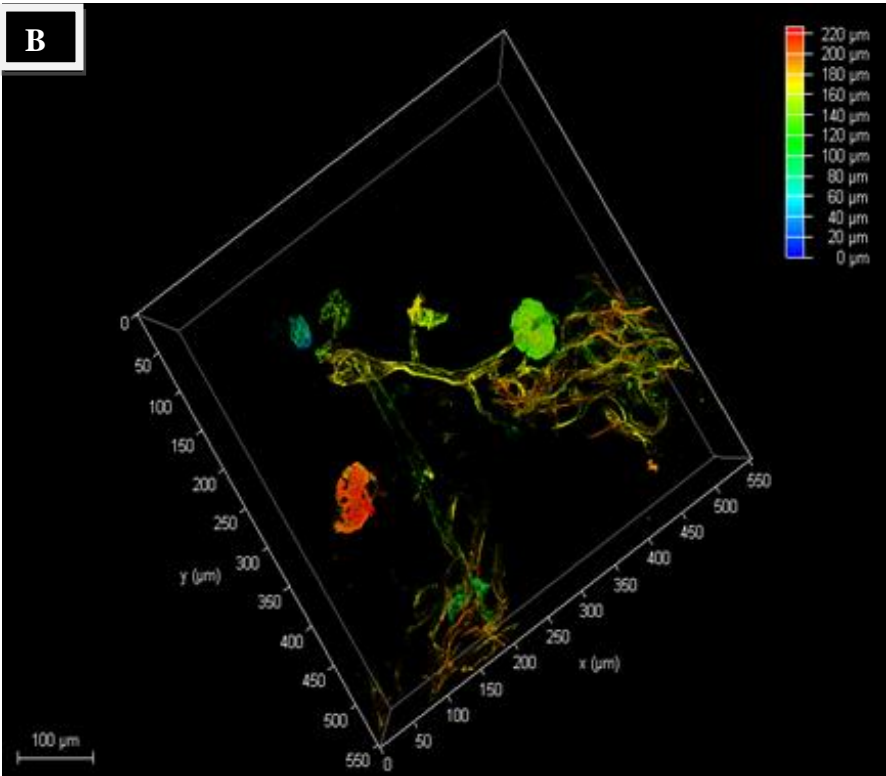
Figure 4.7 is a result of the recently new installed Stage Overview feature. With that, it has been possible to image larger sections compared to the previous ones. This is one example, where in A) it is possible to visualise and easily distinguish many glomeruli linked to the renal blood vessels. A depth coding view is given in B), where the glomeruli have been detected in different points of depth, as indicated from the depth coding on the right side of the image.
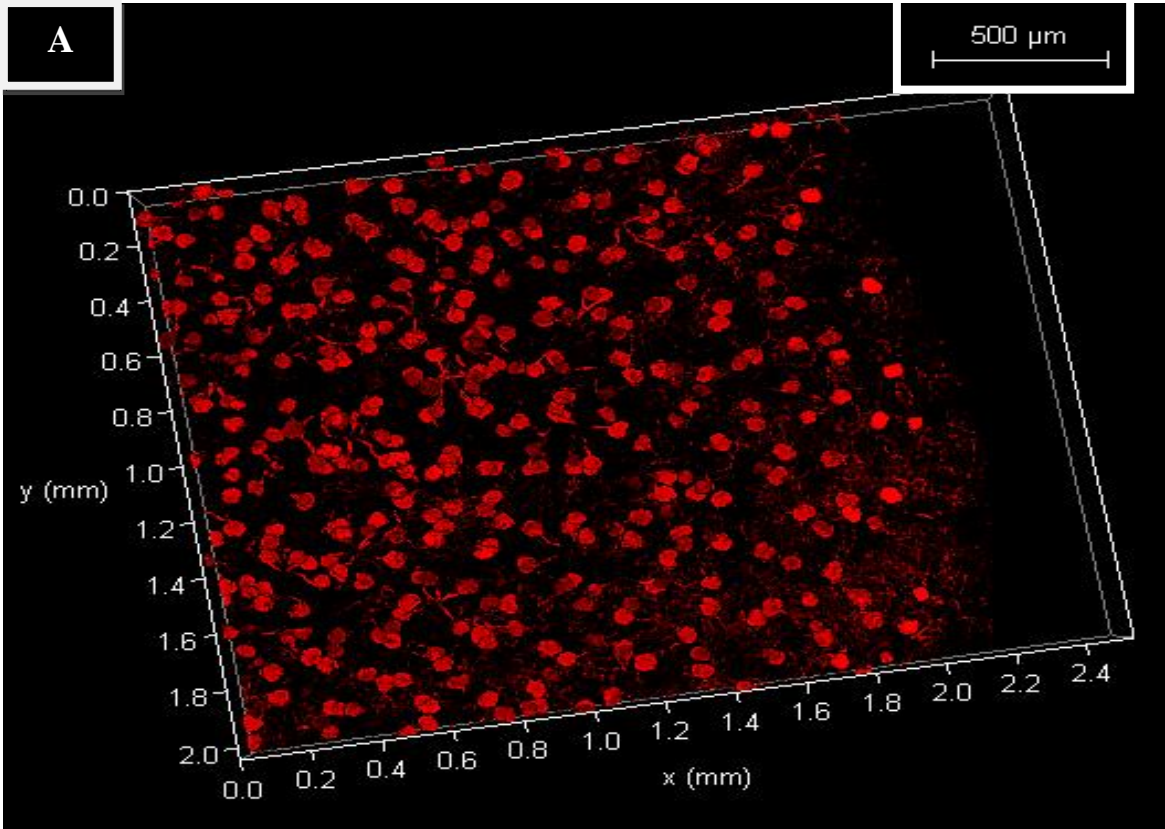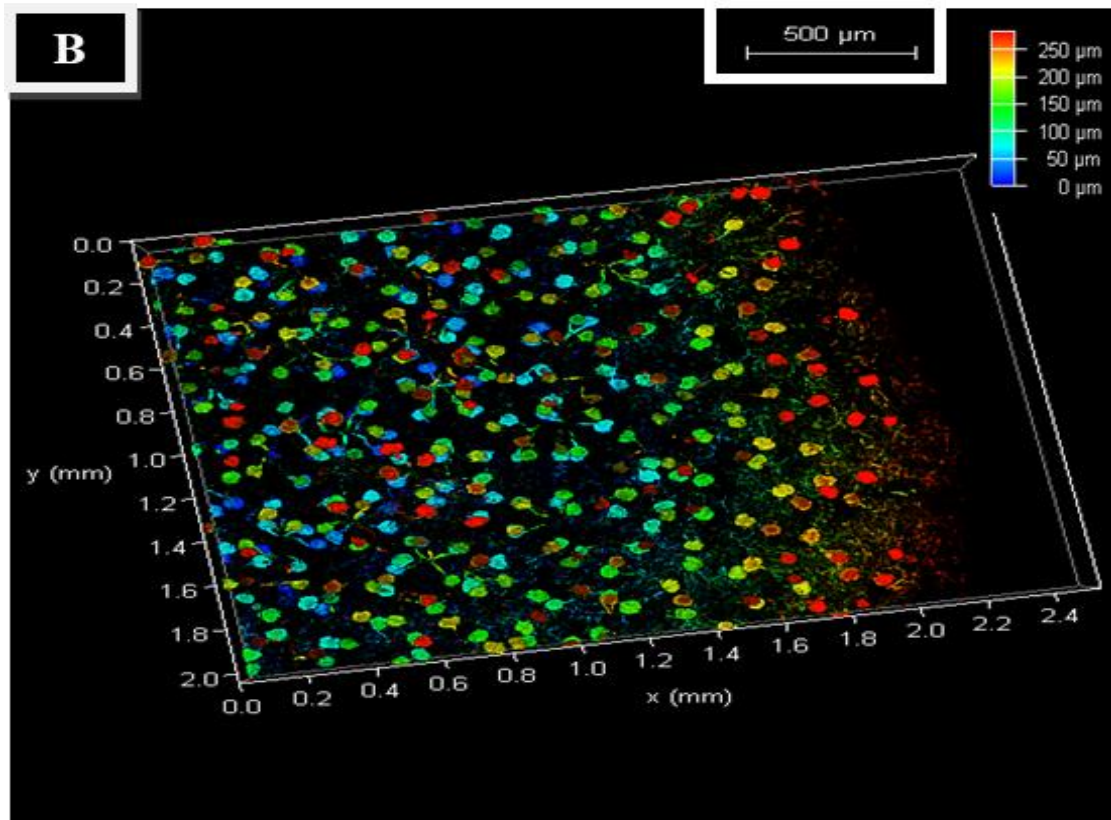
**Figure 4.7**: Section of mouse kidney imaged by CM, using a 20x objective in immersion oil and the 638 channel. A) 3D Tile Scan, acquired using the Stage Overview option from LasX software. B) 3D Tile Scan in depth coding. As indicated from the depth bar on the right side of the image, the depth reached is around 250µm. This scale goes from the surface of the sample (0-100µm, in blue-light blue), middle part (100-200µm, in green) up to the deepest part of the region (200-250µm, in yellow- red). Scale bars: 500µm

**Mouse Kidney: LightSheet Microscopy**

In Figure 4.8 a mouse kidney pole imaged by LSM is shown. The depth coding view describes the depth reached, equal to 1.4mm. The background noise is barely noticeable and the glomeruli are clear and distinguishable as single entities. This is a further confirmation of the efficacy of the use of Cy7-PEI combined to the ECi-based OTC. Figure 4.8 A) shows the whole pole, whereas in B) a zoomed in detail is given.
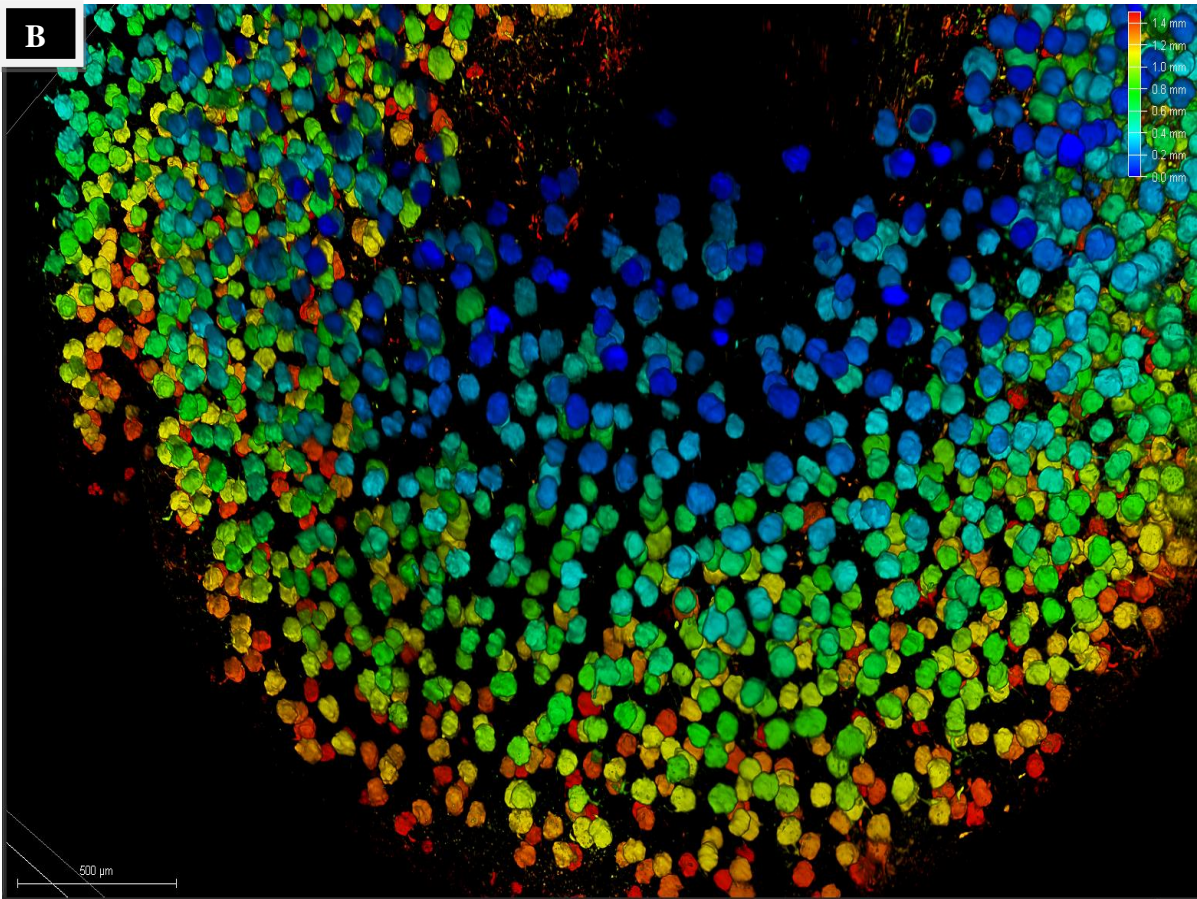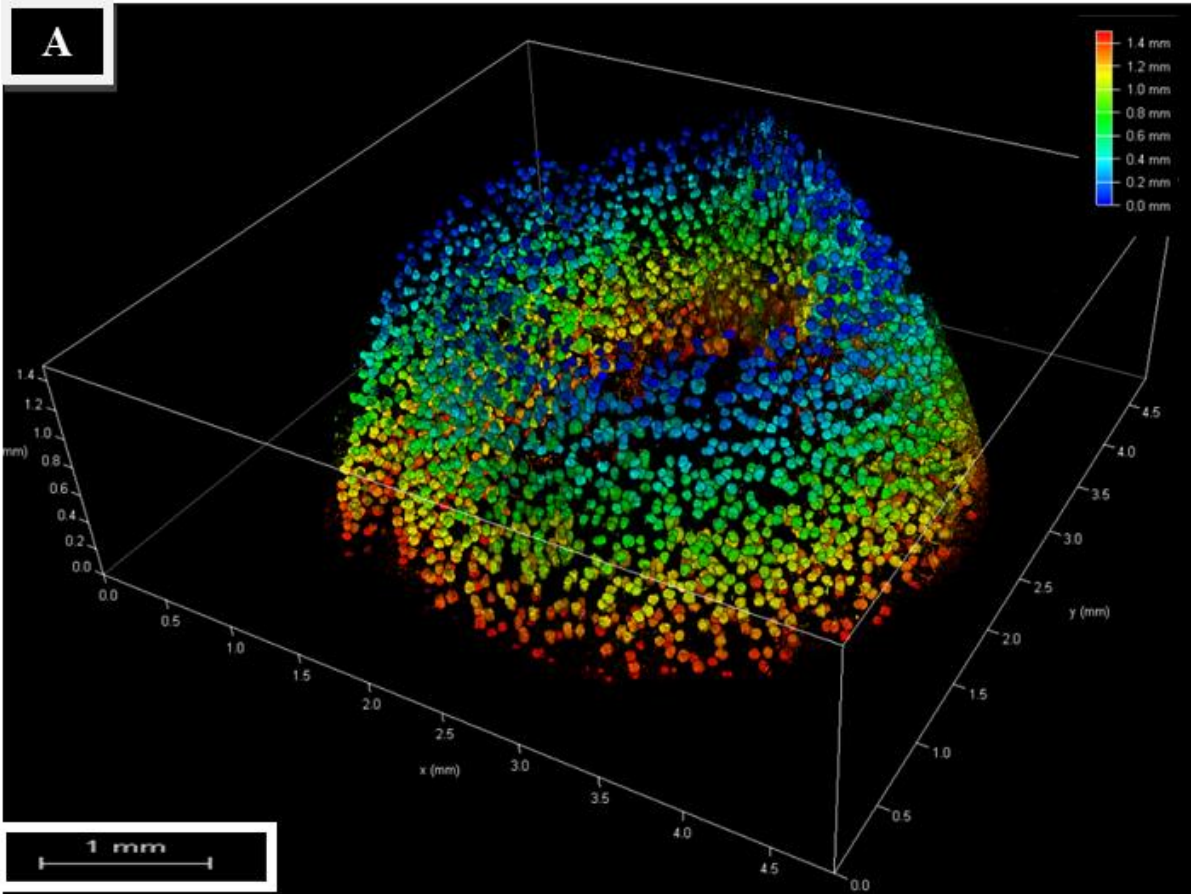
**Figure 4.8**: Depth coding view of a kidney pole from mouse, imaged by LSM, using a 5x objective in ECi and 638 channel. A) Pole from mouse kidney (corresponding to 1/3 of the whole kidney) imaged for 1.4mm. As indicated from the depth coding on the right side of the images, the scale goes from the surface (0.0-0.4mm, in blue), middle part (0.4-1.2mm, in green-yellow) up to the deepest part (1.2-1.4mm, in orange-red). Scale bar: 1mm. B) Detail from a zoom in view of the picture. Scale bar: 500μm.

Figure 4.9 shows a mouse kidney pole, stained with halved concentration of Cy7-PEI (1.5mg/ml) and imaged by using LSM. Despite the reduction of the dye concentration, the glomeruli are anyway well visible and recognizable, with a very low background noise level. Moreover, this 3D image could be suitable also for counting and quantification.
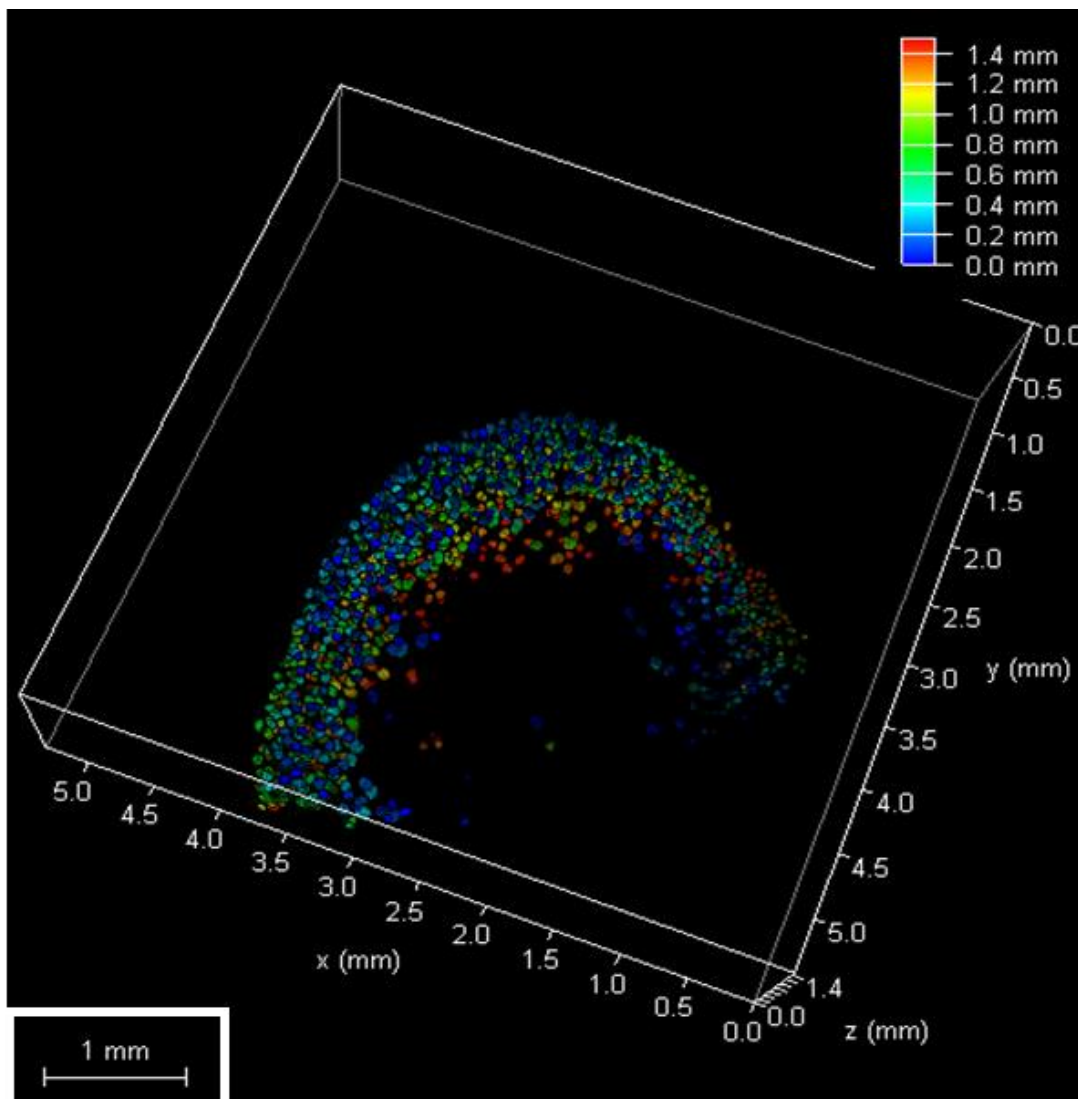


**Figure 4.9**: Depth coding view of a kidney pole from mouse (corresponding to 1/3 of the whole kidney) stained with Cy7-PEI in 1.5mg/ml as concentration and imaged by LSM, using a 5x objective in ECi, with 488 and 638 lasers. Total depth: 1.4mm. As indicated by the depth coding on the right side of the image, the scale goes from the surface (0.0-0.4mm, in blue-light blue); middle part (0.4-1.2mm, in green-yellow); deepest part (1.2-1.4mm, in orange-red). Scale bar: 1mm.

Figure 4.10 (A and B) was acquired after perfusing with Cy7-PEI in 1mg/ml as concentration and clearing. Despite the strong reduction in concentration of the dye, the images clearly demonstrate the presence of blood renal vessels, to which some glomeruli are linked to. In figure A), the glomeruli are more sharp compared to B), although in both A) and B) it is possible to see truly "through" the renal blood vessels.
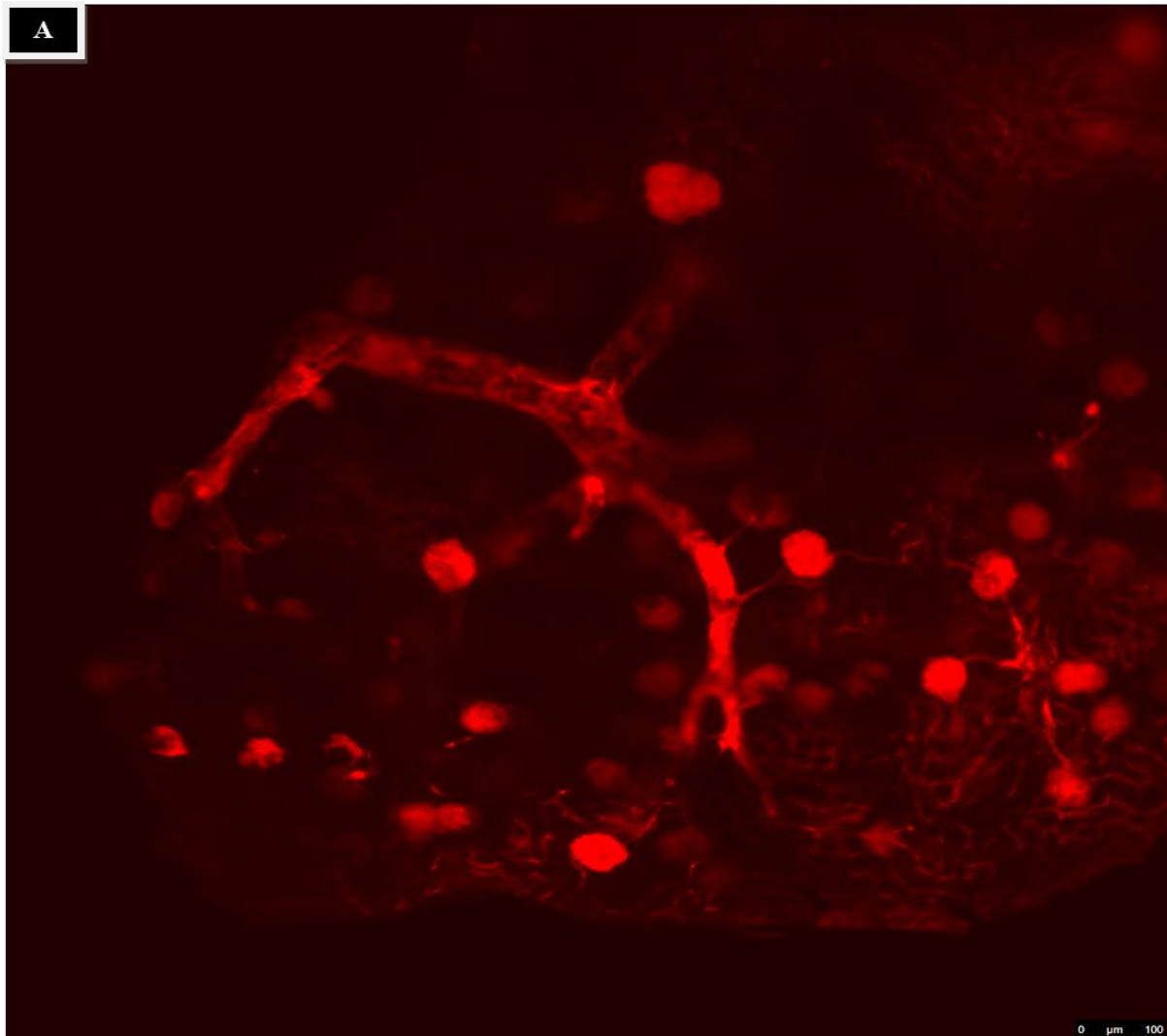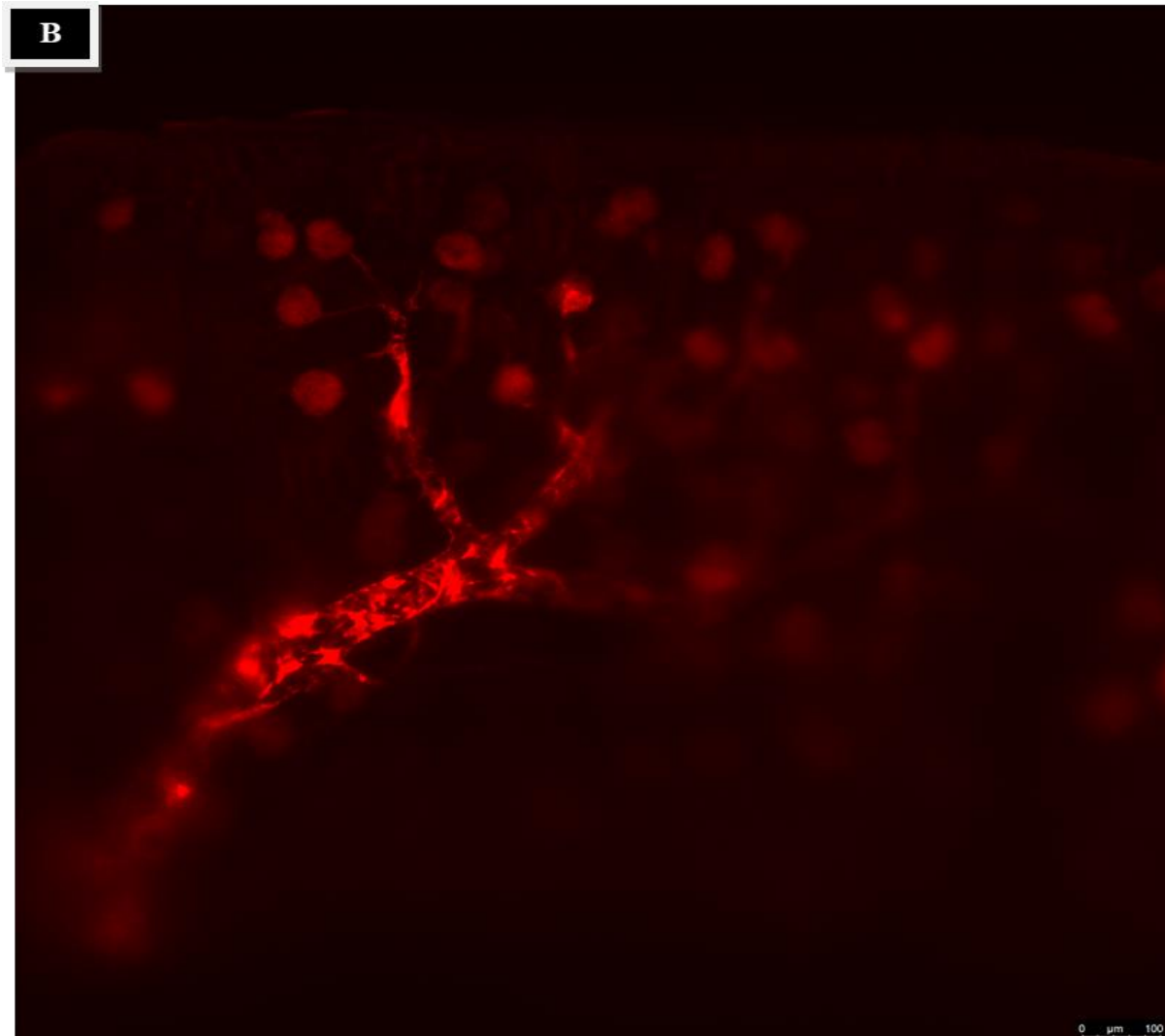
**Figure 4.10**: Renal blood vessels from a mouse kidney pole stained with Cy7-PEI in 1mg/ml as concentration and imaged by LSM, using a 5x objective in ECi and 638 channel. Both images A) and B) show renal afferent artery, connecting to some glomeruli. Scale bars: 100µm

### 4.4.2 ECi-based OTC: different mouse samples

In this section, images from female WT C57BL/6 mouse heart, lung, liver, spleen, will be shown. In the interest of simplicity and unless stated otherwise, all the images are intended acquired by CM after perfusion and staining with Cy7-PEI in 3mg/ml as concentration.

**Mouse Heart**

The 3D image shown in Figure 4.11 was acquired after perfusion with Cy7-PEI-opt 4F (4F: filtered 4 times) and stored in ECi for 26 days. Before the imaging, the thin section was mounted following the method b) described in the paragraph 4.3.1. As indicated by the depth scale in figure B), although only 60µm were imaged, a detailed set of cardiac blood vessel is

clearly described. As revealed by this image, this is characterized by a big artery and its branches surrounded by several capillaries, which are very well defined and easy to follow.
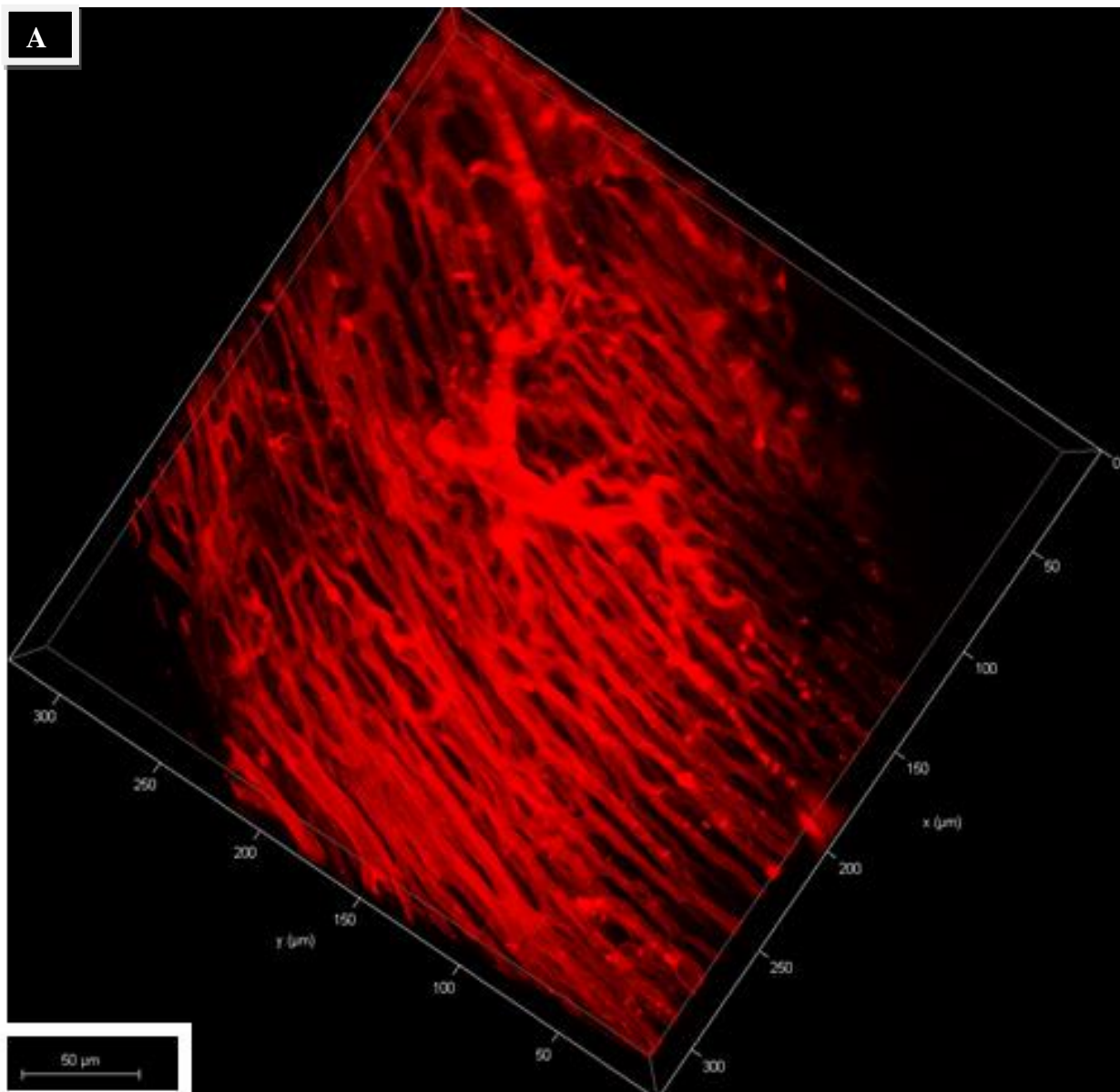


**Figure 4.11**: Section of heart from mouse, stained by Cy7-PEI-opt 4F (3mg/ml) and imaged by CM, using a 20x objective in immersion oil and 638 channel. A) 3D image. B) 3D image in depth coding. As indicated by the scale on the right side of the image, the scale goes from the surface (0-20µm, in blue-light blue); middle part (20-50µm, in green-yellow); deepest part (50-60µm, in orange-red). Scale bars: 50µm.
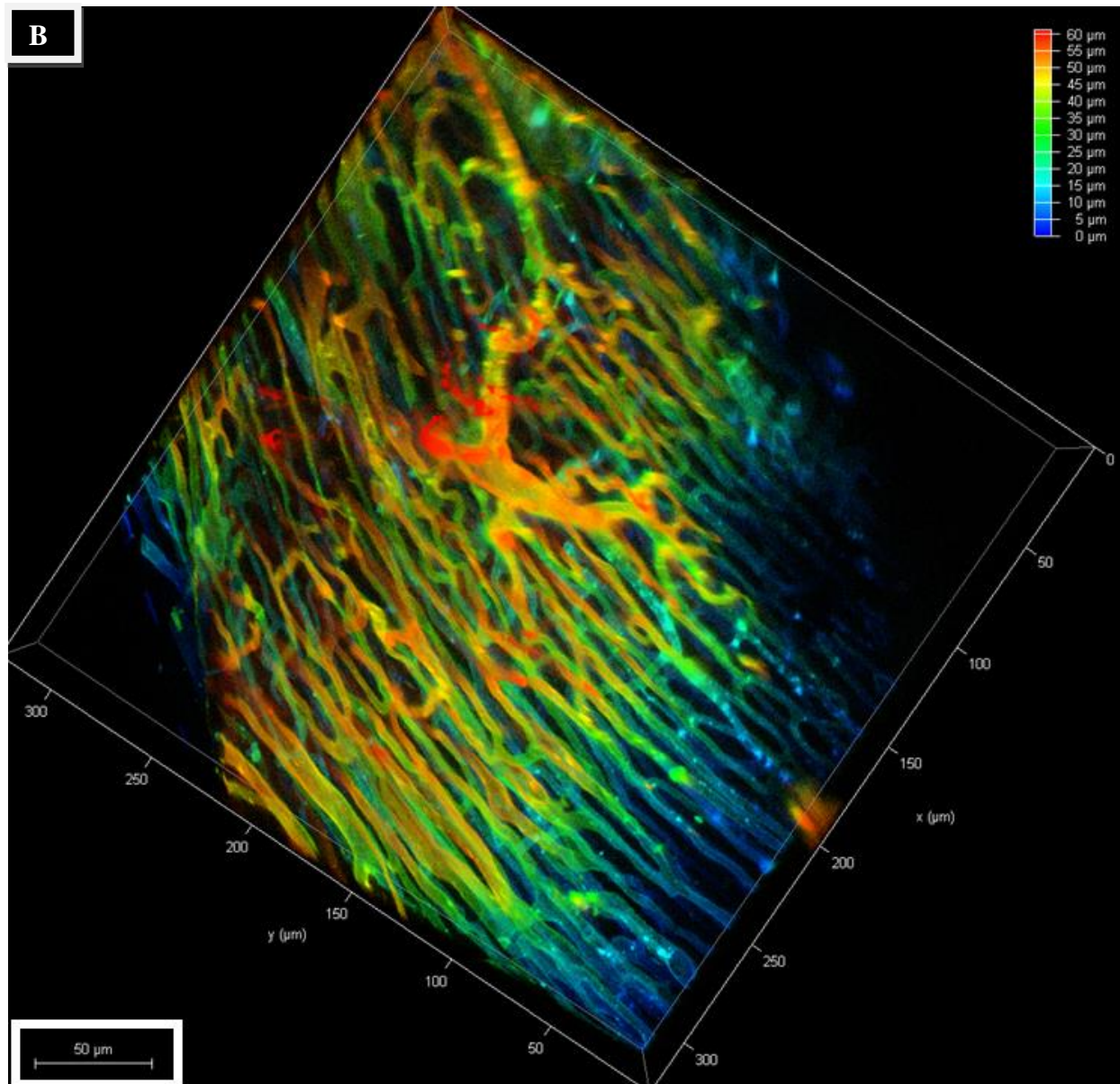
**Mouse Lung**

Figure 4.12 (A, B, C) concerns another staining, made with nanoparticles, injected via intraperitoneal prior to the perfusion. In particular, the one which the images are referred to is the NP510N-Alexa647 conjugated (Thermofischer Scientific, Germany). The maximum absorbance and emission are, respectively, 651nm and 672nm; therefore, this is located in the NIR of the spectrum. These images show the alveolar structures as well as the blood vessels, which are well recognizable. Barely perceptible is the background noise level.
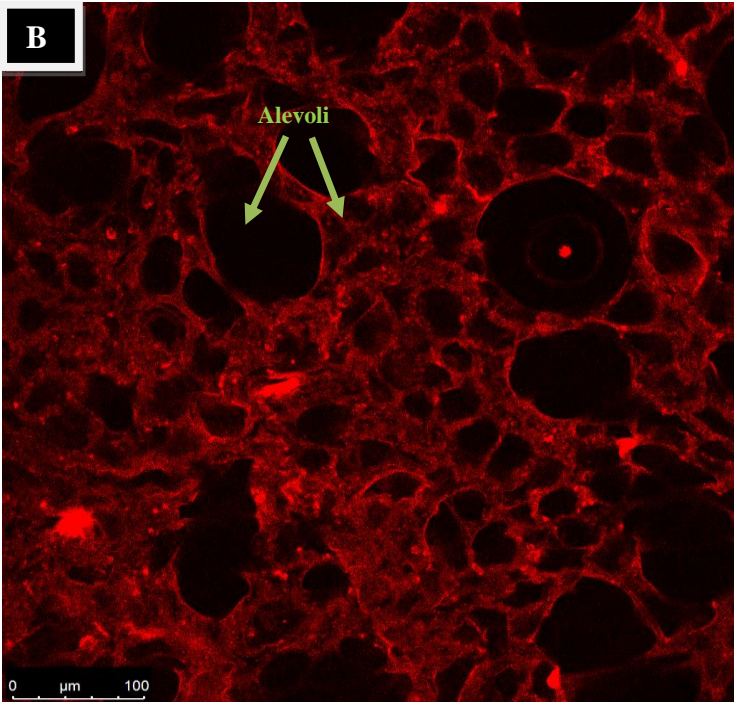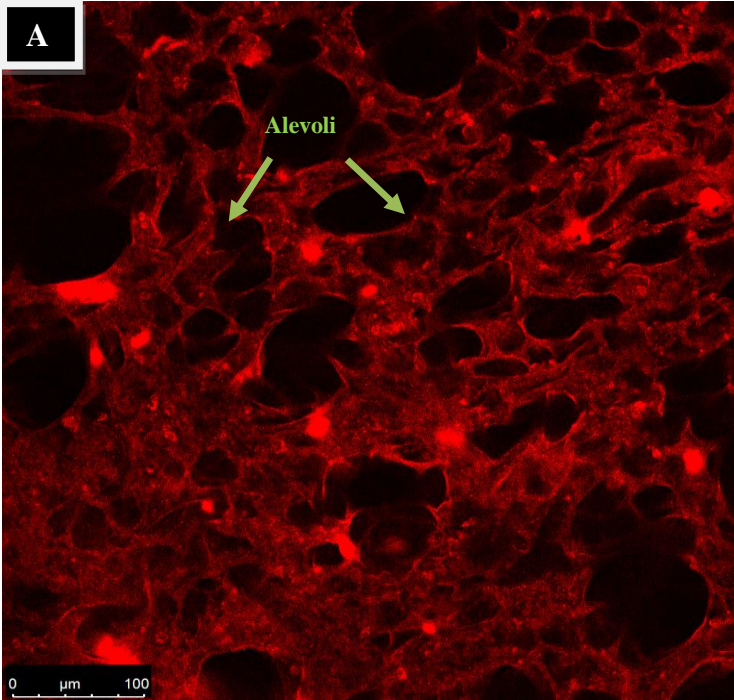
**Figure 4.12**: Mouse lung imaged by CM, stained with NP510N-Alexa647 conjugated, using a 20x objective in immersion oil and 638 laser. A, B and C represent three different regions of the same section, in 2D. Scale bars: 100µm.
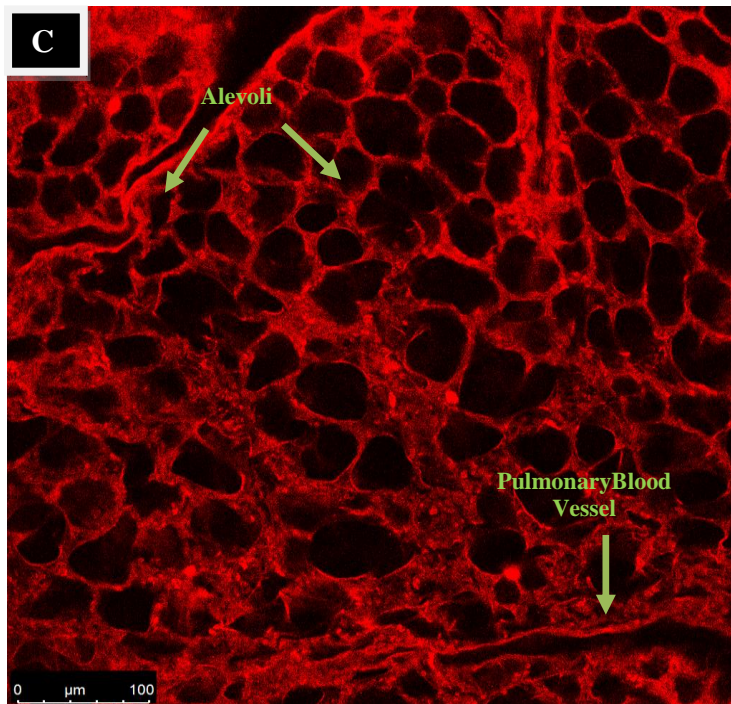
In Figure 4.13 a mouse lung, stained with WGA Alexa488 conjugated and imaged by CM is shown. A) and B) clearly display well defined 2D alveolar structures, whereas C) and D) represent the 3Ds, without and with depth coding respectively. Although, as indicated by the depth coding, the depth reached is not deep, all the pulmonary structures are well defined, both in 2D and in 3D. Even some bronchioles are recognizable. Moreover, in the whole pulmonary tissue, the background noise level is very low, demonstrating a) the good quality of the perfusion and b) the high efficacy of the ECi-based OTC.
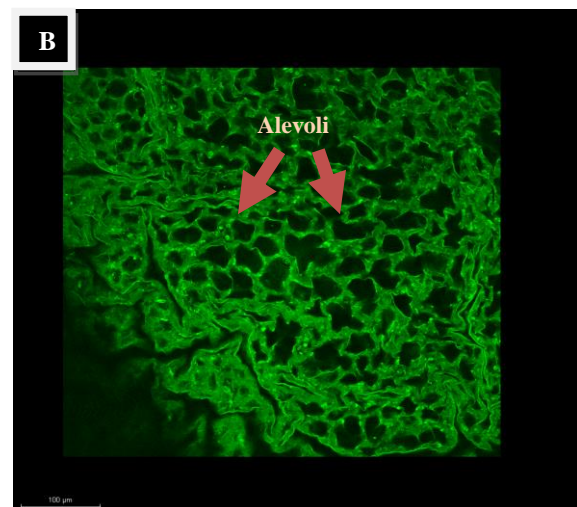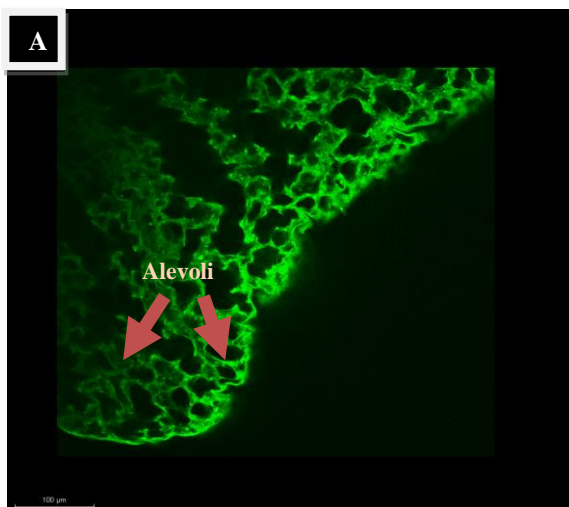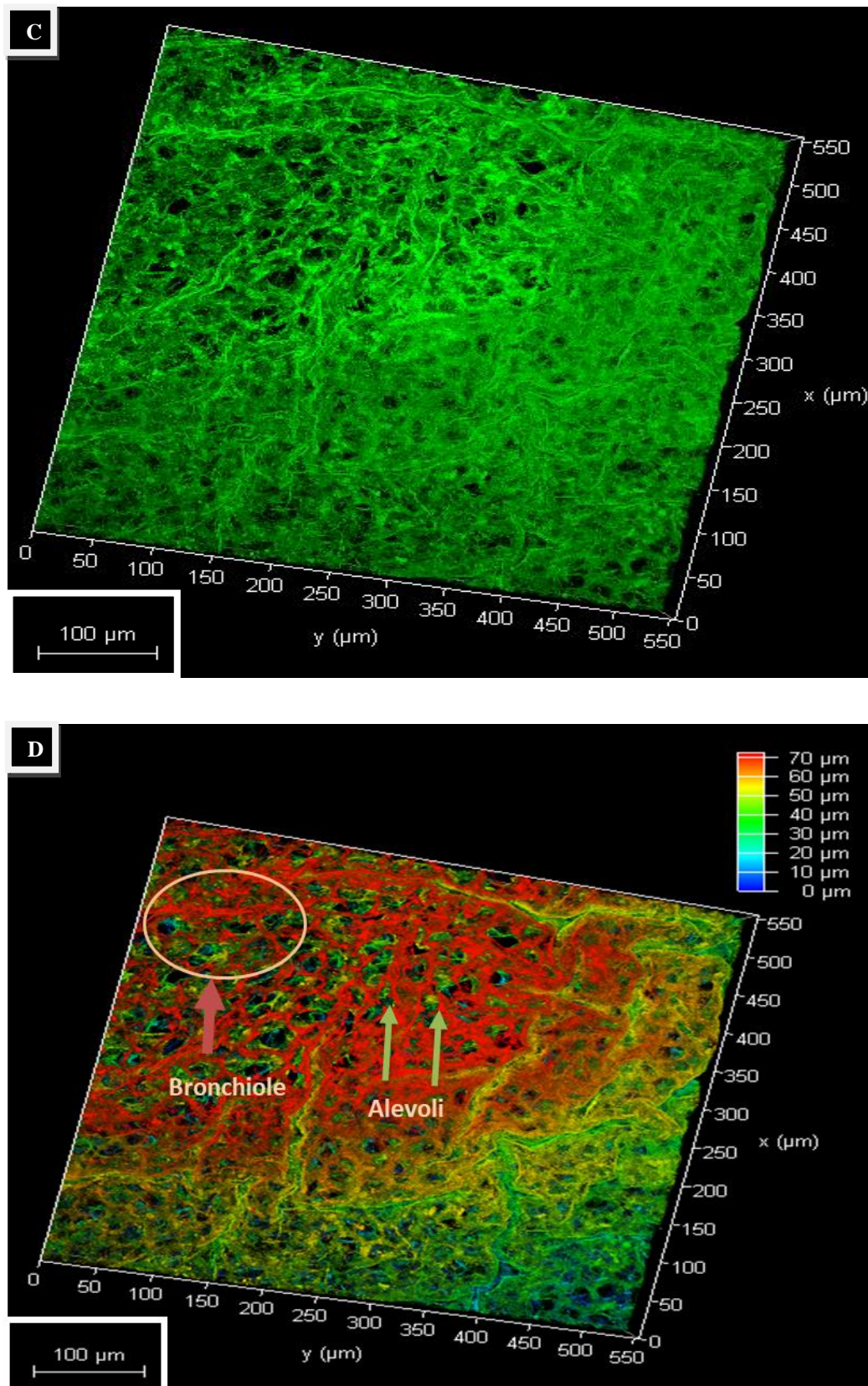
**Figure 4.13**: Section of mouse lung, stained with WGA-Alexa Fluo 488 conjugated (stock concentration 1mg/ml, diluted 1:1000 in a final volume of 20 ml of solution) and imaged by CM, using a 20x objective in immersion oil and 488 channel. A) and B) represent two different regions of the same section, in 2D. Scale bars: 100µm. C) 3D view. Scale bar 100µm. D) 3D depth coding view: As indicated by the scale on the right side of the image, this goes from the most superficial regions (0-20µm in blue-light blue), middle part (20-60µm in green-yellow) up to the deepest part (60-70µm, in red). Scale bar: 100µm.

Figure 4.14 shows a 3D mouse lung section, imaged by CM. The final depth reached is 200µm. The imaging proceeded and captured structural elements in all the points of the depth. Alveoli are well distinguishable.
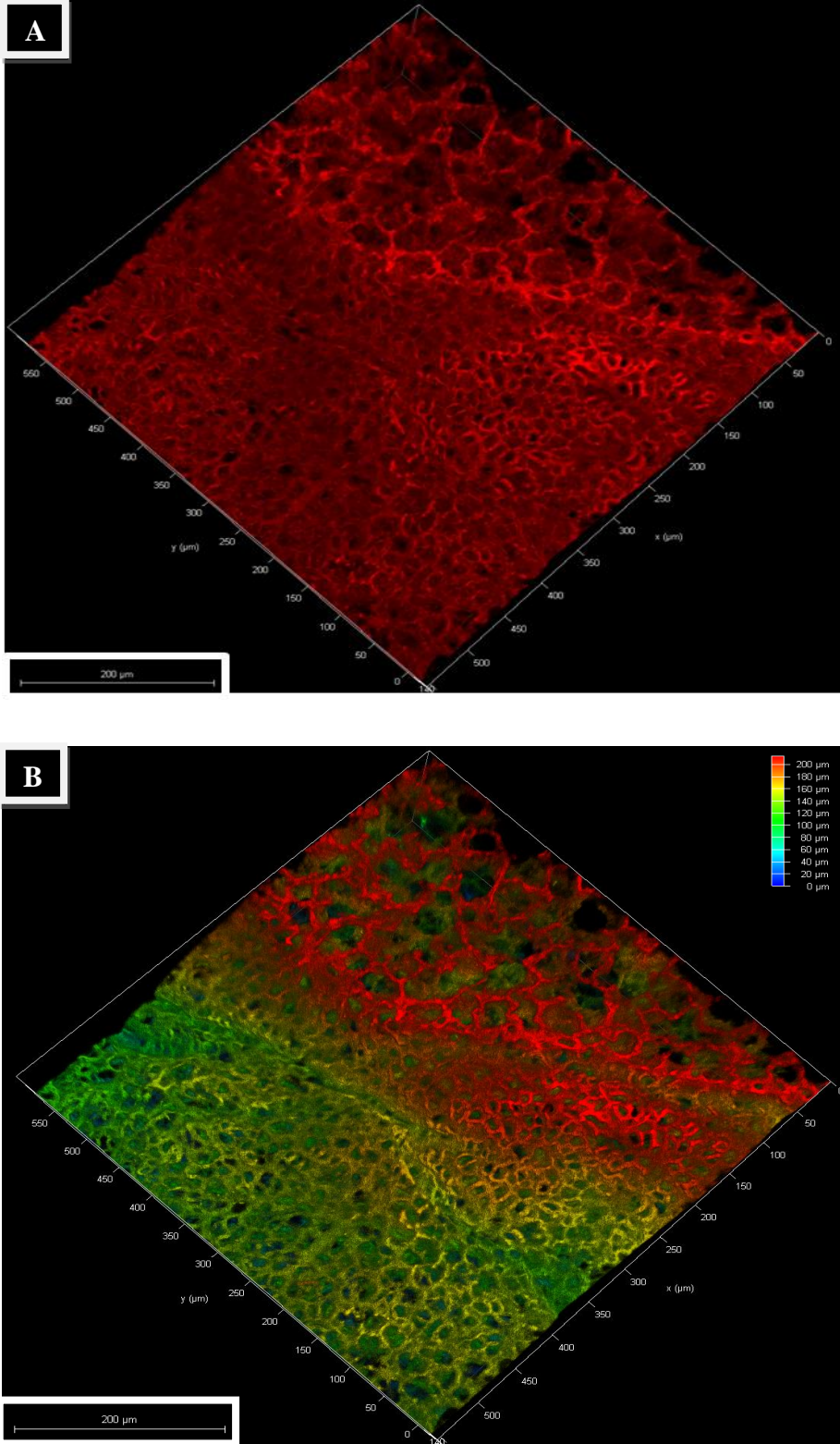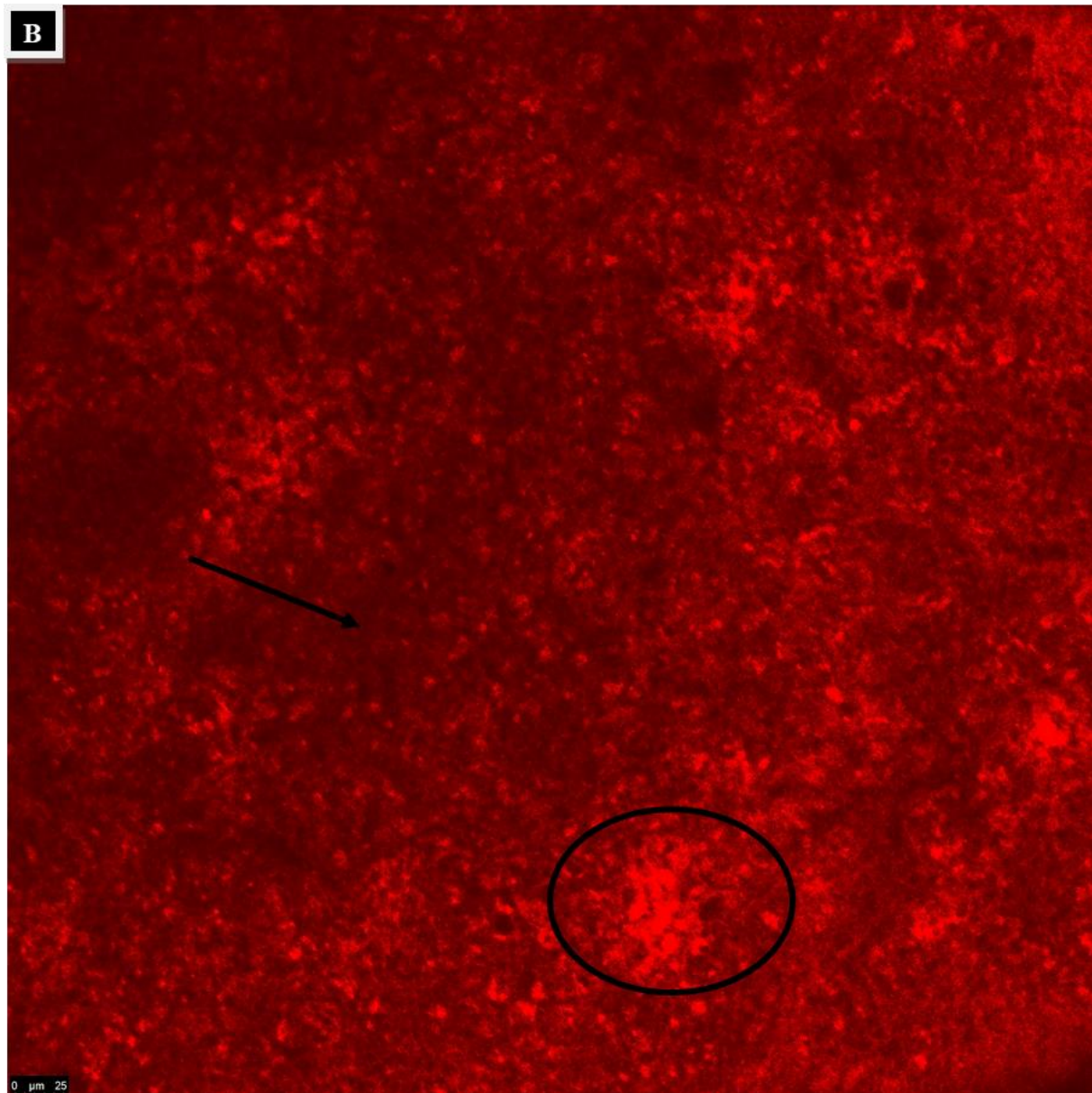


**Figure 4.14**: 3D mouse lung section, imaged by CM, using 20x objective in immersion oil and the 638 channel. A) 3D Tile Scan. B) Depth coding view: As indicated by the scale on the right side of the image, this goes from the most superficial regions (0-80µm in blue-light blue), middle part (80-180µm in green-yellow) up to the deepest part (180-200µm, in orange-red). Scale bars: 200µm

**Mouse Spleen**

Figure 4.15 represents the 2Ds of two different regions of the same spleen mouse sample. The main elements in there are the white and red pulps, underlined, respectively by the black round shape and black arrow. These are differentiated by the diverse brightness intensity.
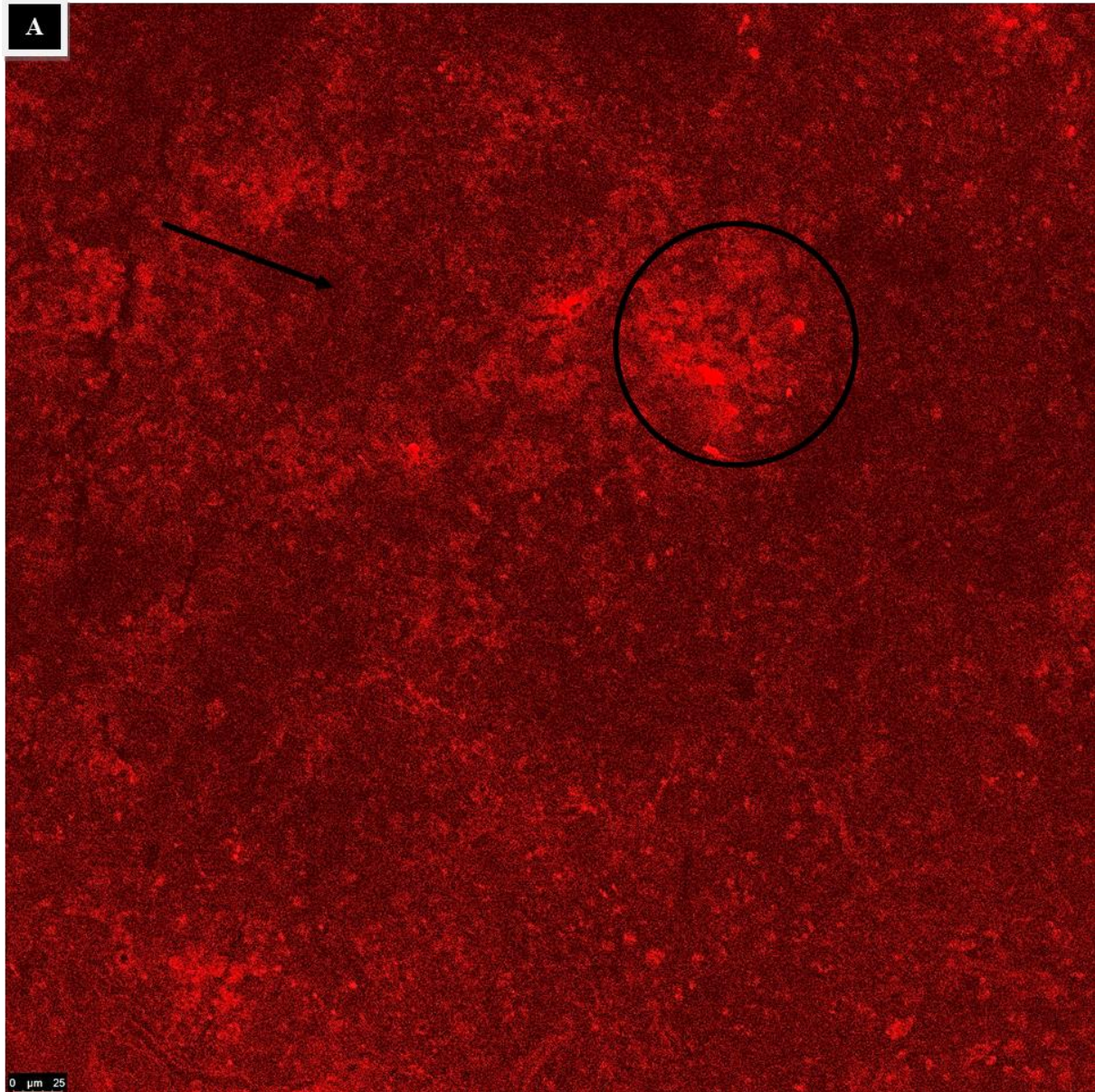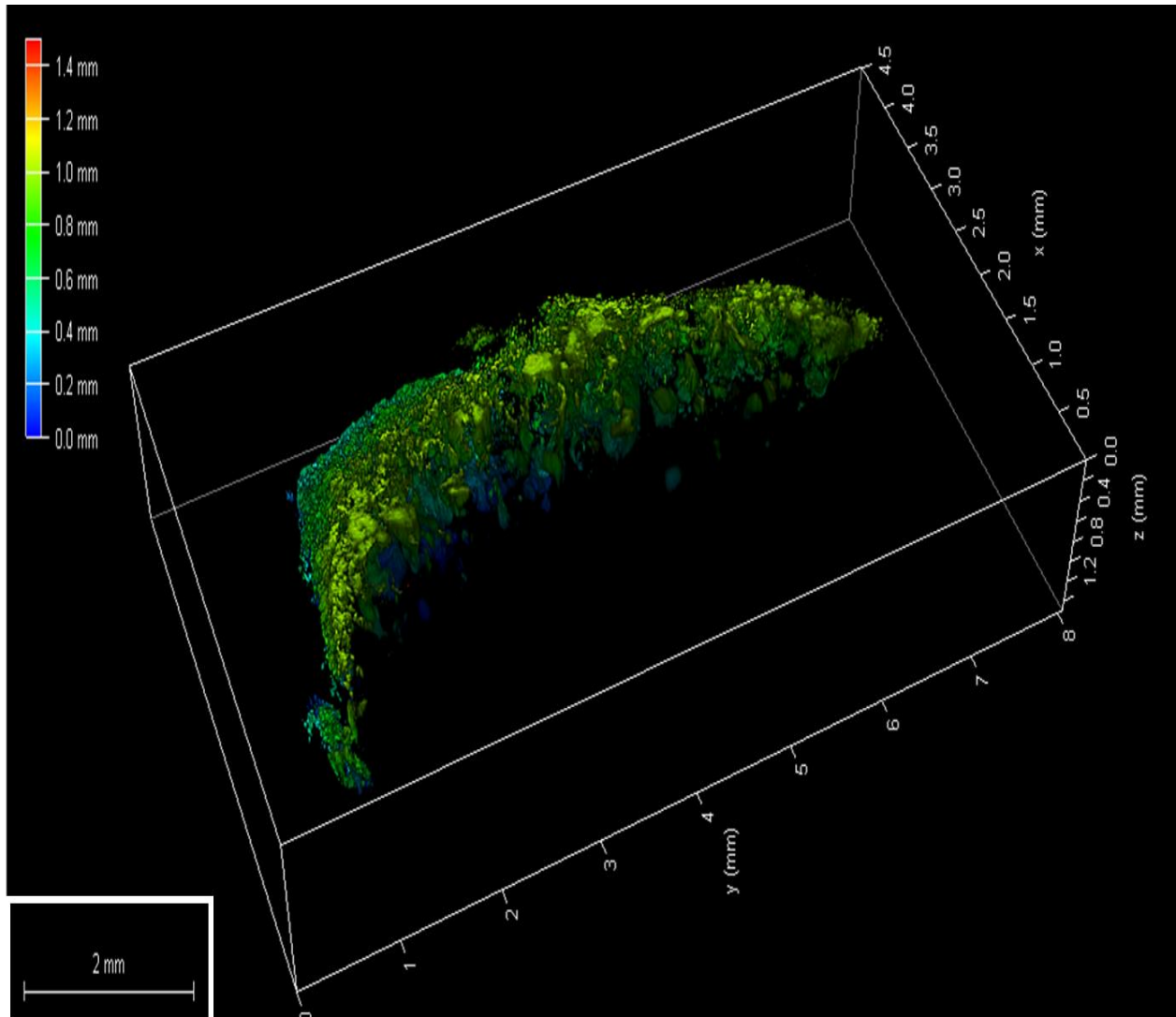
**Figure 4.15**: Spleen section from mouse, imaged by CM, using a 20x objective in immersion oil and the 638 channel. A) and B) show different regions of the same section in 2D. Scale bars: 25 μm

**Mouse Spleen: Light Sheet Microscopy**

The depth coding version of Figure 4.16 shows a very large section of mouse spleen imaged by LSM. Thanks to the longer working distance of the objective, a very wide depth was achieved. Additionally, this image shows also some structural details as white and red pulp.

**Figure 4.16**: Spleen section from mouse, imaged by LSM, using a 5x objective in ECi and the 638 channel. 3D Tile scan view in depth coding. As indicated by the scale on the right side of the image, this goes from the most superficial region (0.0-0.6mm in blue-light blue), middle part (0.6-1.2mm in green-yellow) up to the deepest part (1.2-1.4mm, in orange- red) Scale bar: 2mm

Figure 4.17 shows a mouse spleen, stained with halved concentration of Cy7-PEI (1.5mg/ml). Despite the reduction in concentration of the dye, all the main spleen structural elements are easily detectable. In fact, from the outside it is possible to identify the connective capsule, surrounding all the spleen. Within, the main components of this organ: the white and red pulp: this latter is viewable as a set of red dots. In that it is present the connective tissue, known as cords of Billroth and a spleen artery clearly visible with its branches.
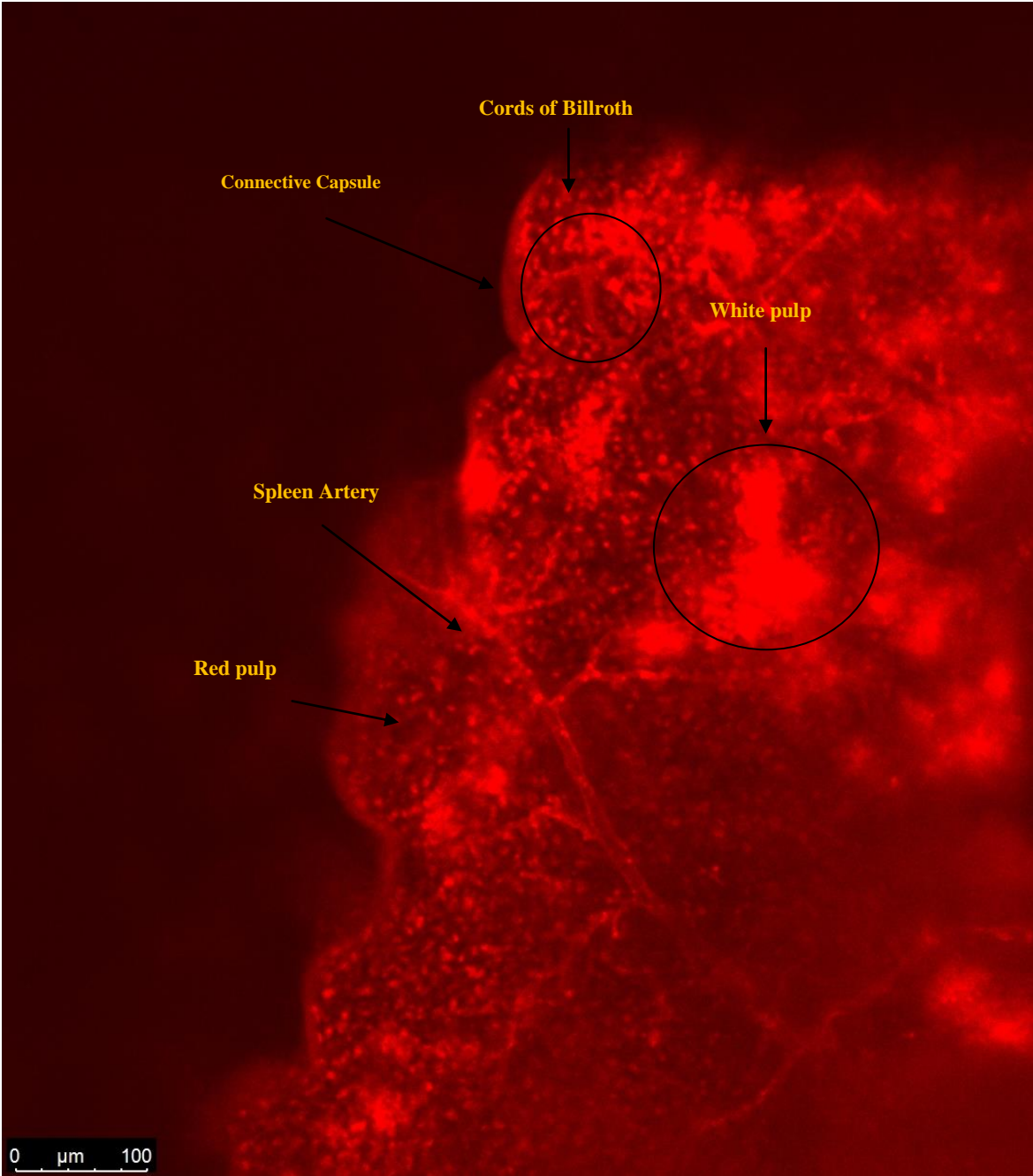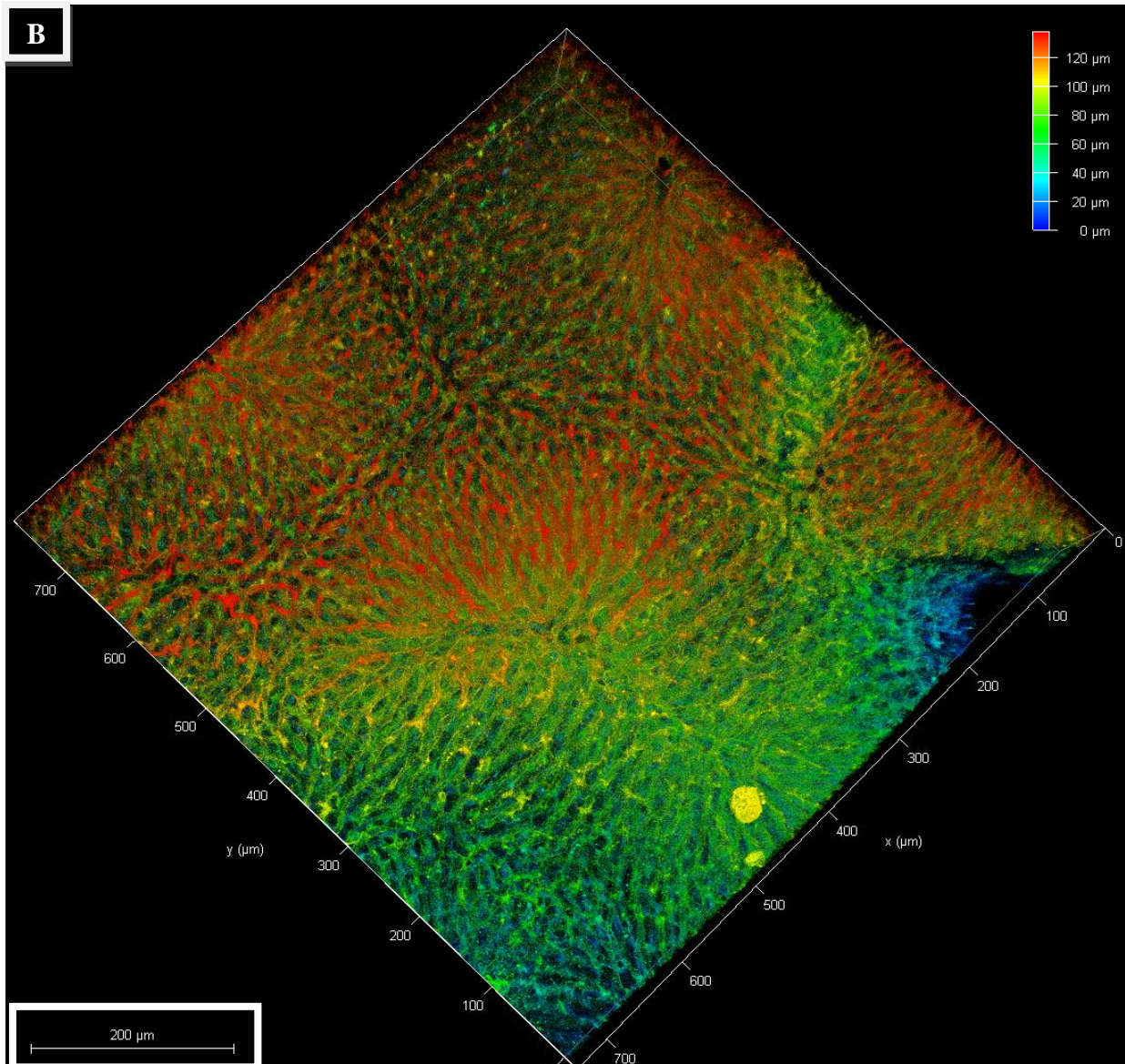
**Figure 4.17**: 2D mouse spleen section stained with Cy7-PEI in 1.5mg/ml and imaged by LSM, using a 5x objective in ECi and the 638 channel. Scale bar: 100μm

**Mouse Liver**

In Figure 4.18 another example of 3D mouse liver, imaged by CM, is shown. Sinusoids and hepatocytes are clearly distinguishable. These are underlined by the light-green arrows. Figure B) is the depth coding view.
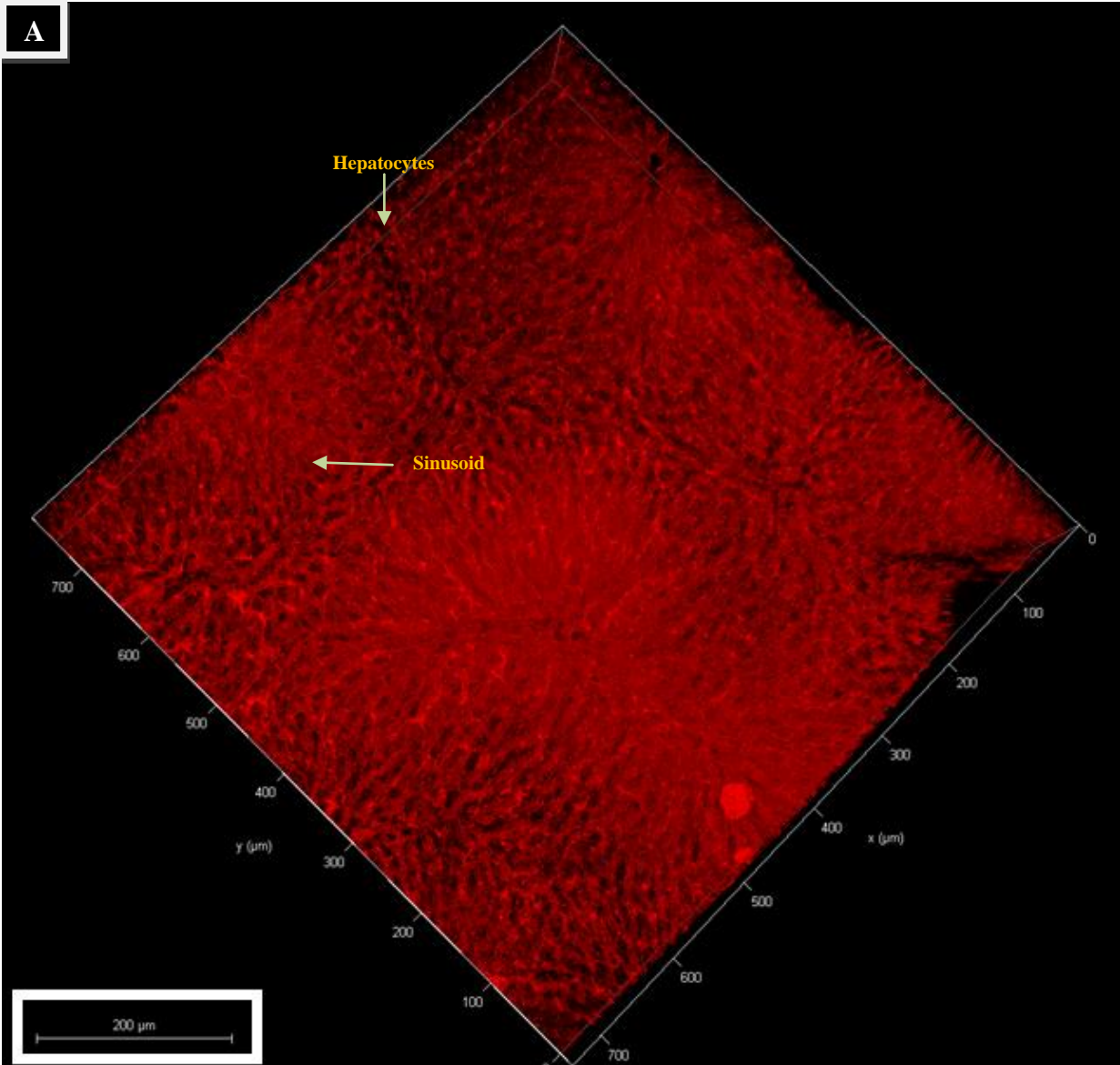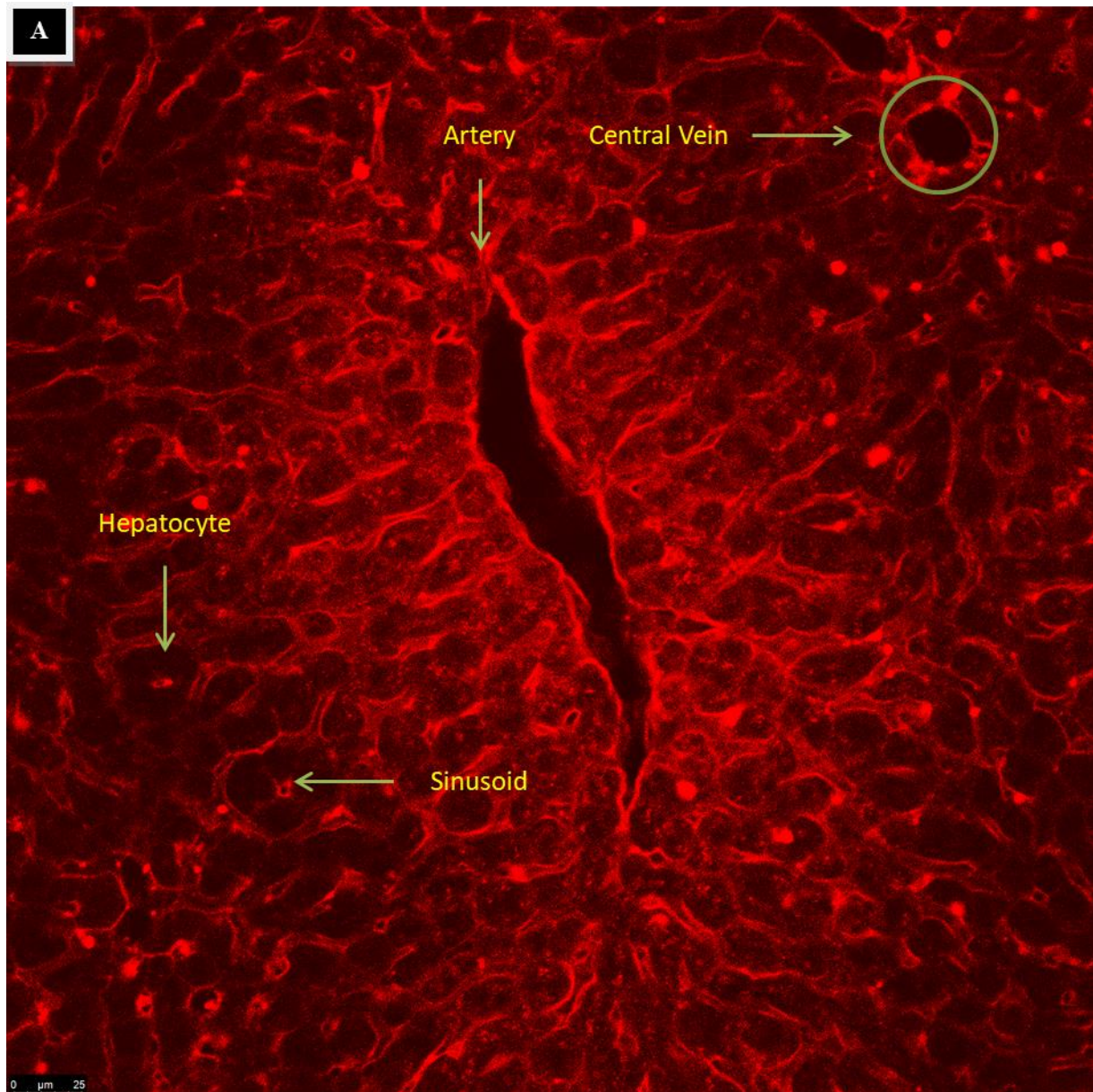
**Figure 4.18**: Liver section from mouse, imaged by CM, using a 20x objective in immersion oil and the 638 channel. A) 3D view. Scale bar: 200µm. B) 3D view in depth coding: as indicated by the scale on the right side of the image, this goes from the most superficial region (0-40µm in blue-light blue), middle part (40-100µm in green-yellow) up to the deepest part (120µm, in red) Scale bar:200µm

A further example of the imaging of mouse liver is given by Figure 4.19: A) shows in 2D all the main hepatic tissue elements (indicated in the figure). In addition to the central vein, sinusoids and hepatocytes, also an artery is shown. B) and C) are the 3Ds, with and without depth coding, respectively. The depth reached is 140µm.

**Figure 4.19**: Mouse liver section, imaged by CM, using a 20x objective in immersion oil and the 638 channel. A) 2D view. Scale bar: 25μm. B) 3D view. C) 3D view in depth coding: as indicated by the scale on the right side of the image, this goes from the most superficial region (0-40μm in blue-light blue), middle part (40-120μm in green - yellow) up to the deepest part (120-140μm, in red) Scale bars: 200μm
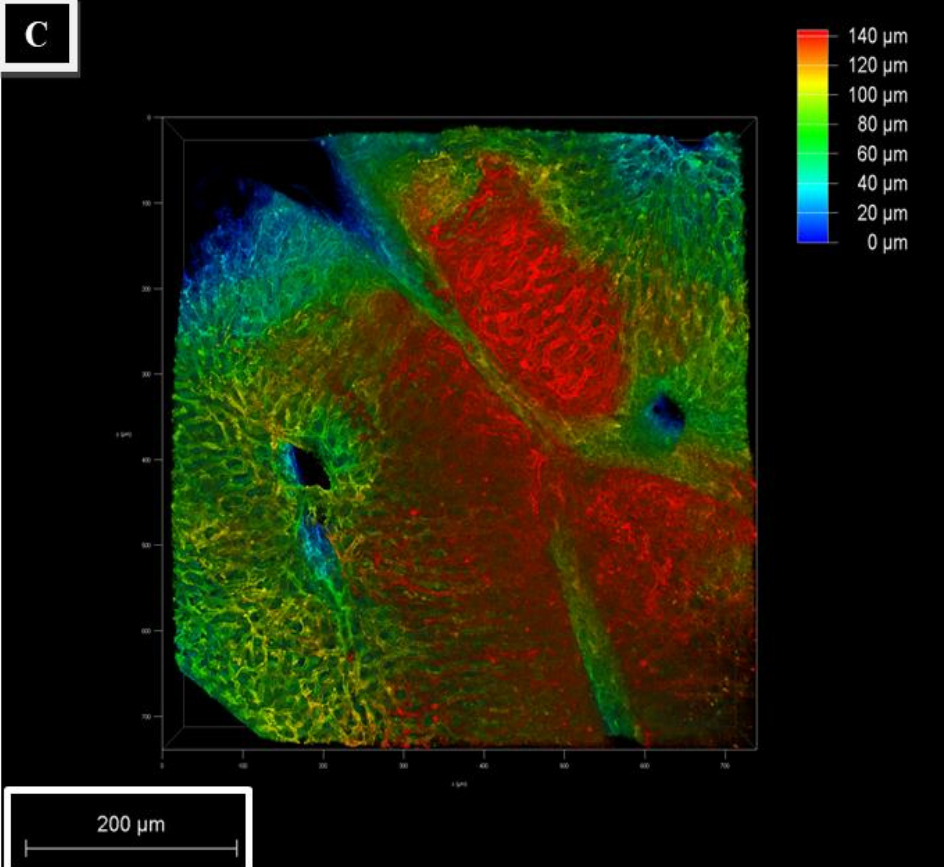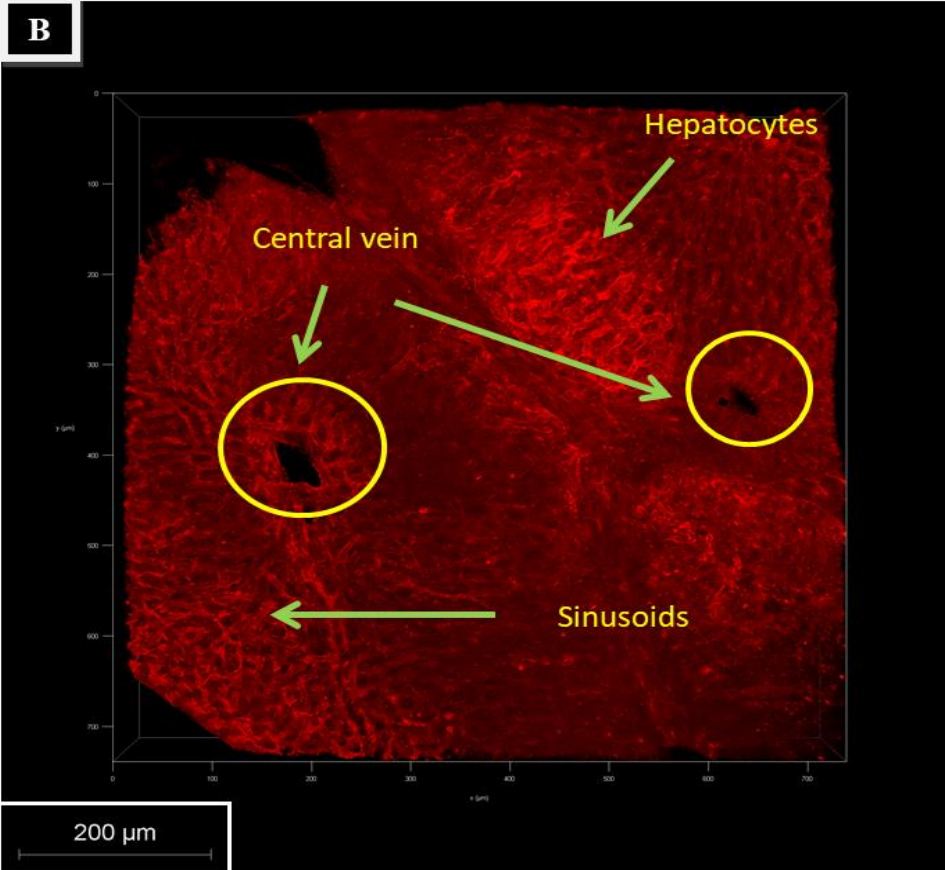
### 4.4.3 ECi-based OTC: Results from pathological samples

In order to understand whether the ECI-based OTC would have been suitable also on pathological samples, in the following some results from rat samples, characterized by different diseases, will be reported.
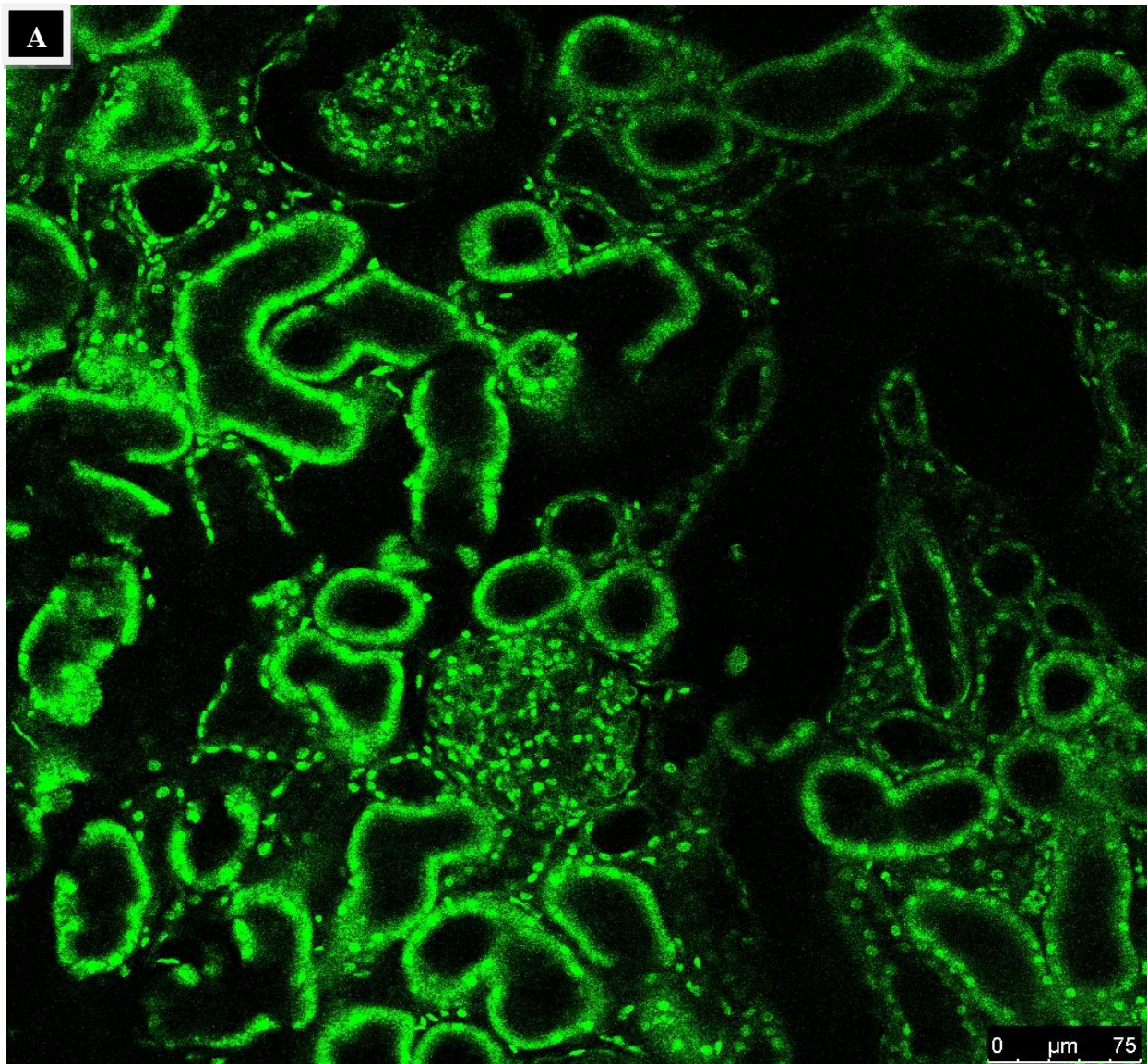
### CISPLATIN RAT

As part of the project G14/13, carried out by Cristina Daniele, under the supervision of Prof. Dr. med. N. Gretz, some kidneys from male Sprague Dawley (SD) rats, treated with cisplatin (TEVA, 1mg/ml ready to use solution; used in a dose of 7mg/kg BW) in order to cause kidney injury, were provided to be cleared and imaged. Prior to the perfusion, the rats were treated by injections of cisplatin. As it is described in Table 4.6, the perfusion procedure, performed after 14 days from the first injection of cisplatin, was slightly modified, as the timing and the pressure used were adapted for rats, although the injection of the dyes were kept to the same rate as previously described (1ml/min). For these experiments a double staining was used, made with WGA and Cy7-PEI. The working concentrations for both dyes were kept the same as usual.

| REAGENT | TIME (min) | PRESSURE(mbar) |
|---|---|---|
| NaCl pH 7.4+ hep | 3 | 280 |
| Cy7-PEI | 1 | 230 |
| NaCl pH 7.4+ hep | 1 | 230 |
| WGA | 1 | 230 |
| NaCl pH 7.4+ hep | 1 | 230 |
| 4% PFA | 3 | 230 |
| **Table 4.6**: Perfusion protocol used for SD rats. | | |

In order to assess whether it could have been possible to use the CM technology to analyze in depth the main elements of cisplatin-induced AKI, the following images were acquired during the animal model establishment phase. Figure 4.20 (A, B, C) shows many hallmarks of the cisplatin-induced AKI, mentioned before. First of all, a very high level of macrophage infiltrate is present (represented by the green dots), detected in all of the three images. Tubular dilatation is also distinguishable. In addition, noticeable is the result of this differential. In fact, in A), the more visible elements are the renal tubuli and the macrophages, stained by WGA, while in B) the glomeruli are more easily detectable. This is in accordance with the different role of the two dyes: WGA is a lectin and it links to N-acetylnerumaninc acid, as

components of carbohydrates from cell membranes, which is, in turn, a prominent component of the macrophages. On the other hand, as already explained, Cy7-PEI was designed to bind directly to the glomeruli and blood vessels. Figure 4.20 C) shows the overlay between the two dyes, where the orange shades come from their overlapping. Again, even in the image in overlay, the macrophages are only green colored.
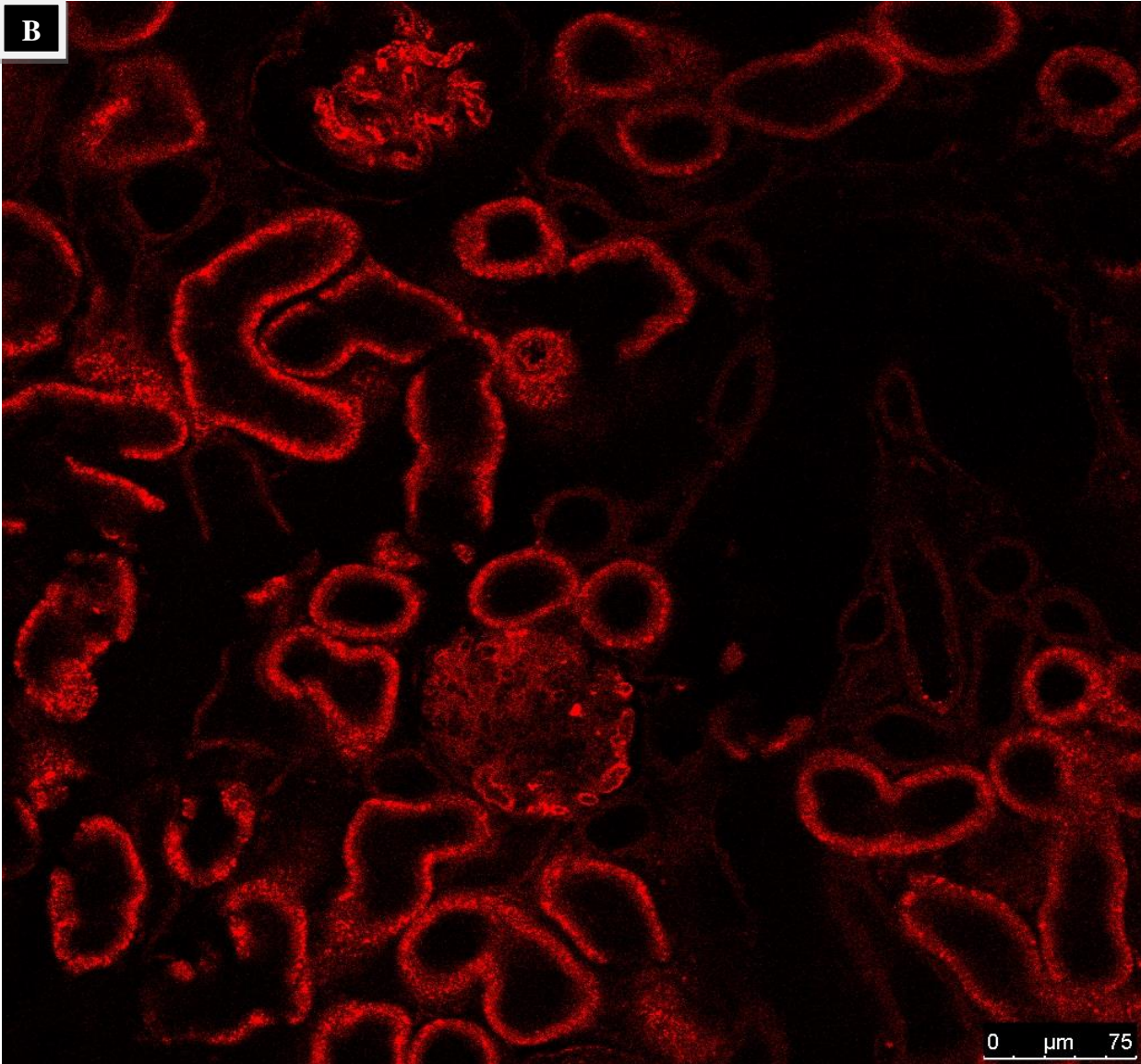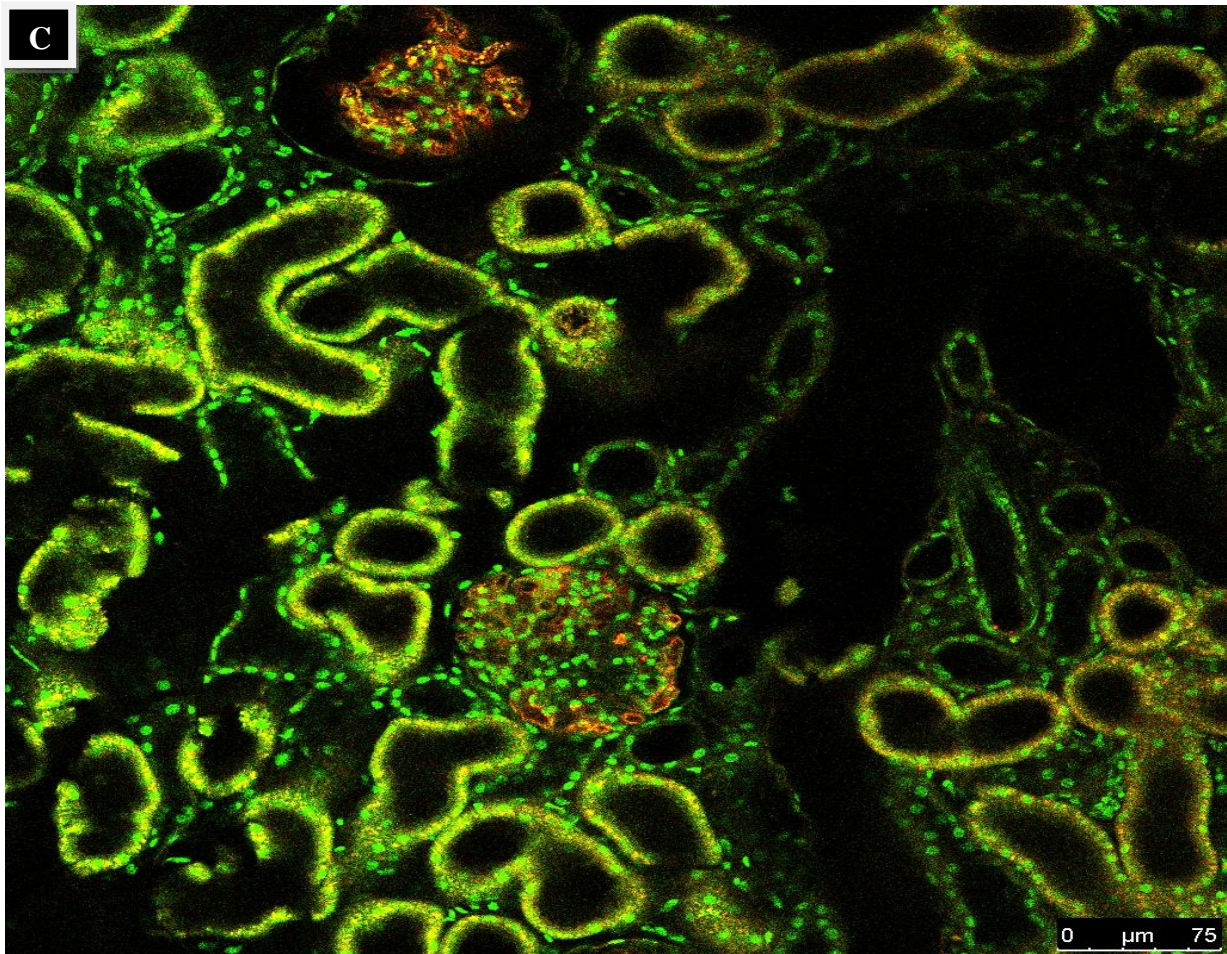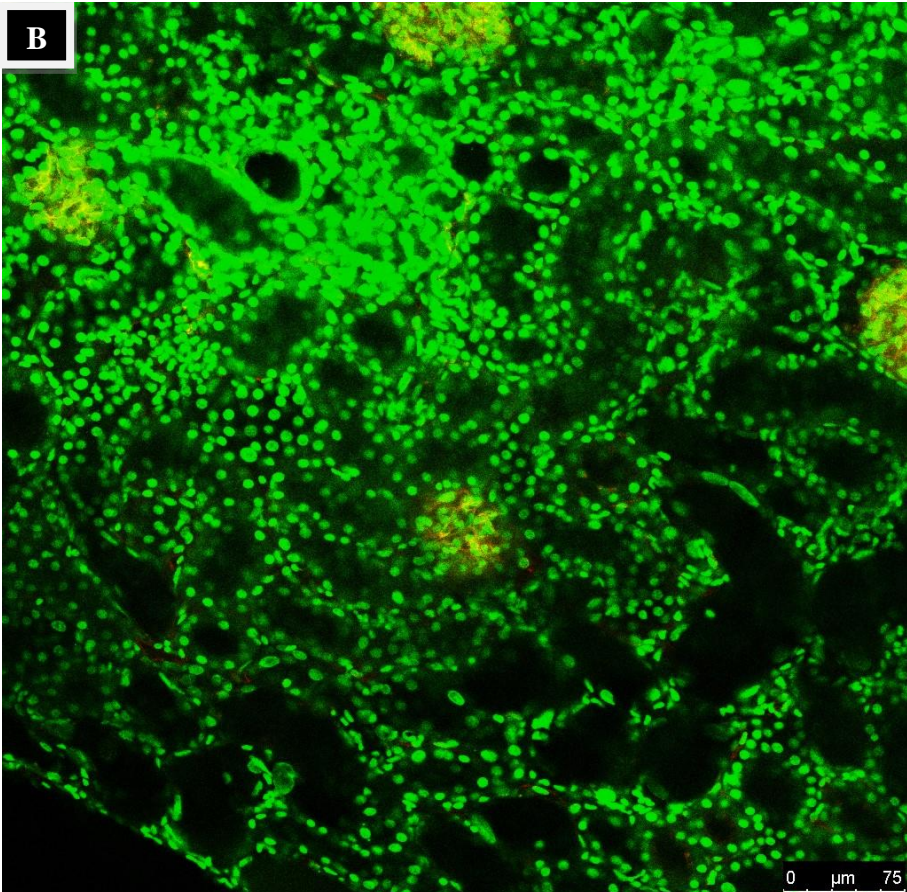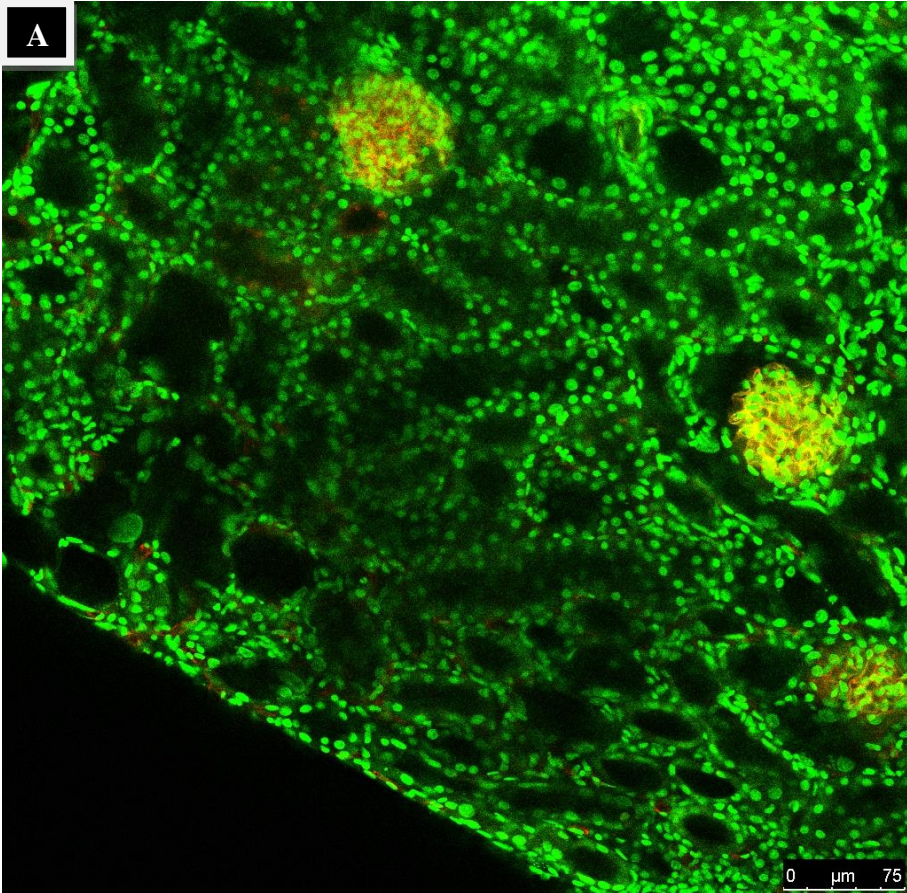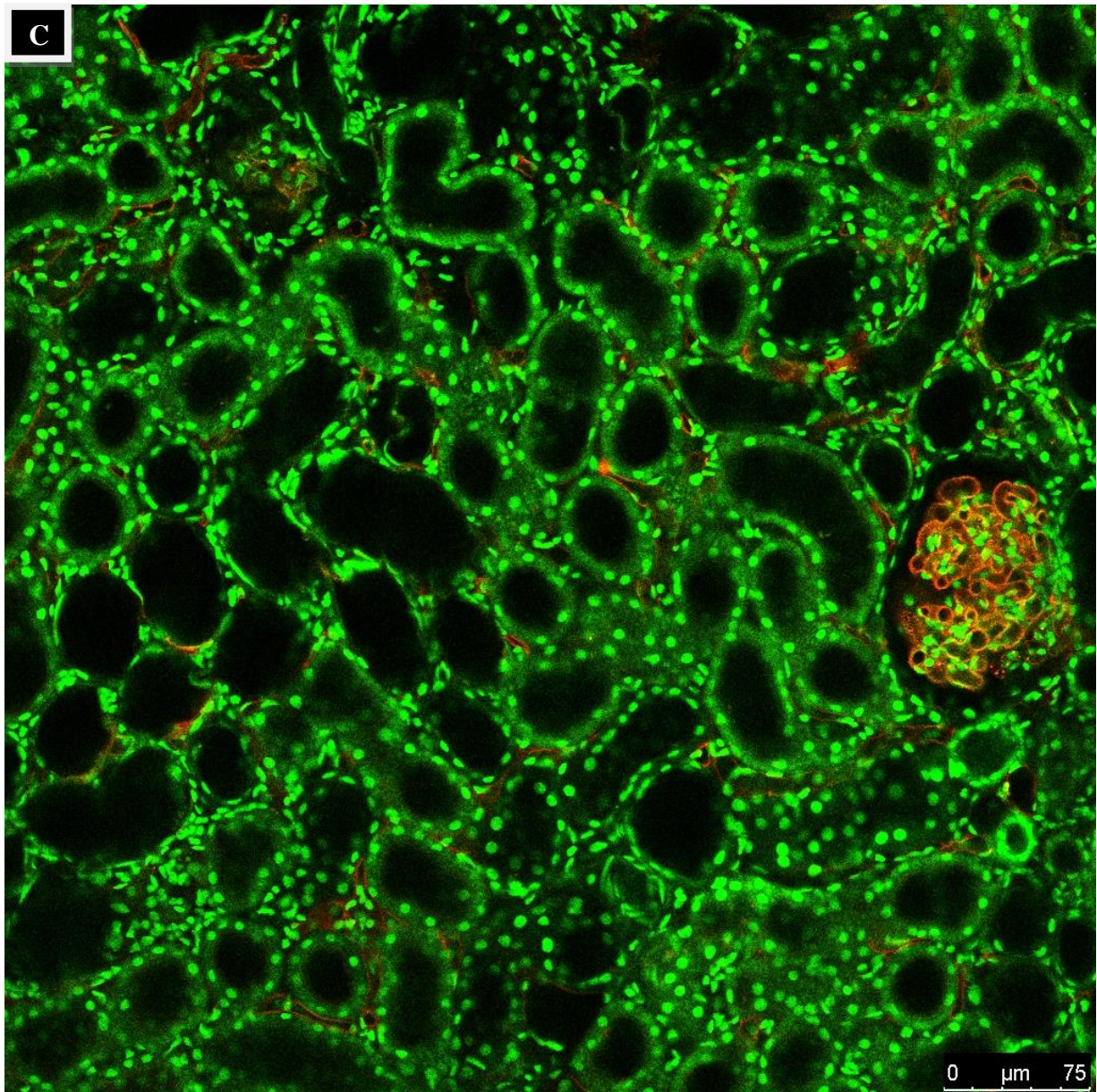
**Figure 4.20**: 2D Kidney section from SD rat, treated with cisplatin injection prior to perfusion and OTC, stained with WGA Alexa Fluo488 conjugated (stock concentration 1mg/ml, diluted 1:1000 in a final volume of 20 ml of solution) and Cy7-PEI, imaged by CM, using a 20x objective in immersion oil. All of the three images are from the same region, where A) shows WGA detection only, with 488 channel; B) Cy7-PEI detection only, with 638 channel and C) overlay image. Scale bars: 75µm

In Figure 4.21 another example of the differential staining, performed with WGA and Cy7-PEI is presented. Again, a very high rate of inflammatory infiltrates (represented by the green dots) is highlighted, while the glomeruli are characterized by orange shades, as result of the combination of both dyes. In C), although no renal tubular dilatation is revealed, the presence of the macrophages is still high. The glomerulus, on the right side, is again in orange shade, as sign of overlay of the two dyes.

**Figure 4.21**: 2D Kidney section from SD rat, treated with cisplatin injection prior to perfusion and OTC, stained with WGA-Alexa Fluo488 conjugated (stock concentration 1mg/ml, diluted 1:1000 in a final volume of 20 ml of solution) and Cy7-PEI, imaged by CM, using a 20x objective in immersion oil. The 488 channel was used for imaging the WGA staining and the 638 channel for the CY7-PEI staining. A), B), C): Images in overlay. Scale bars: 75µm
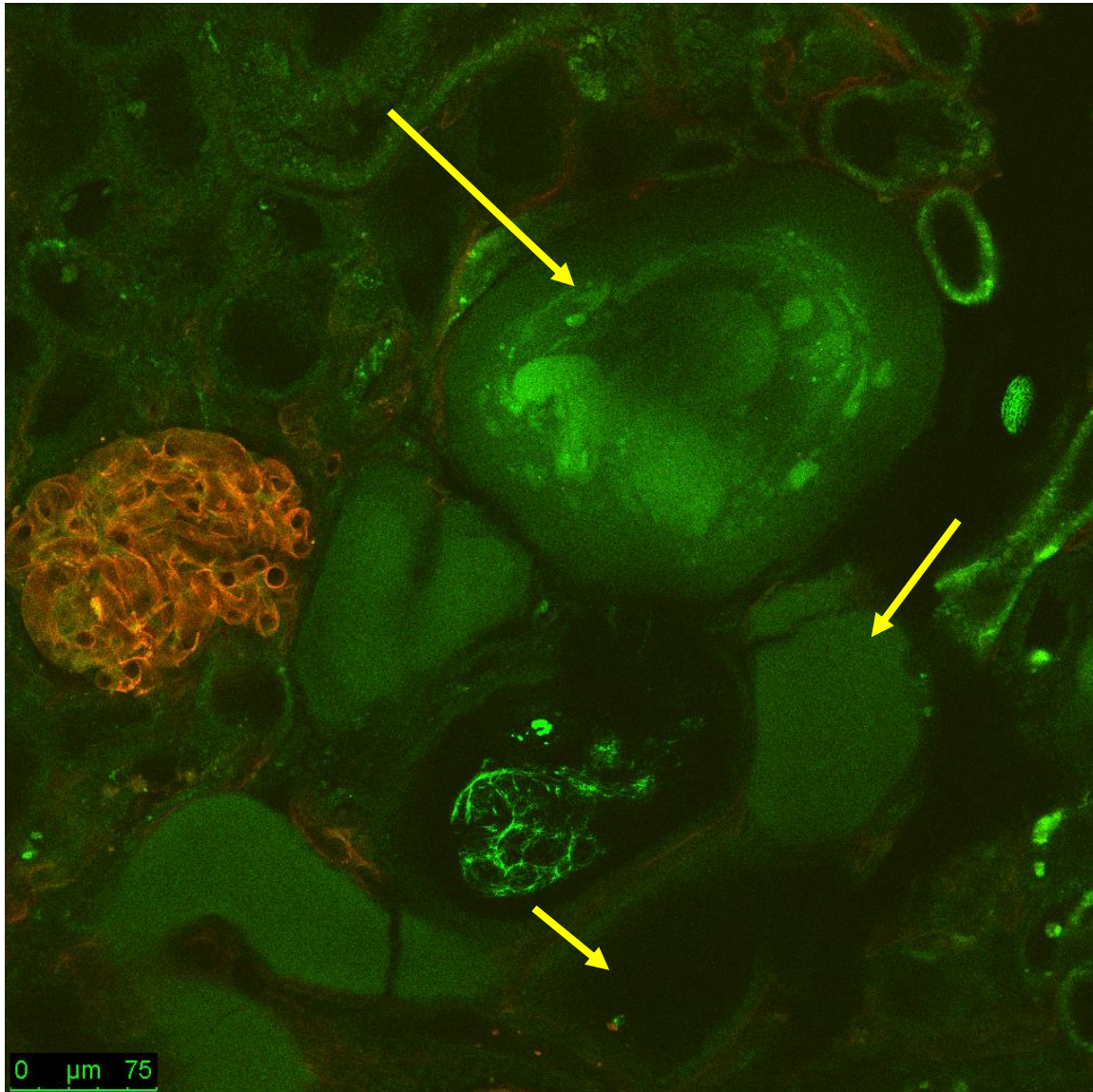
**ADPCK Rat**

As part of the project G19/17, carried out by Daniela Nardozi, under the supervision of Prof. Dr. med. N. Gretz, some 10 months old female ADPCK rat kidneys were provided to be cleared and imaged. As described in Table 4.7, the perfusion procedure was slightly modified, as the timing and the pressure used were adapted for rats, although the injection of the dyes were kept to the same rate as previously described (1ml/min). For these experiments a double staining of WGA and Cy7-PEI was used. The working concentrations of both dyes were kept the same as usual.

| REAGENT | TIME (min) | PRESSURE(mbar) |
|---|---|---|
| NaCl pH 7.4+ hep | 3 | 280 |
| Cy7-PEI | 1 | 230 |
| NaCl pH 7.4+ hep | 1 | 230 |
| WGA | 1 | 230 |
| NaCl pH 7.4+ hep | 1 | 230 |
| 4% PFA | 3 | 230 |

**Table 4.7**: Perfusion protocol used for PCK rats.

Figure 4.22 underlines the presence of some renal cysts (indicated by yellow arrows), different in their appearance. In fact, the different appearance of the cysts depends on their different content, which might be rich in extracellular matrix, proteins or lipids. Based on that, these can appear "full" or "empty". Furthermore, the tubular damage is emphasized by the de-differentiated epithelium. On the left side of the figure, an orange coloured glomerulus is located. This is the result of the overlay of the two dyes, which is more prominent in some structures than in others. In fact, differently from the glomerulus, the cyst content is not the specific Cy7-PEI marker and this is the reason why the renal cysts appear only in green coloured, as the result of the only WGA staining.
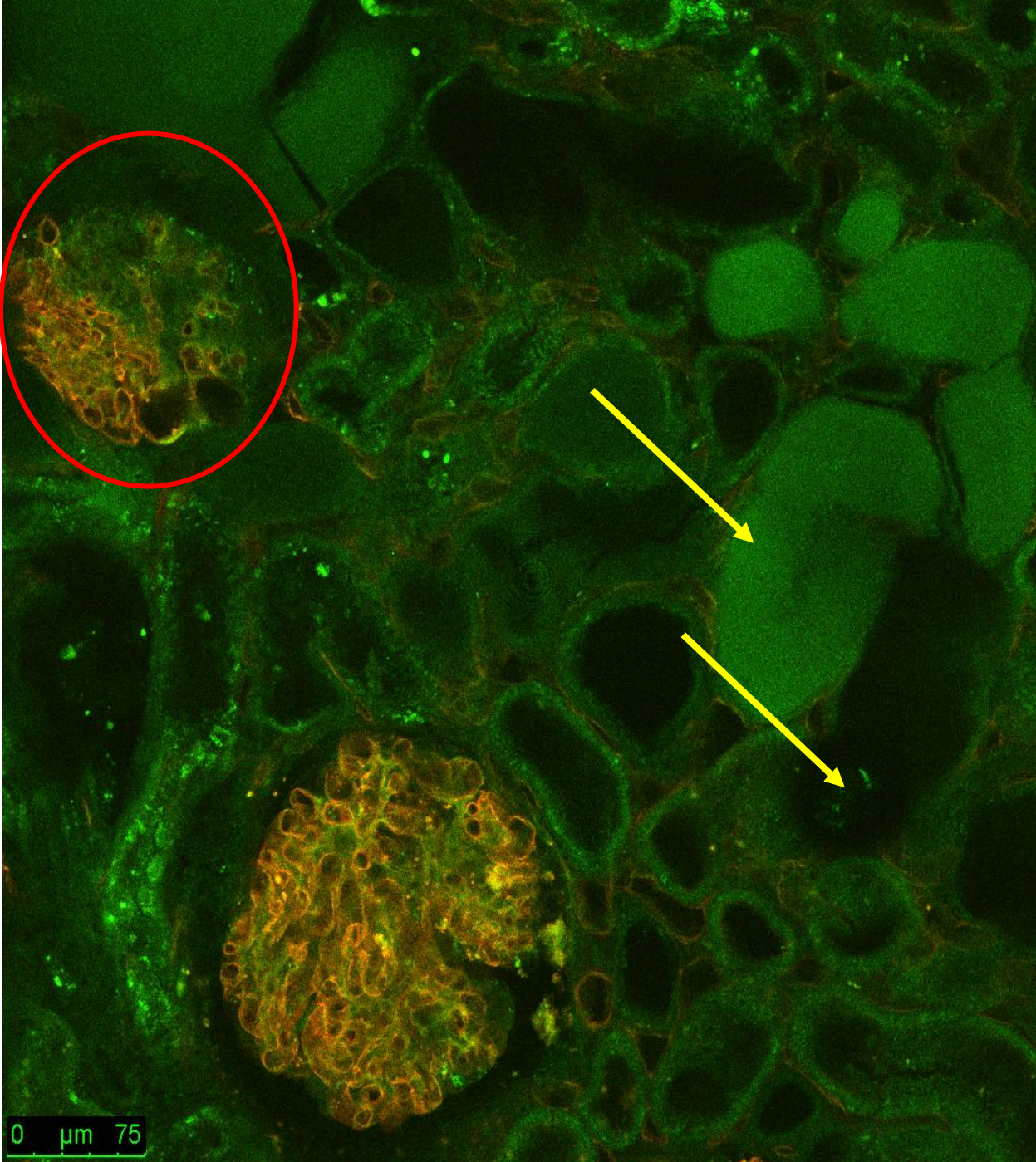
**Figure 4.22**: 2D Kidney section from PCK rat, stained with WGA-Alexa Fluo488 conjugated (stock concentration 1mg/ml, diluted 1:1000 in a final volume of 20 ml of solution) and Cy7-PEI, imaged by CM, using a 20x objective in immersion oil. Channel 488 and 638 used to detect, respectively, the WGA and the CY7-PEI staining. Image in overlay. Scale bar: 75µm

In Figure 4.23 all the distinctive traits of PCK disease are shown. On the bottom of the image a glomerulus with enlarged Bowman's space is visible, as well as cysts, indicated by yellow arrows. The tubular epithelium layer appears de-differentiated and, additionally, there is a clear loss of the normal tubular conformation. Concerning the staining, this image confirms once again the differences between WGA and Cy7-PEI. Only the two glomeruli appear in orange shadows, as sign of overlay of both dyes, whereas, cysts and renal tubuli are completely green, as result of non-specific markers for the Cy7-PEI. Moreover, the

glomerulus depicted in the left upper part of the image (in the red circle) shows only a partial overlay. This is due to a lack of perfusion, which, in turn, might depend on two factors: in fact, this could be a sign either of a glomerular sclerosis or a mesengial expansion.



**Figure 4.23**: 2D Kidney section from PCK rat, imaged by CM, using a 20x objective in immersion oil. Channel 488 and 638 used to detect, respectively, the WGA and the CY7-PEI staining. Image in overlay. Scale bar: 75µm

In Figure 4.24 the 3D image is shown. On the right side of the picture, a big renal cyst (indicated by the pink arrow) is depicted and the renal tubuli, surrounding the two glomeruli in there, are clearly de-differentiated. Once again, the overlay between the two dyes regards only the glomeruli, appearing in the usual orange shadow.
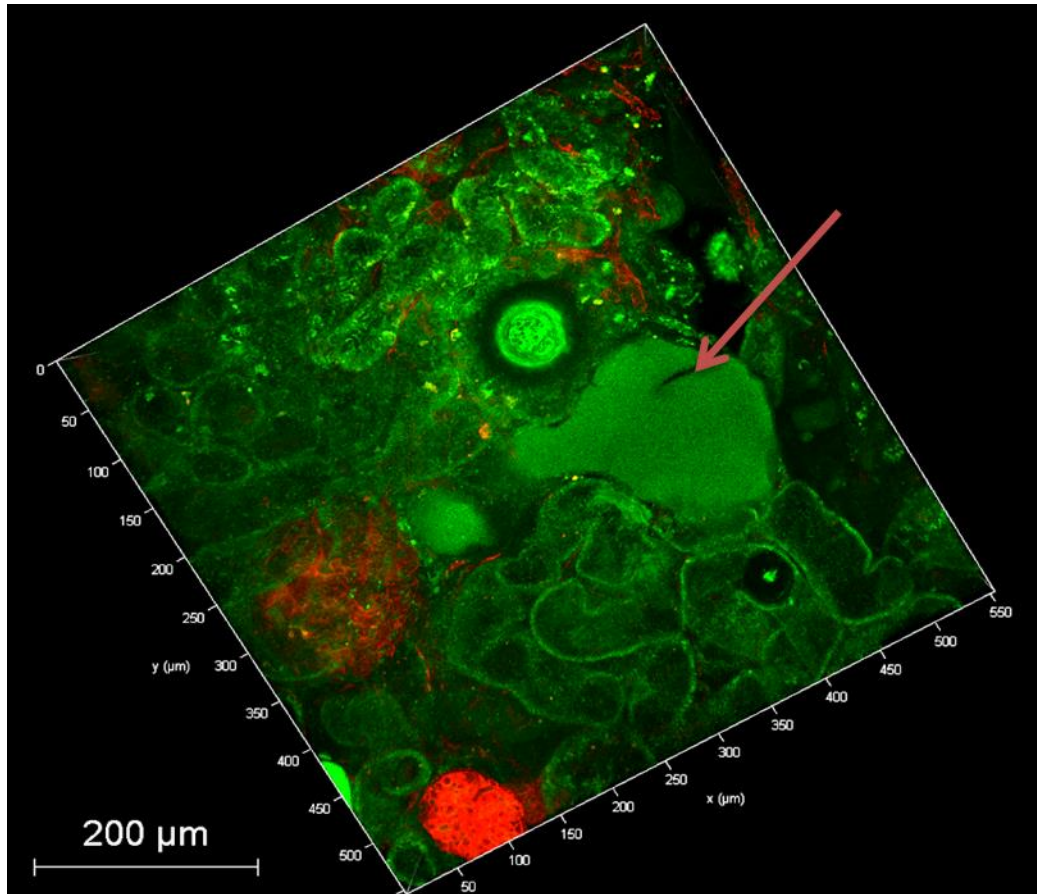


**Figure 4.24**: 3D Kidney section from PCK rat, stained with WGA-Alexa Fluo488 conjugated (stock concentration 1mg/ml, diluted 1:1000 in a final volume of 20 ml of solution) and Cy7-PEI, imaged by CM, using a 20x objective in immersion oil. Channel 488 and 638 used to detect, respectively, the WGA and the Cy7-PEI staining. Image in overlay. Scale bar: 200μm

### 4.5 Different staining: H&E Staining

In order to analyse the fluorescence provided by the H&E staining and combine that with CM microscopy, some mouse, rat and human not cleared kidney slides were stained using the standard procedure which is normally performed for 5μm slides and then imaged by CM. Furthermore, whole mouse organs were perfused with H&E, cleared by the ECi-based OTC procedure and microscopically analysed. This paragraph will show first the images acquired

on the slides and then on the whole organs. Unless stated otherwise, the mouse strain refers to C57BL/6, while the rat strain refers to SD. The human samples came from renal biopsies, provided by the Pathology Department of Universitäts Klinikum of Mannheim.

**MOUSE SLIDES**

Figure 4.25 shows a 3D image of a 5µm mouse slide stained with H&E and analysed through CM. The green colour (488 channel) refers to the eosin, whereas the red colour (552 channel) to haematoxylin. Glomeruli, surrounded by renal tubuli, are immediately evident. Moreover, the red dots within the tubuli are nuclei from the epithelial cells, which are also present in the glomeruli. So, as expected from this staining, both dyes were detected in the right place.
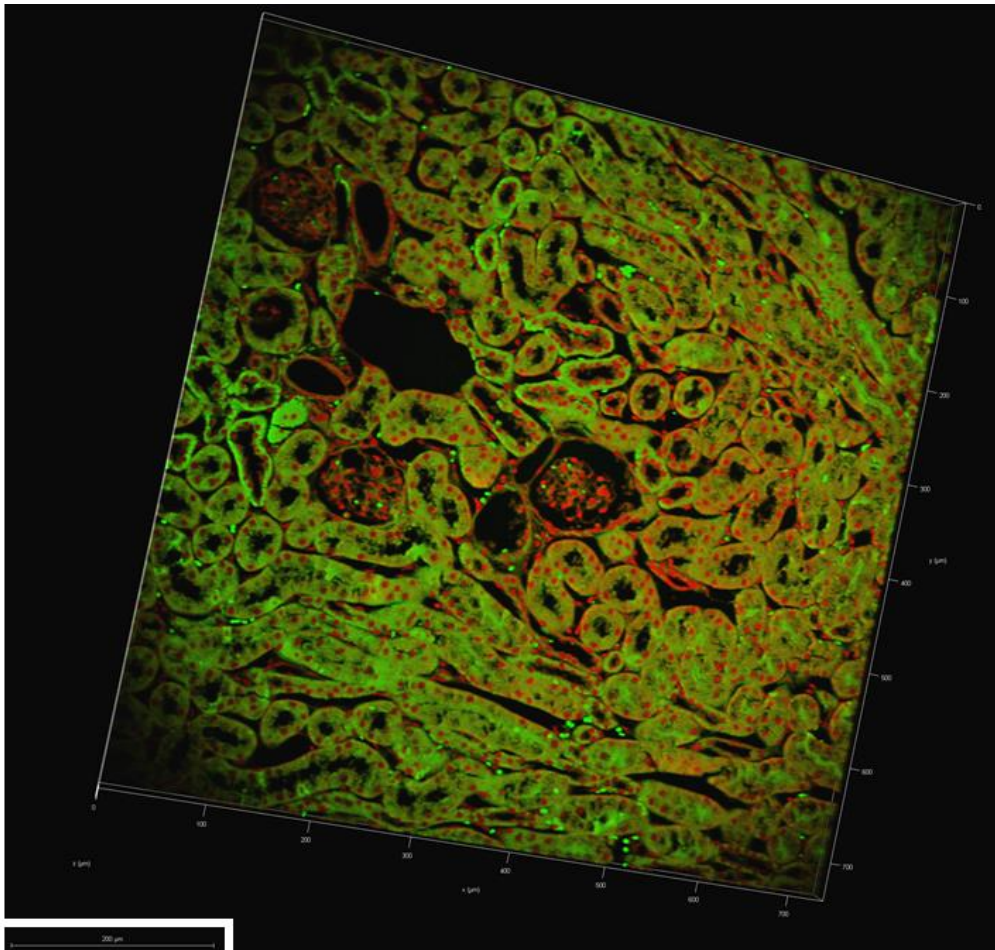


**Figure 4.25**: Mouse slide (5µm), stained with H&E and imaged by CM using a 20x objective in immersion oil 488 plus 552 channels, respectively for eosin and haematoxylin detection. Sample not cleared. 3D Image in overlay. Red colour refers to haematoxylin and green colour to eosin. Scale bar: 200µm.

Figure 4.26 shows a 3µm slide stained by using the H&E protocol from the Pathology Department of the Universität Klinikum of Mannheim. For this imaging, purple colour (552 channel) was used to detect haematoxylin and orange colour (488 channel) eosin. The pinkish gradation is the result of the overlay of both dyes. As expected from the standard visualisation of this staining, the nuclei of epithelial cells are purple coloured, whereas the tubuli appear in orange shadow. However, as a not cleared sample, the detection of blood vessels as well as other inner structures was not possible.
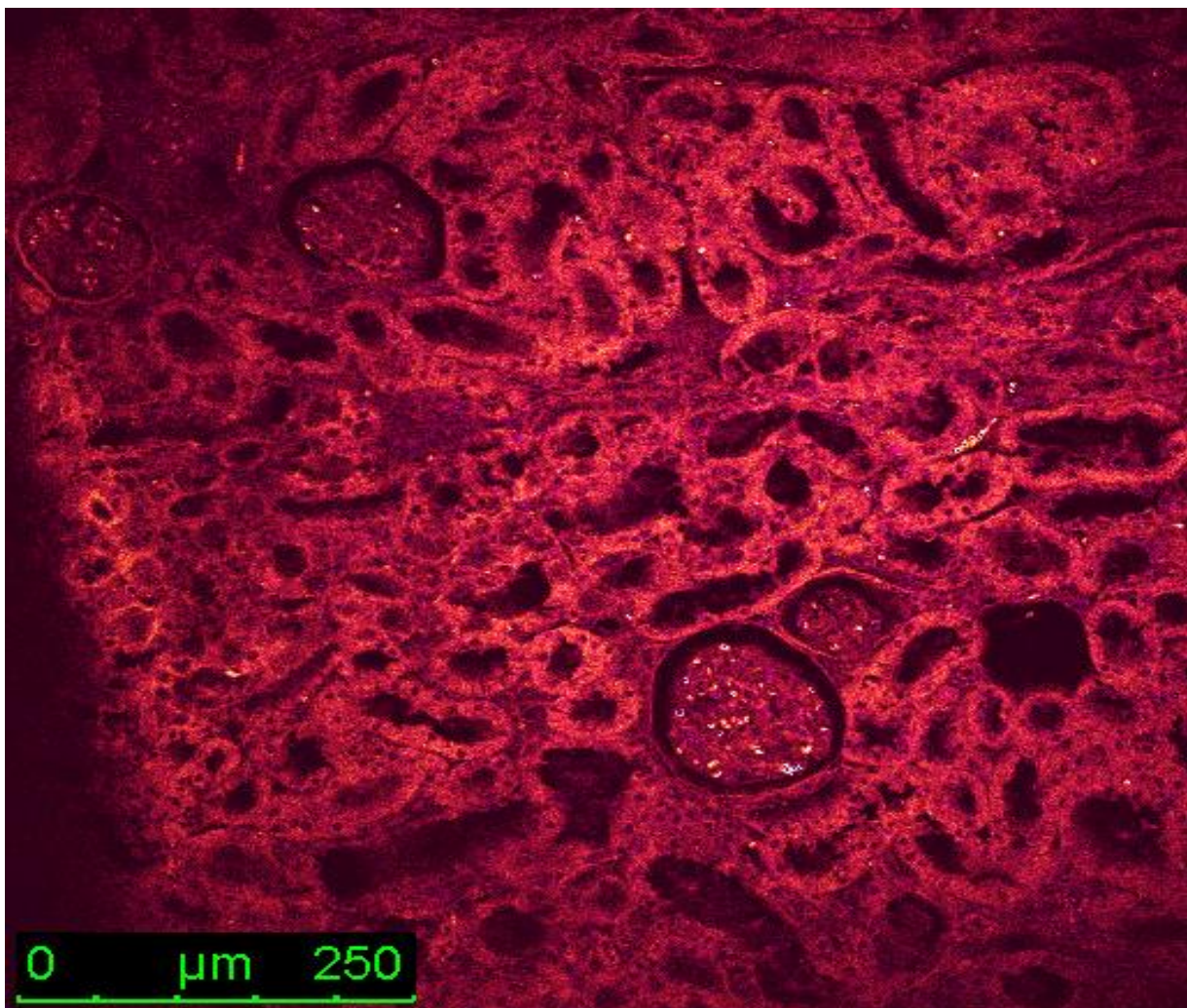


**Figure 4.26**: Slide of a mouse kidney of 3µm in thickness, stained with H&E (Pathology Department protocol – see Material and Methods, Tab.3.2b) and imaged by CM, using a 20x objective in immersion oil and 488 plus 552 channels, respectively for eosin and haematoxylin detection. Sample not cleared. 2D Image in overlay, where purple colour refers to haematoxylin, orange colour to eosin and the pinkish gradation is the result of the overlay of the two channels. Scale bar: 250µm.

**RAT SLIDES**

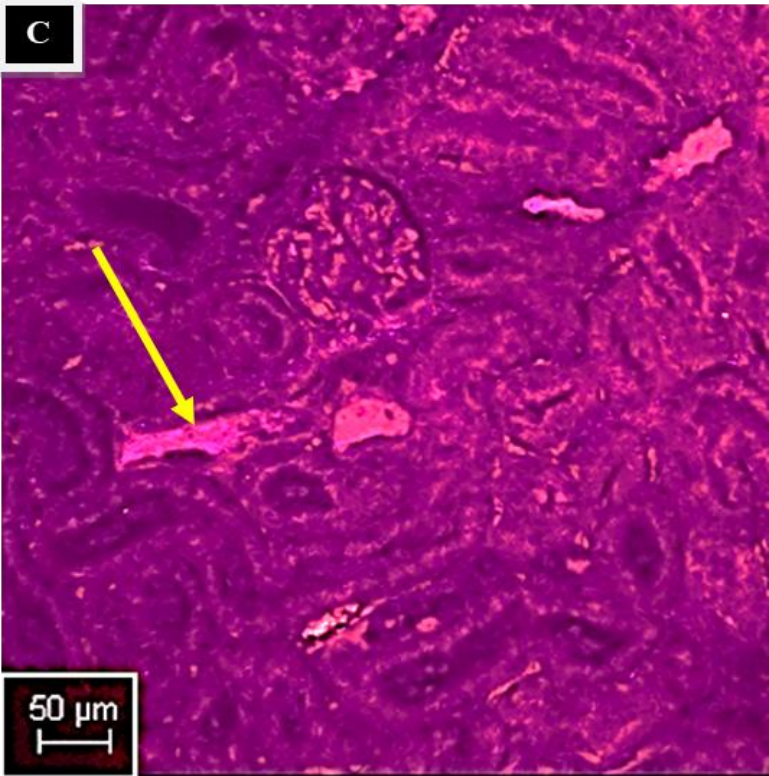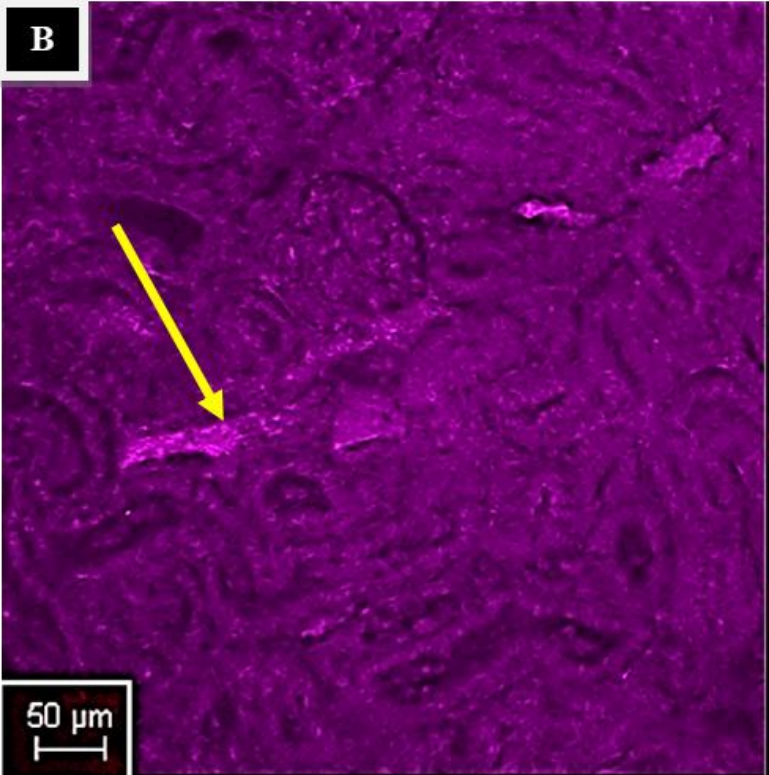Figure 4.27 illustrates the results obtained from the CM imaging of a 5µm rat kidney slide. This is a 2D image. The red colour (488 channel), in A) refers to the eosin the purple colour (552 channel) in B) to the haematoxylin and the magenta shadow in C) is the overlay of the A) and B). Especially in A) and C) a whole glomerulus surrounded by tubules is evident. Moreover, Figure 4.27 A) displays the surface of the tissue structures, as expected from a standard visualisation in a normal microscope and the cellular nuclei are displayed as dark dots, as result of the negative contrast. These are better revealed in B), where the only haematoxylin detection is shown. Also the overlay underlines the presence of cellular nuclei within the glomerulus, in particular where the haematoxylin intensity is stronger. In addition it is important to underline the lack of clearing, which is the reason why only superficial structures were detected. Despite that, a renal blood vessel is clearly recognizable, as indicated by the yellow arrows.
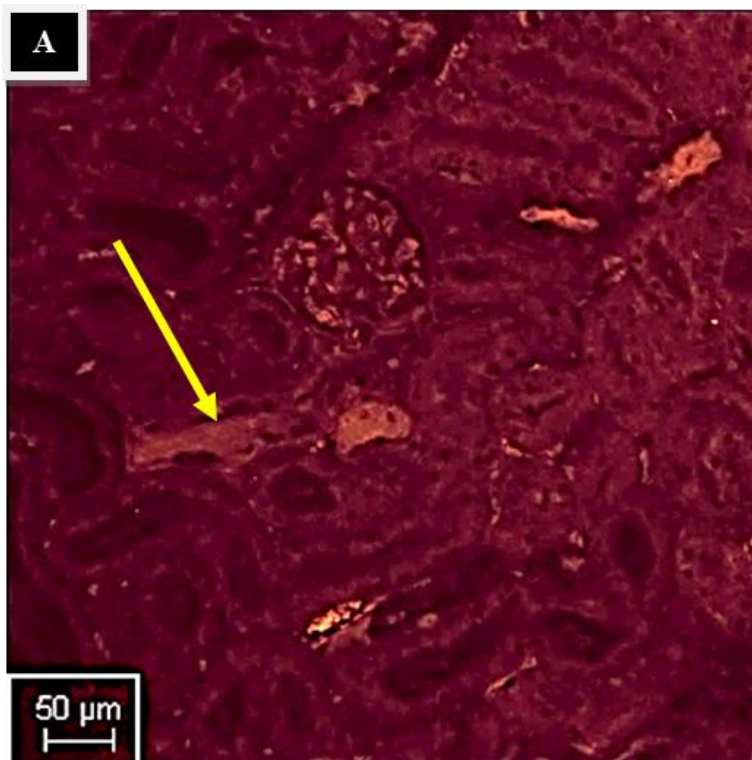


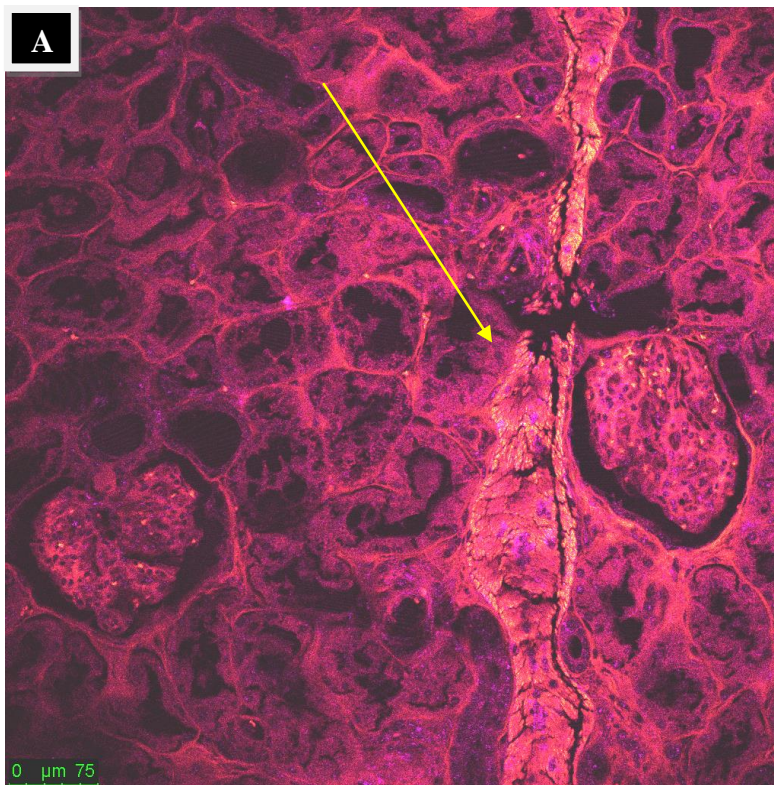**Figure 4.27**: 2D Slide of a rat kidney of 5µm in thickness, stained with H&E and imaged by CM, using a 20x objective in immersion oil and 488 plus 552 channels, respectively for eosin and haematoxylin detection. Sample not cleared. A) Image acquired by 488 channel only, for eosin detection. B) Image acquired by 552 channel only, for haematoxylin detection. C) Image in overlay. Scale bars: 50µm

**HUMAN SAMPLES**

This section will examine the results obtained from the imaging of human kidney slides with CM. Figure 4.28 A) and B) show human glomeruli in detail. A closer look underlines cellular nuclei, here represented as dark dots, due to the negative contrast coming from the overlay. A wider Bowman's space is well recognisable. The renal tubuli around the glomeruli are easily detectable and the overlay provides a better visualisation of all the structures. Being a not cleared tissue, no inner structure is displayed. In addition, Figure 4.28 A) highlights also the presence of some fibrotic tissue (indicated by the yellow arrow).

**Figure 4.28**: 2D Kidney section (50µm) from human renal biopsy, stained with H&E and imaged by CM, using a 20x objective in immersion oil and 488 plus 552 channels, respectively for eosin and haematoxylin detection. Sample not cleared. Both A) and B) are images in overlay, where the purple colour refers to haematoxylin and the orange one to eosin. The overlay generates a magenta colour. Scale bars: 75µm
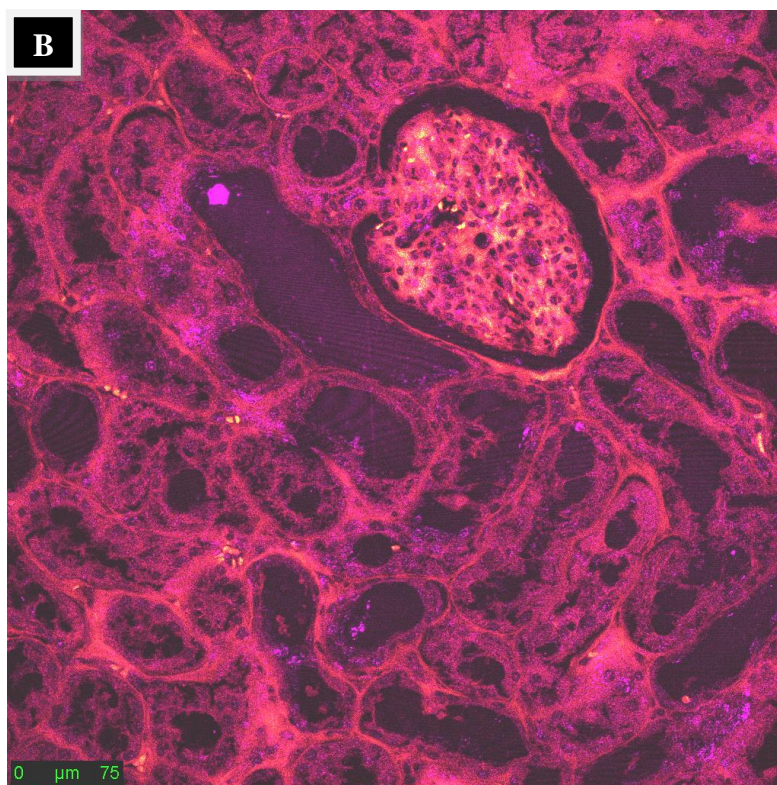
The following images (Fig.4.29, Fig.4.30) will be focused on WT C57BLK/6 mouse samples, perfused with a combination of H&E and Cy7-PEI (protocol description in Tab. 4.8), then cleared by the ECi-based OTC and, afterwards, imaged by CM. The Cy7-PEI working concentration was kept to 3mg/ml and all dyes were injected in the usual ratio of 1ml/min.

| REAGENT | TIME (min) | PRESSURE (mbar) |
| --- | --- | --- |
| NaCl pH 7.4+ hep | 6 | 180 |
| Cy7-PEI | 10 | 180 |
| NaCl pH 7.4+ hep | 1 | 180 |
| Hemtoxylin | 5 | 180 |
| NaCl pH 7.4+ hep | 1 | 180 |
| Eosin | 5 | 180 |
| NaCl pH 7.4+ hep | 1 | 180 |
| 4% PFA | 6 | 180 |
| **Table 4.8**: Perfusion protocol used for the triple staining on C57BL/6 mouse | | |

After the perfusion, kidneys and lungs were collected, cleared and microscopically analysed. Two purposes aimed this experiment:

a) Firstly, to figure out whether other dyes, in addition to Cy7-PEI, would have survived the ECi OTC;

b) Secondly, to evaluate whether the H&E staining could have provided a differential staining also on 3D objects;

c) Lastly, to understand whether the H&E combined to Cy7-PEI could have given additional information for the 3D imaging.

The following images will show the results concerning the aforementioned protocol.

In Figure 4.29, a mouse kidney stained with the aforementioned perfusion protocol is shown. The orange colour (488 channel) in A) refers to eosin, purple colour (552 channel) in B) to haematoxylin, red colour (638 channel) in C) to Cy7-PEI and the magenta shade in D) is the result of the overlay of the all channels. The analysis through CM pointed out that all dyes survived the OTC procedure. Despite that, a differential staining was only partially possible. In fact, due to the perfusion which allows the staining of the whole animal body, although all dyes contributed to stain all tissue structures, the specific markers of each single dye are clearly viewable from the images. In fact, the eosin channel in A) distinctly shows renal tubuli, which are the proper eosin marker; in addition to that, the haematoxylin channel in B) depicts also some cellular nuclei and the Cy7-PEI channel in C) contributes to the glomeruli staining to a larger extent compared to the previous ones. In D), where the overlay is reproduced, a whole set of these structures is represented. It is important to underline the overlapping phenomenon in the same region of the spectrum between all dyes. For instance, haematoxylin and Cy7-PEI share part of that, creating, therefore, a sort of masking effect. This could be a reason why a partial differential staining occurs.
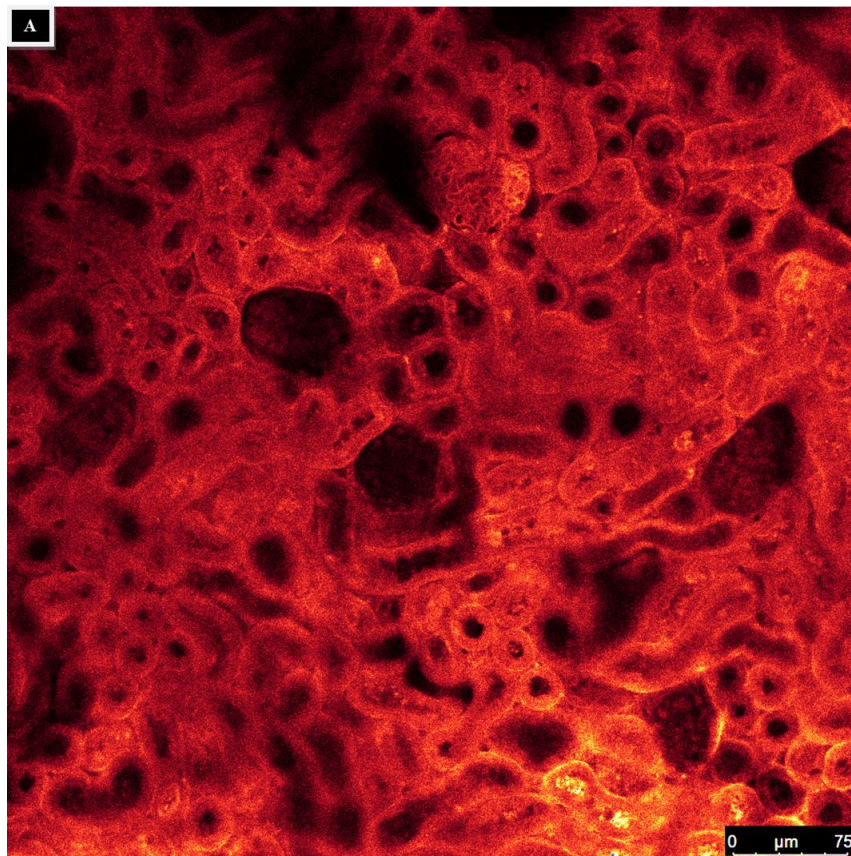
**Figure 4.29**: 2D mouse kidney section, perfused by Cy7-PEI and H&E. Image acquired by CM, using a 20x objective in immersion oil and 488, 552 and 638 channels, respectively for eosin (A), haematoxylin (B) and Cy7-PEI (C) detection. Scale bars: 75µm. D) Image in overlay. Scale bar: 50µm
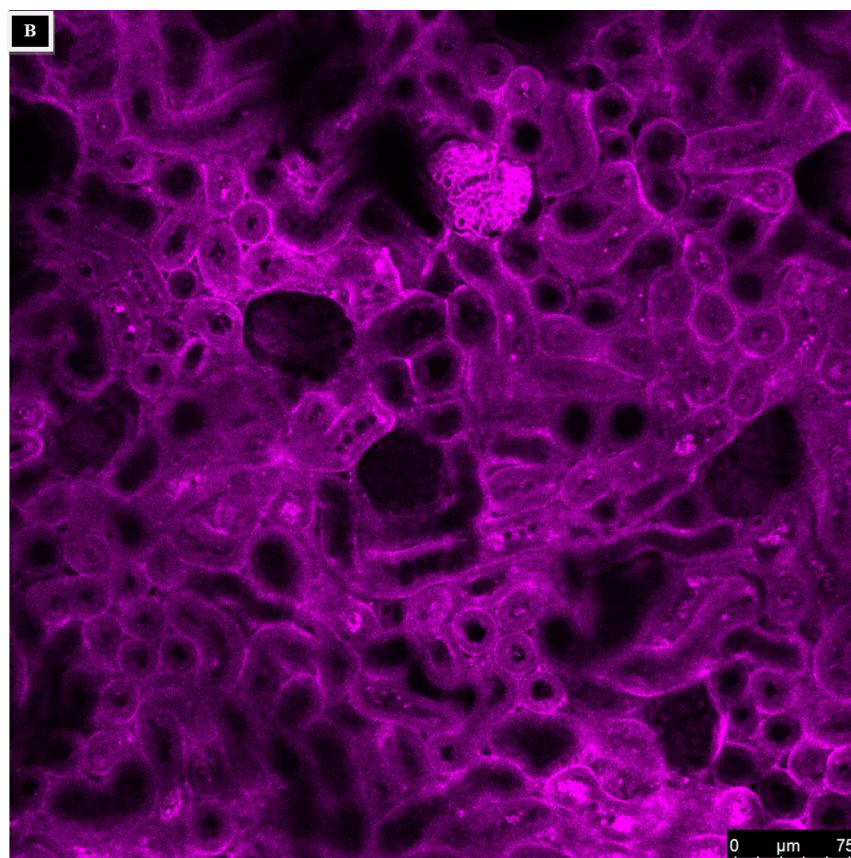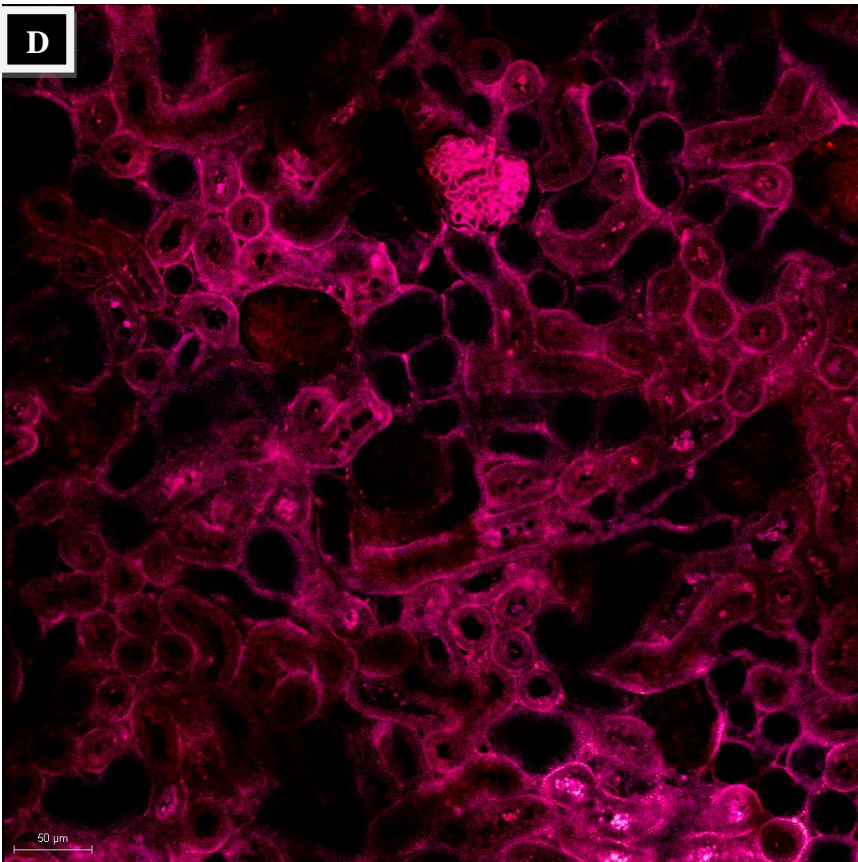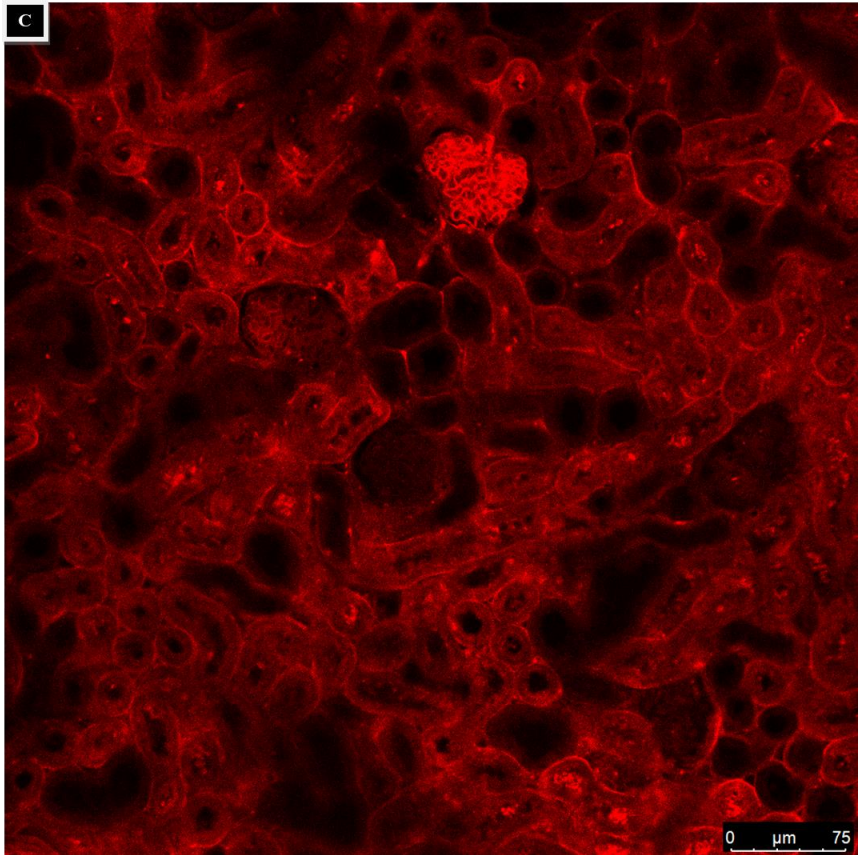
Figure 4.30 illustrates a mouse lung. As previously described, the orange colour (488 channel) in A) refers to eosin, purple colour (552 channel) in B) to haematoxylin, red colour (638 channel) in C) to Cy7-PEI and the magenta shade in D) is the result of the overlay of the all channels. Even in this case all dyes survived to the ECi-based OTC. Although, as previously described, only a partial staining was possible the main pulmonary structures, as alveoli and the pulmonary artery are detectable.



**Figure 4.30**: 2D mouse lung section, perfused by Cy7-PEI and H&E. Image acquired by CM, using a 20x objective in immersion oil and 488, 552 and 638 channels, respectively for eosin (A), haematoxylin (B) and Cy7-PEI (C) detection. D) Image in overlay. Scale bars: 100μm
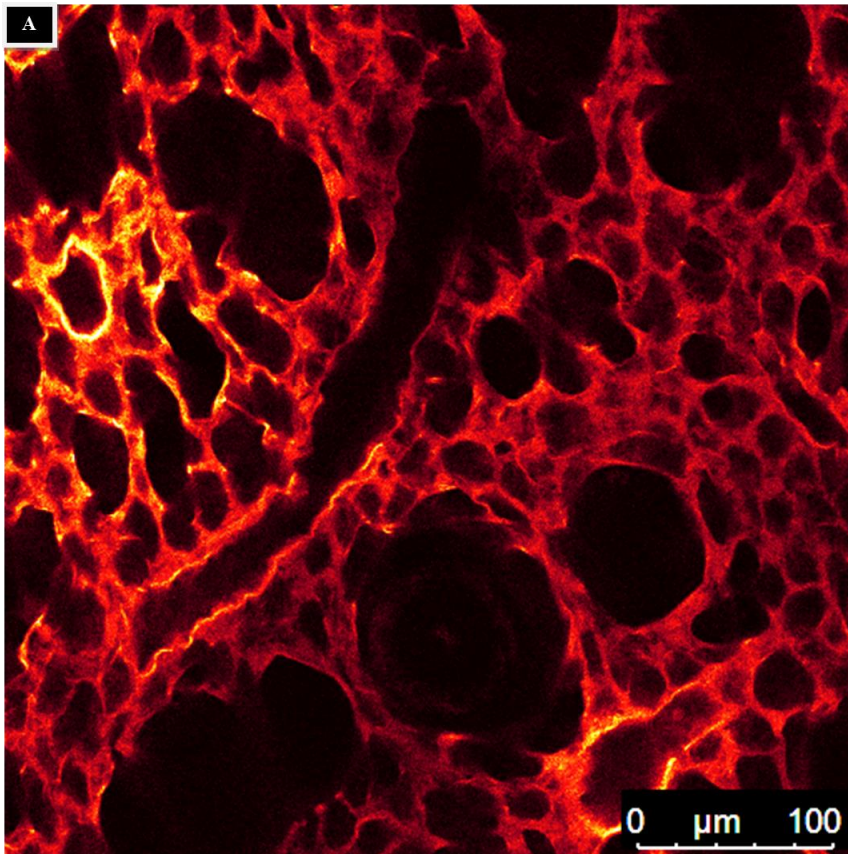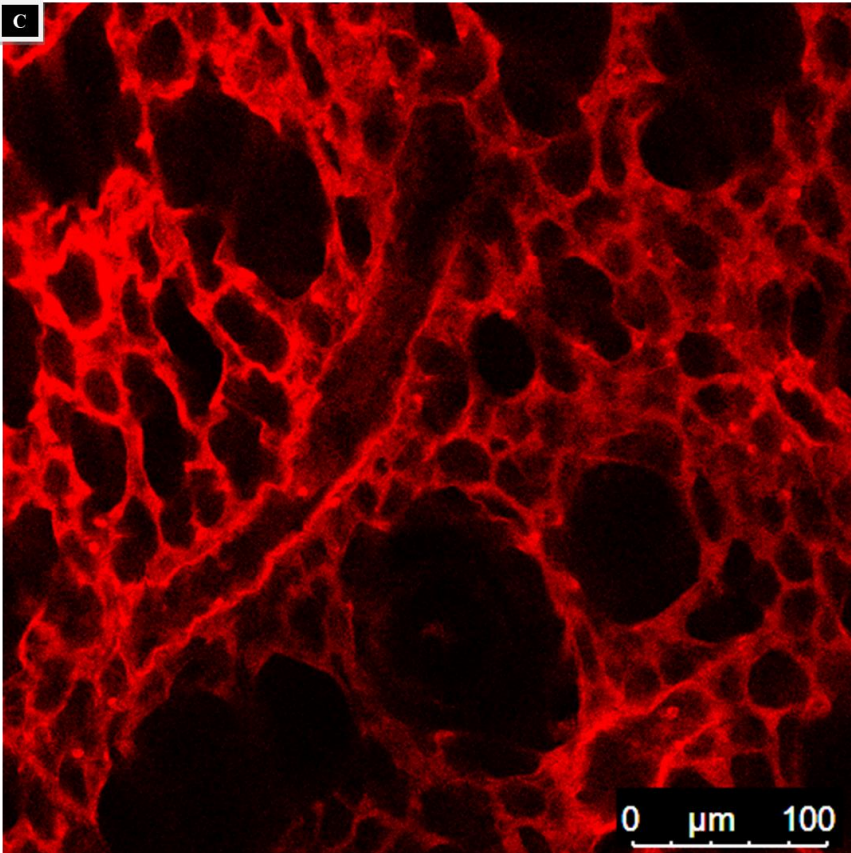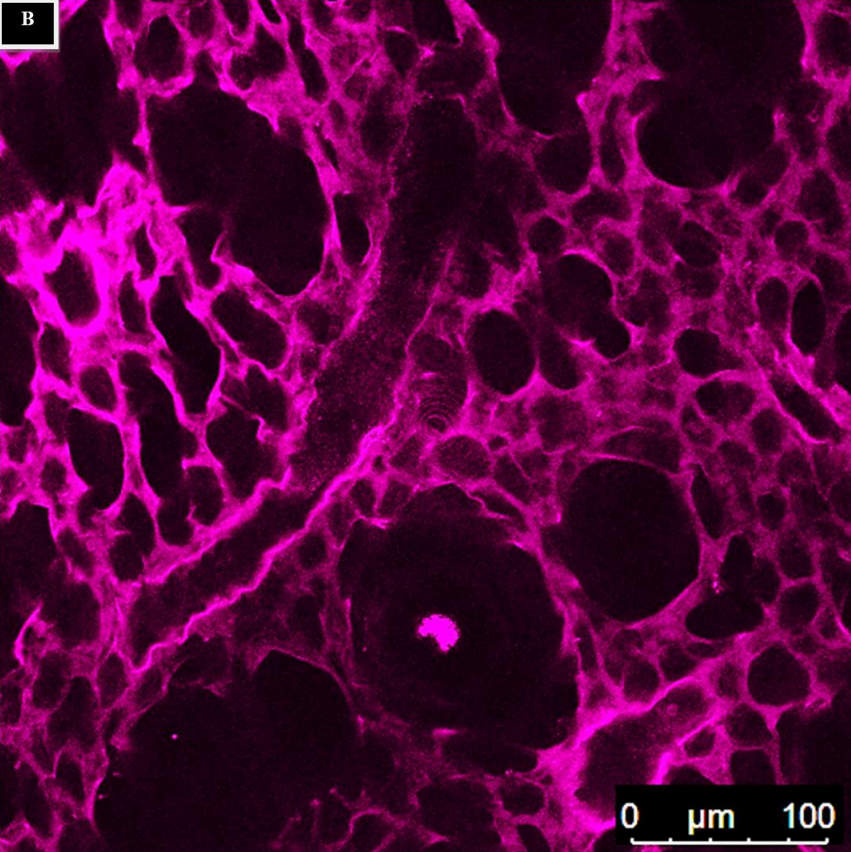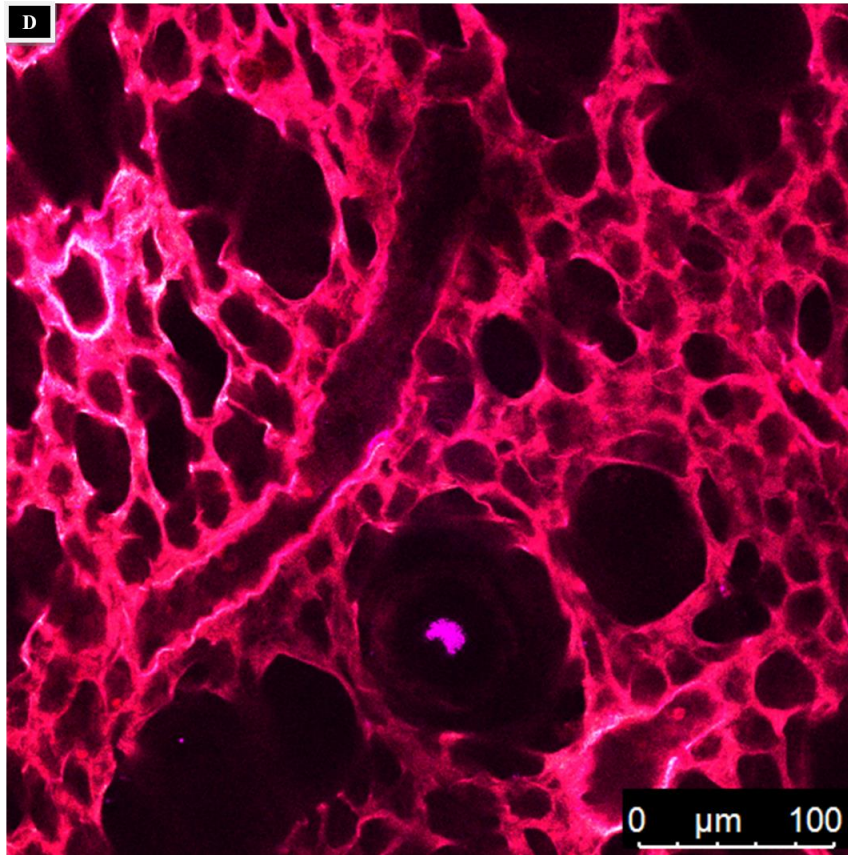
## 4.6 Shrinkage Studies

The following paragraph will describe the results obtained by comparing the optimised (Opt) and the original protocol (Org[52]). After mouse perfusion, kidneys, heart, liver, lung and spleen were collected and the following parameters were analysed before and after the two different procedures (for all the details refer to Material and Methods): weight, surface area, volume and lipid content, in order to asses which of the two ECi-based OTC protocols could generate the more shrinkage. The following graphs (Fig. 4.31, 4.32, 4.33, 4.34) illustrate the results obtained from these studies.

Figure 4.31 relates to the weight results. Except for lungs, all the other organs exhibit a decrease in weight after both protocols: heart: -0.065g (Opt), -0.132g (Org); kidney: -0.059g (Opt), -0.11g (Org); liver: -0.34g (Opt), -0.47g (Org); spleen: -0.042g (Opt), - 0.053g (Org). On the other hand, lung seems to gain weight after both the procedures: +0.065g (Opt), +0.015g (Org).
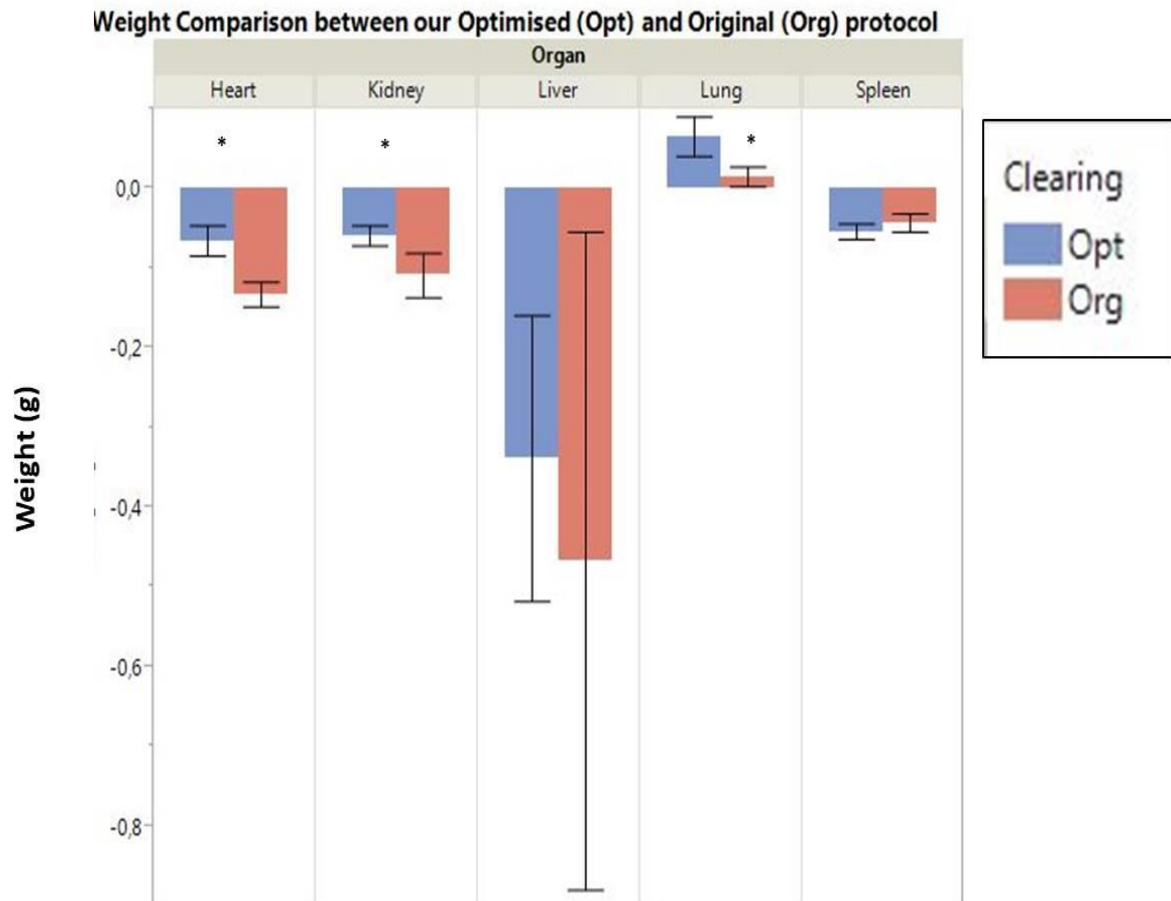
**Figure 4.31**: Shrinkage analysis of different organs based on weight (manual).

Bar plot show the weight comparison between our optimized (blue bar) and the original protocol (red bar). The values are the results from differences obtained by calculating the weight before and after the OTC procedure, for both protocols and for all the organs. The weight values are expressed in g. Asterisks indicate significance ($p < 0.05$) in a paired t test between the two protocols, error bars denote SD. The sample size is n = 5.

Figure 4.32 shows the surface area comparisons between Opt and Org protocol. As described in the following graph, for the surface area a decrease was noticed after both the procedures, for all organs except for lung after Org. The changes are the following: heart: -26.83% (Opt), -55.93% (Org); kidney: -26.83% (Opt), -55.93% (Org); liver: -36.12% (Opt), -46.91% (Org); lung: -56.79% (Opt), +49.83 (Org), spleen: -13.13% (Opt), -70.19% (Org).

**Figure 4.32**: Shrinkage analysis of different organs based on surface area (manual).

Bar plot show the surface area comparison between our optimized (blue bar) and the original protocol (red bar). The values are the results from differences obtained by calculating the surface area before and after the OTC procedure, for both the protocol and for all the organs. Afterwards, the values were normalized to fixed percentage (100%) for organs before clearing. The surface area values are expressed in percentages. Asterisks indicate significance ($p < 0.05$) in a paired t test between the two protocols, error bars denote SD. The sample size is n = 3.

Figure 4.33 regards the volume values, obtained from the two different ECi-based OTCs. Very important differences were observed. In fact, for heart and kidney, liver and lung a very high decrease in the volume is present after the original procedure when compared to the optimised one: heart: -26.16% (Opt), -86.80% (Org); kidney: -59.60% (Opt), -85.06% (Org); liver: -35.52% (Opt), -89.09% (Org); lung: -82.22% (Opt), -44.82% (Org). The opposite situation was found in spleen, which seems to decrease its volume more in the optimised protocol than in the original: spleen: -70.69% (Opt), -55.35% (Org).
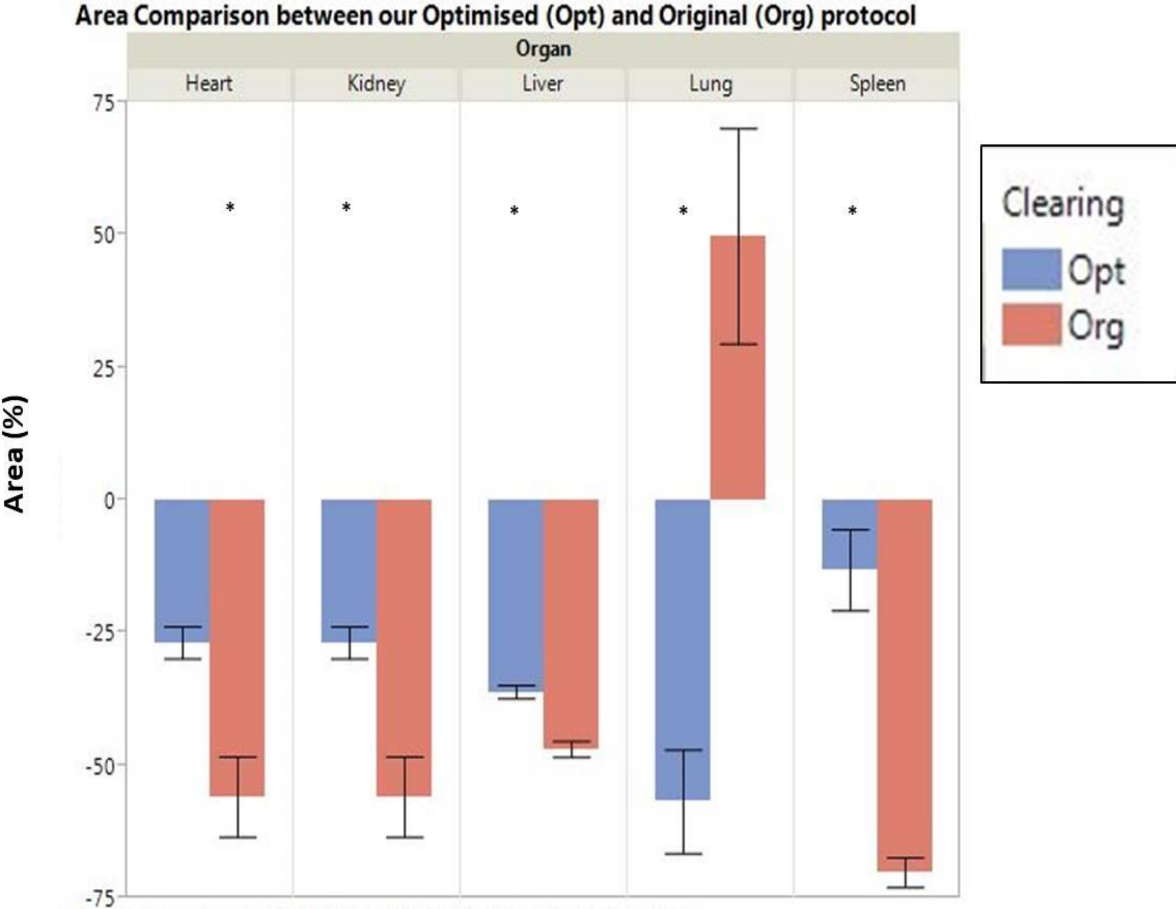
**Figure 4.33**: Shrinkage analysis of different organs based on volume (manual).
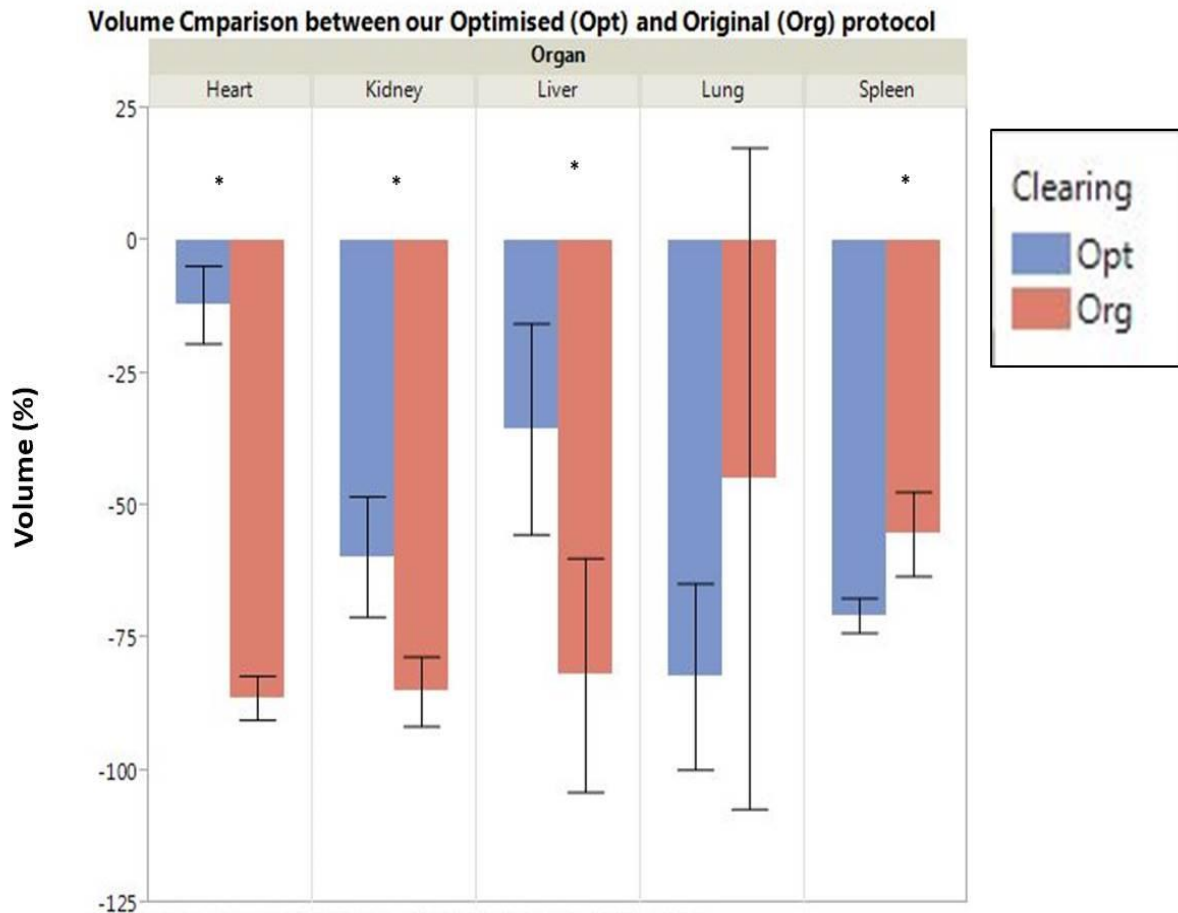
Bar plot show the volume comparison between our optimized (blue bar) and the original protocol (red bar). The values are the results from differences obtained by calculating the volume before and after the OTC procedure, for both the protocol and for all the organs. Afterwards, the values were normalized to fixed percentage (100%) for organs before clearing. The volume values are expressed in percentages. Asterisks indicate significance ($p < 0.05$) in a paired t test between the two protocols, error bars denote SD. The sample size is n = 5.

Figure 4.34 presents the results concerning the lipid content. Both OTC protocols contribute to the lipid extraction in the same way. In fact, none of the t-tests performed gave a significant result ($p > 0.05$). A reduction of the lipid contents occurred almost equally in both procedures: heart: -87.29% (Opt), - 91.23% (Org); kidney: -92.09% (Opt), -92.55% (Org); liver: -94.42% (Opt), -88.88% (Org); spleen: -86.96% (Opt), -86.65% (Org); lung: -94.99% (Opt), - 85.63% (Org).
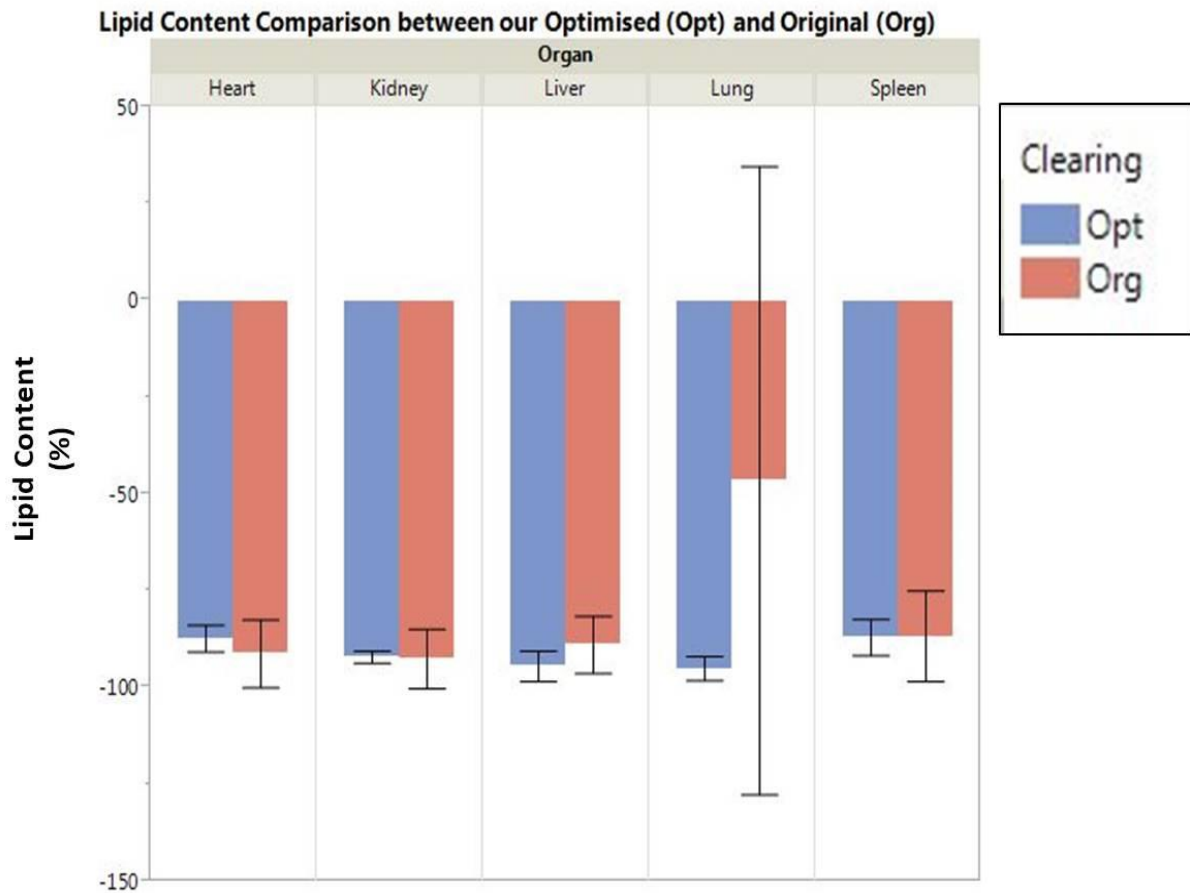
**Figure 4.34**: Shrinkage analysis of different organs based on lipid content (fluorescent assay). Bar plot show the lipid content comparison between our optimized (blue bar) and the original protocol (red bar). The values are the results from differences obtained by calculating the lipid content before and after the OTC procedure, for both the protocol and for all the organs. Afterwards, the values were normalized to fixed percentage (100%) for organs before clearing. The lipid content values are expressed in percentages. Error bars denote SD. The sample size is n = 5.

## 4.7 Dye Stability

In order to evaluate and prove the stability of the fluorescent dyes, after a long time (years), in ECi, three different imaging were performed on the same mouse kidney sample with an interval of 2 and 3 years, as shown in Figures 4.35, 4.36, 4.37. The staining was Cy7-PEI-opt 4F in 3mg/ml as concentration. Before going on with the imaging, the sample was stored for 48 hours in 88% glycerol for the RI correction. Figure 4.35 A) displays a 2D picture, revealing a differential staining, as result of a combination of the dye itself (red colour) and the autofluorescence (green colour). Thanks to that, in fact, it was possible to detect all the

structures, even the ones which are not detectable by Cy7-PEI-opt 4F. In green, renal tubuli are visible, whereas glomeruli are in a colour range between red and yellow, as result of an overlay of the two channels. The 3D image in depth coding in B) proves the detection of structures in different points of depth.
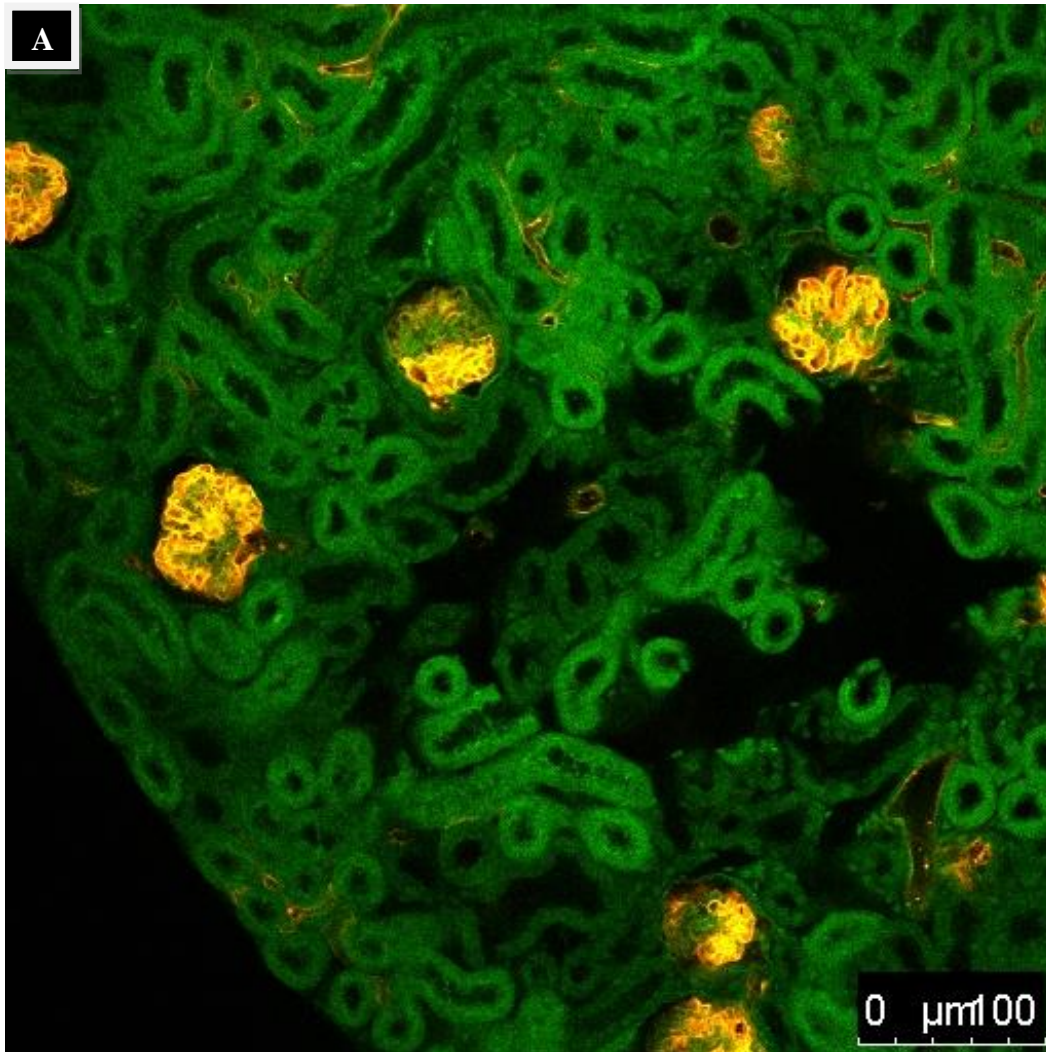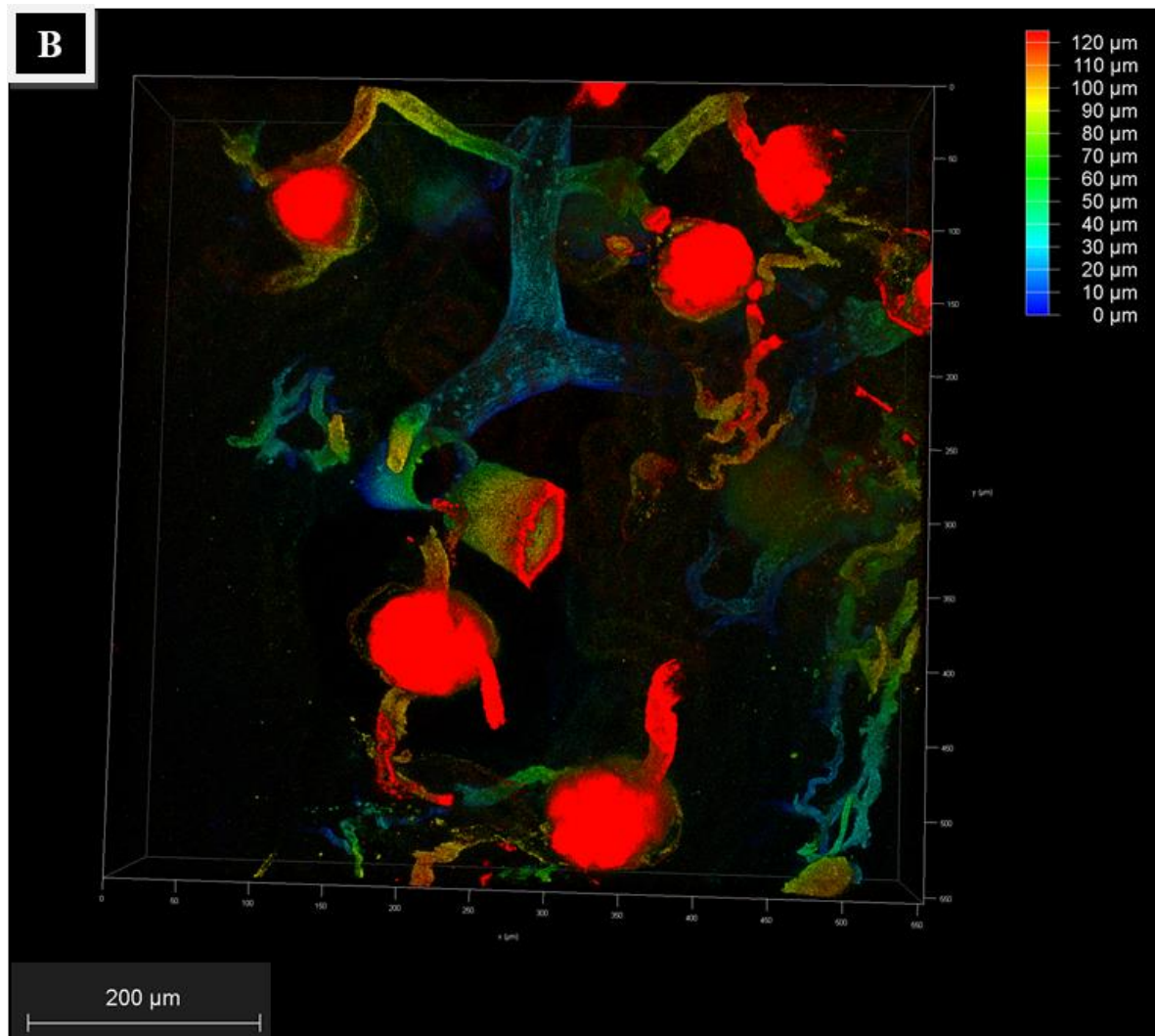
**Figure 4.35**: Section of mouse kidney imaged by CM, stained by Cy7-PEI-opt in 3mg/ml as concentration, using a 20x objective in 88% glycerol and 488 plus 638 channel to respectively detect autofluorescence and Cy7-PEI-opt 4F. A) 2D section. Scale bar: 100µm. B) 3D section in depth coding. The depth bar on the right side of the image indicates the depth reached during the imaging: it goes from the surface (0-40µm, in blue-light blue), the middle area (40-100µm, in green-yellow) up to the deepest parts (100-120µm, in orange-red).Scale bar: 200 µm

Figure 4.36 regards the same mouse kidney from Figure 4.35, which was imaged after 2 years. Except for the detection of the autofluorescence and the use of the Stage Overview, which gave a big amelioration, other experimental conditions were kept equal to the first imaging. Compared to Figure 4.35, it was possible to a) go more in depth, and b) acquire a larger region of interest. Here, 3D images in depth coding are presented. Despite a little loss of structural data, due to the loss of fluorescence in the time and a little increase of the background noise level, it is however noticeable the presence of the dye, still surviving after two years from the first imaging.
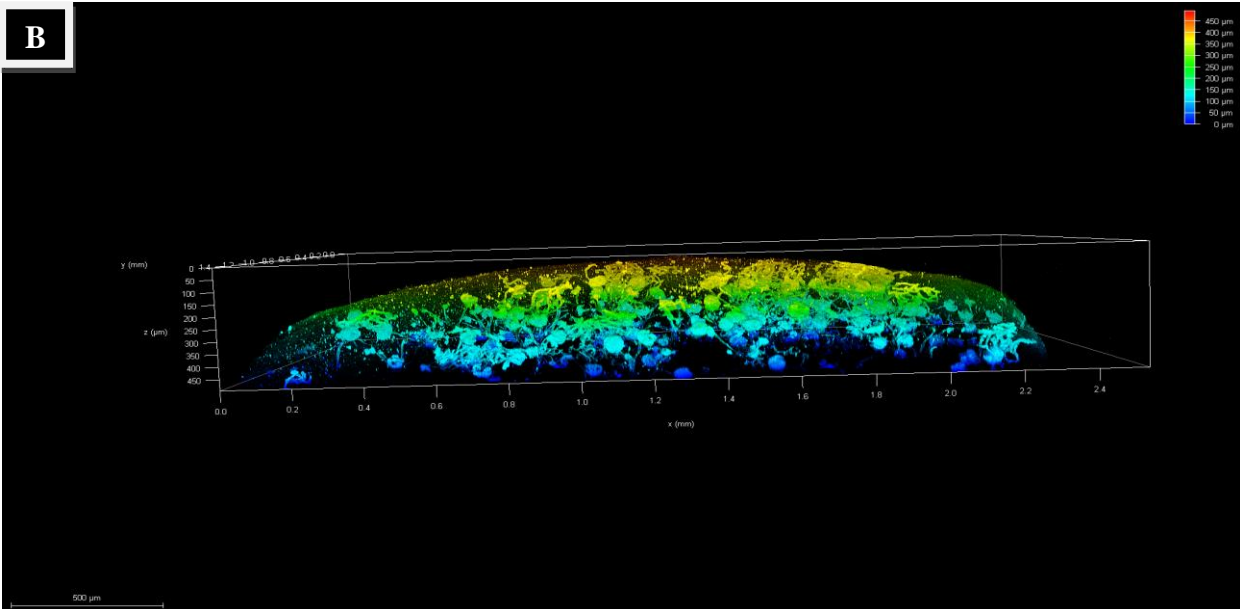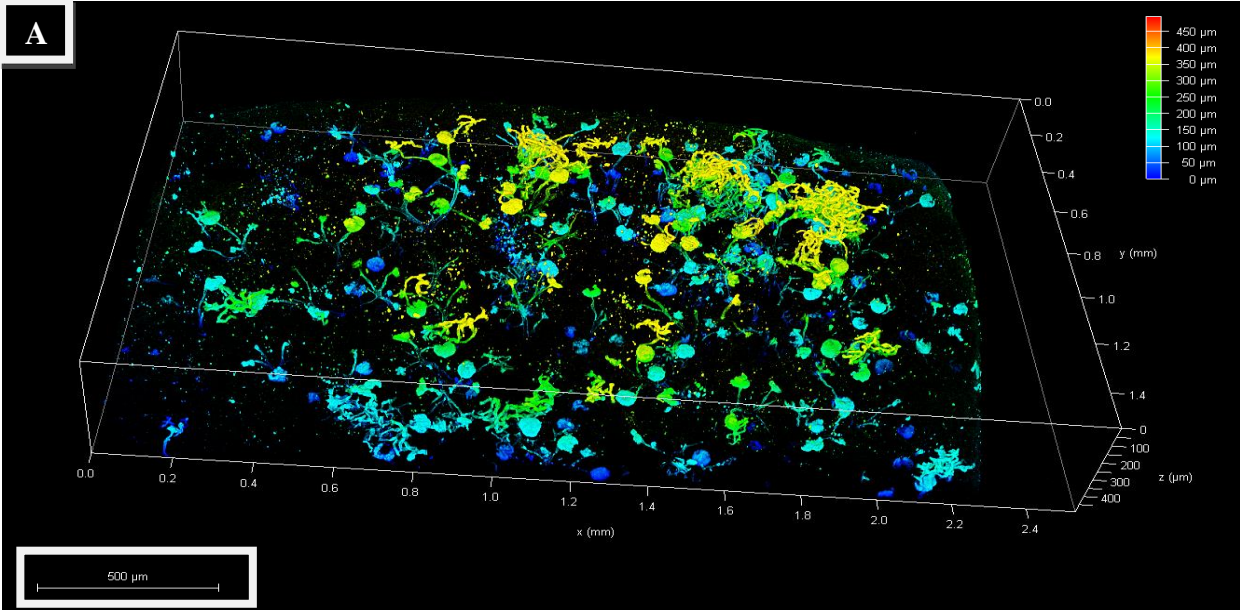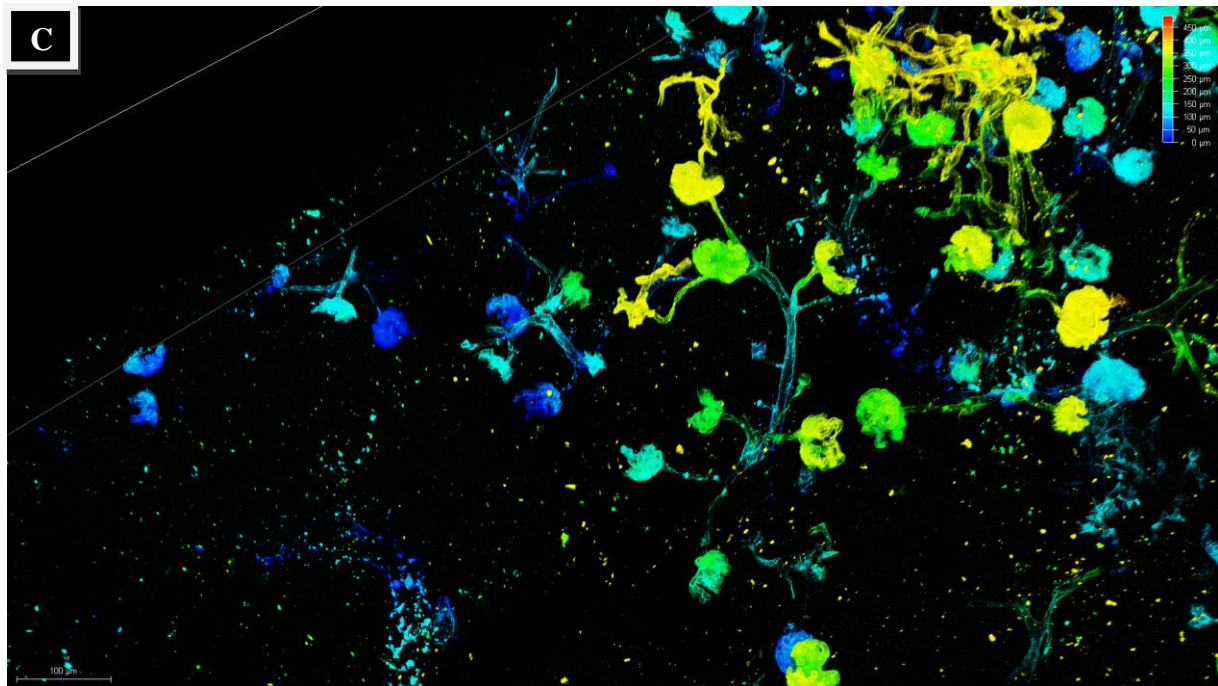
**Figure 4.36**: Kidney pole from mouse, imaged by CM, stained with Cy7-PEI-opt 4F in 3mg/ml as concentration using 20x objective in 88% glycerol and the 638 channel. 3D Tile Scan. This image was acquired by using the Stage Overview option from Las-X software (Tiles number: 15). View in depth coding from top A) and in front B). Scale bars: 500µm. C) Detail in depth coding from top showing some glomeruli and renal vessels. Scale bar: 100µm. As indicated from the depth bar on the right side of the images, the depth reached is around 500µm. This scale goes from the surface of the sample (0-150µm, in blue-light blue), middle part (100-400µm, in green-yellow) up to the deepest part of the region (400-450µm, in yellow-red).

Figure 4.37 is the results obtained from the same mouse kidney, imaged in the same conditions (including the detection of the autofluorescence), after 3 years. Surprisingly, the dye was still in place, despite a further loss of fluorescence, due to the time. In red some glomeruli and renal blood vessels are visible (from the Cy7-PEI-4F detection), whereas in green tubuli (from autofluorescence detection). Orange shadows come from the overlay of the two dyes. Because of the loss of the fluorescent signal and as indicated by the depth coding in Figure 4.37 B), the total depth detected was reduced compared to Fig. 4.36.
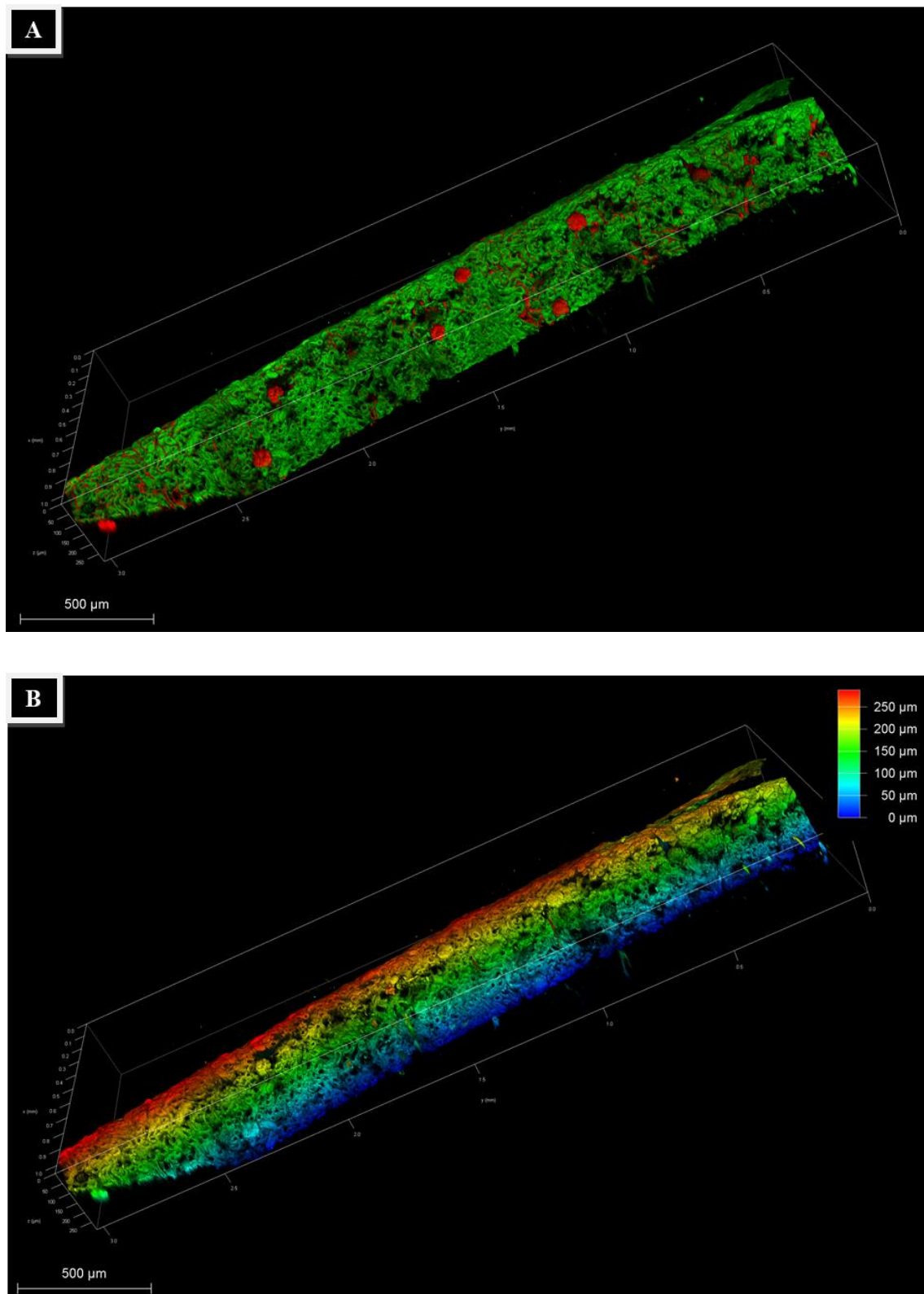
**Figure 4.37**: Kidney pole from mouse, stained with Cy7-PEI-opt 4F in 3mg/ml as concentration, imaged by CM, using 20x objective in 88%glycerol with 488 and 638 channel to detect respectively autofluorescence and Cy7-PEI-opt 4F. 3D Tile Scan. This image was acquired by using the Stage Overview option from Las-X software (Tiles number: 12). A) Scale bar: 500 µm. B) Depth coding view. As indicated from the depth bar on the right side of the images, the depth reached is around 300µm. This scale goes from the surface of the sample (0-100µm, in blue-light blue), middle part (100-200µm, in green) up to the deepest part of the region (200-250µm, in yellow-red). Scale bar: 500 µm

**4.8 Alternative Uses of Eci-based OTC**

**4.8.1 De-Paraffinization and clearing of paraffin blocks**

This section describes the results from the protocol mentioned in the paragraph 3.5.1. PCK rat kidneys, lungs and heart from 20 years old paraffin blocks as well as human kidney biopsies obtained after nephrectomy were tested and treated.

**Polycystic Rat**

Figure 4.38 shows very well detectable structural elements, even in absence of a specific staining. As a PCK rat, renal cysts are prominent, as indicated by the red arrows both in A) and in B). Moreover, it is also possible to recognize a very de-differentiated tubular epithelium, which is a characteristic of this pathology. The yellow arrow indicates also a glomerulus surrounded by an enlarged Bowman's space, another clear sign of the disease.
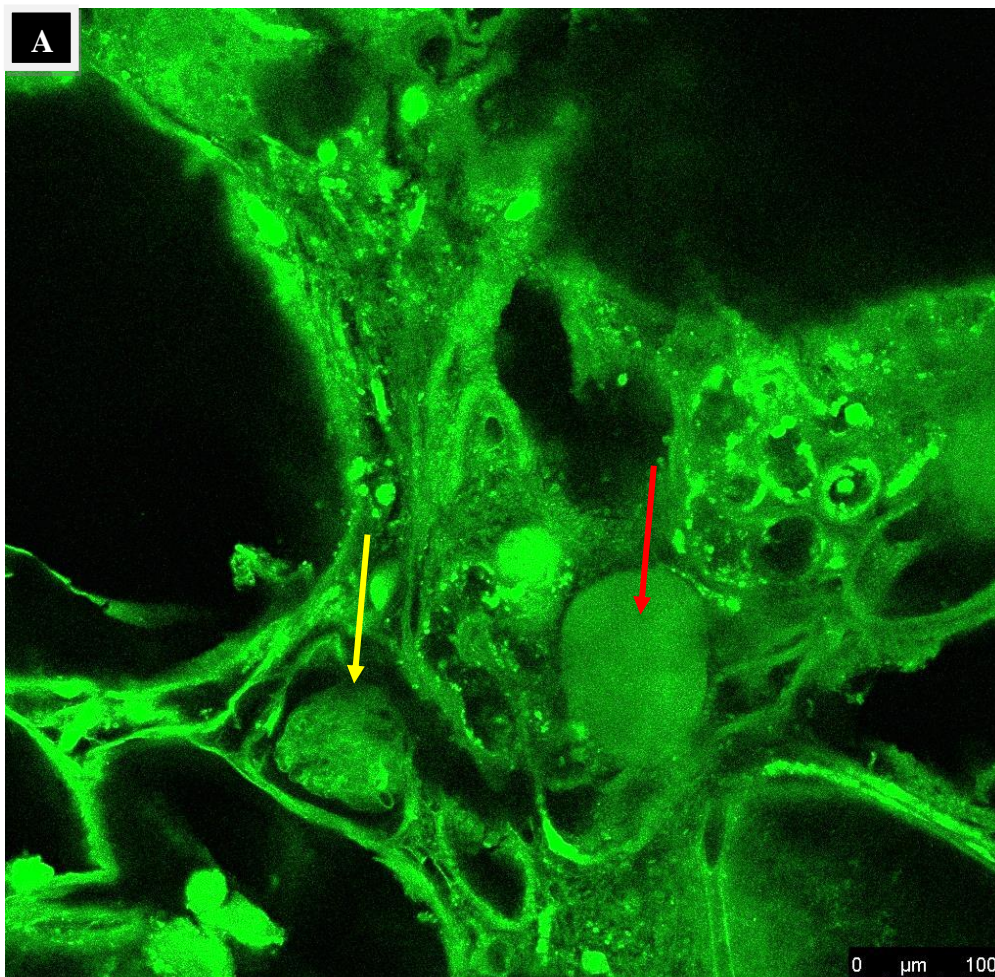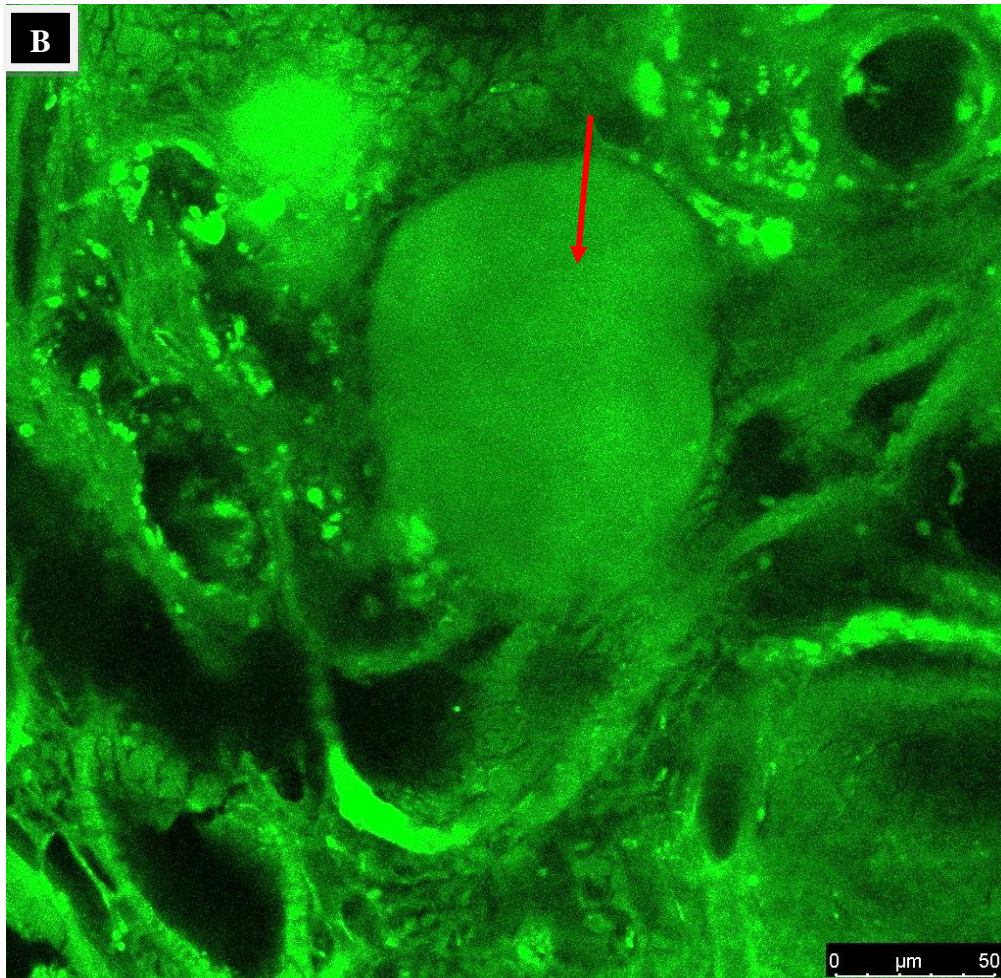
**Figure 4.38**: 2D Kidney section from a PCK rat, imaged by CM, using a 20x objective in immersion oil. No staining. Autofluorescence detected by 488 channel. A) 2D view. Scale bar: 100µm. B) Zoomed in view of A). Scale bar: 50µm

The images shown in Figure 4.39 A), B) and C) were acquired after de-paraffinisation and clearing of 20 years old paraffin embedded sample: surprisingly, the inner structures survived the whole protocol. In fact, these images show the glomeruli and renal tubuli with a very low background noise level. Remarkable is also the depth reached, considering the age of the paraffin block. The zoomed in glomerulus shown in C) depicts a much enlarged Bowman's capsule, clear sign of this pathology.
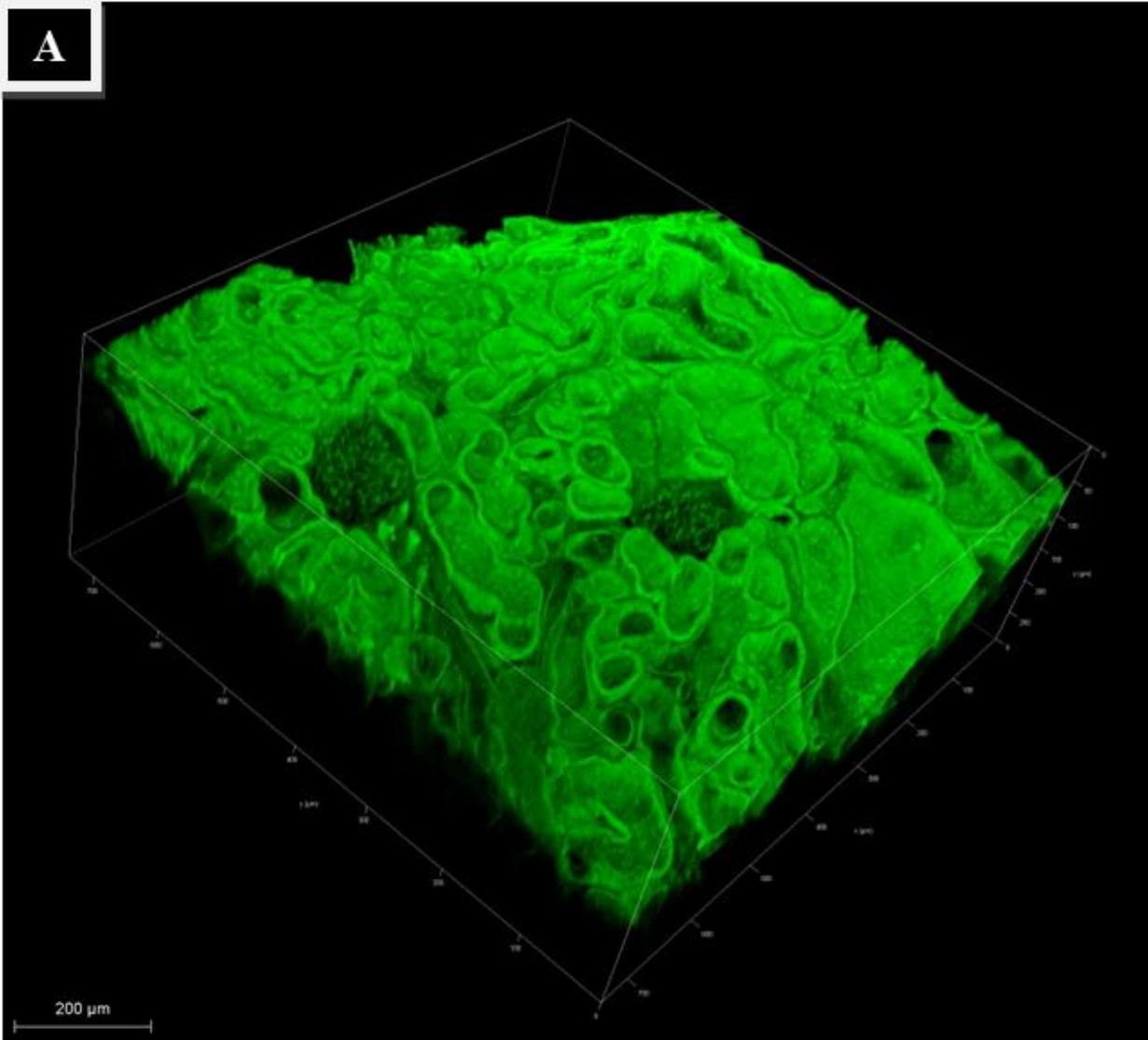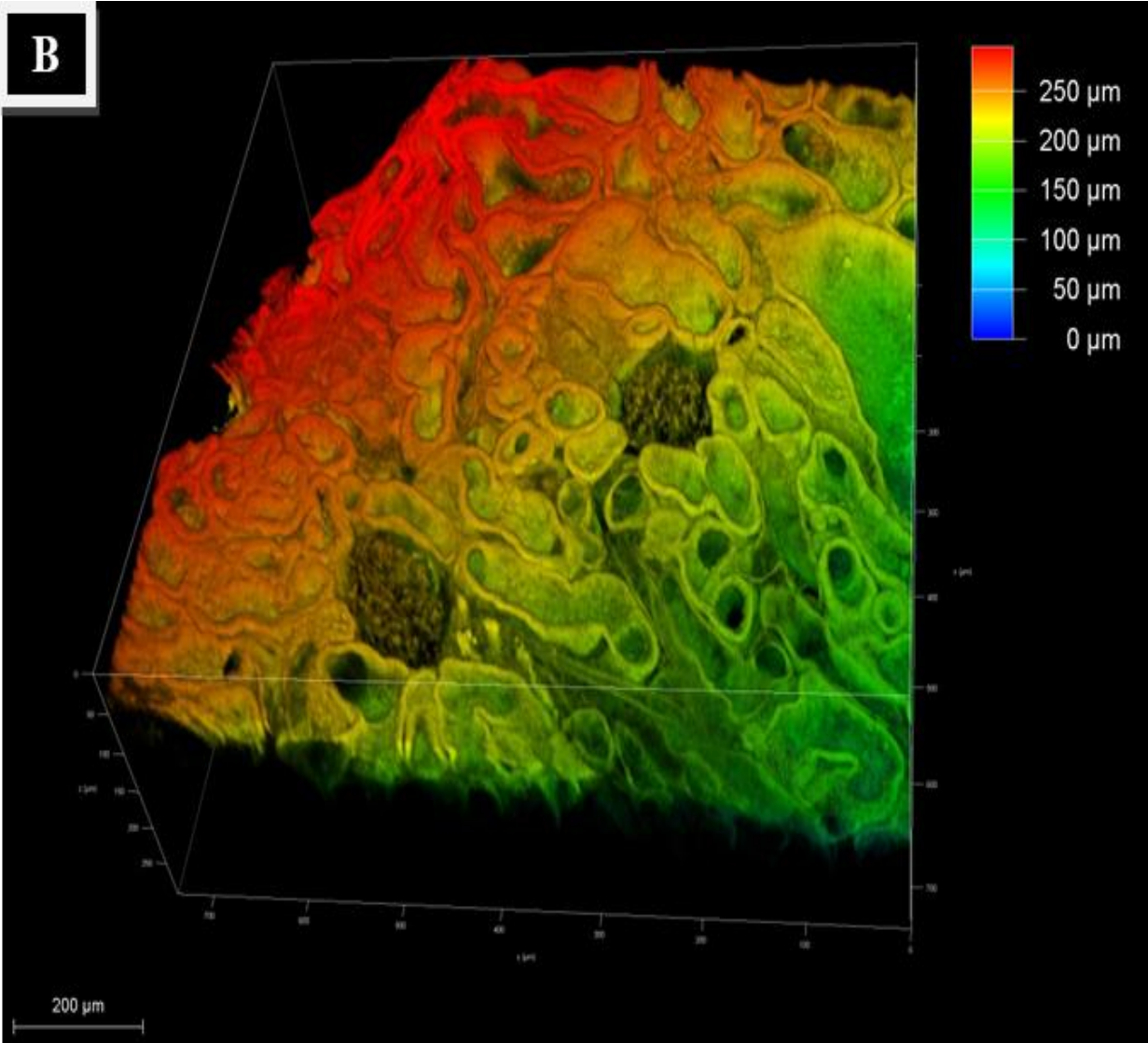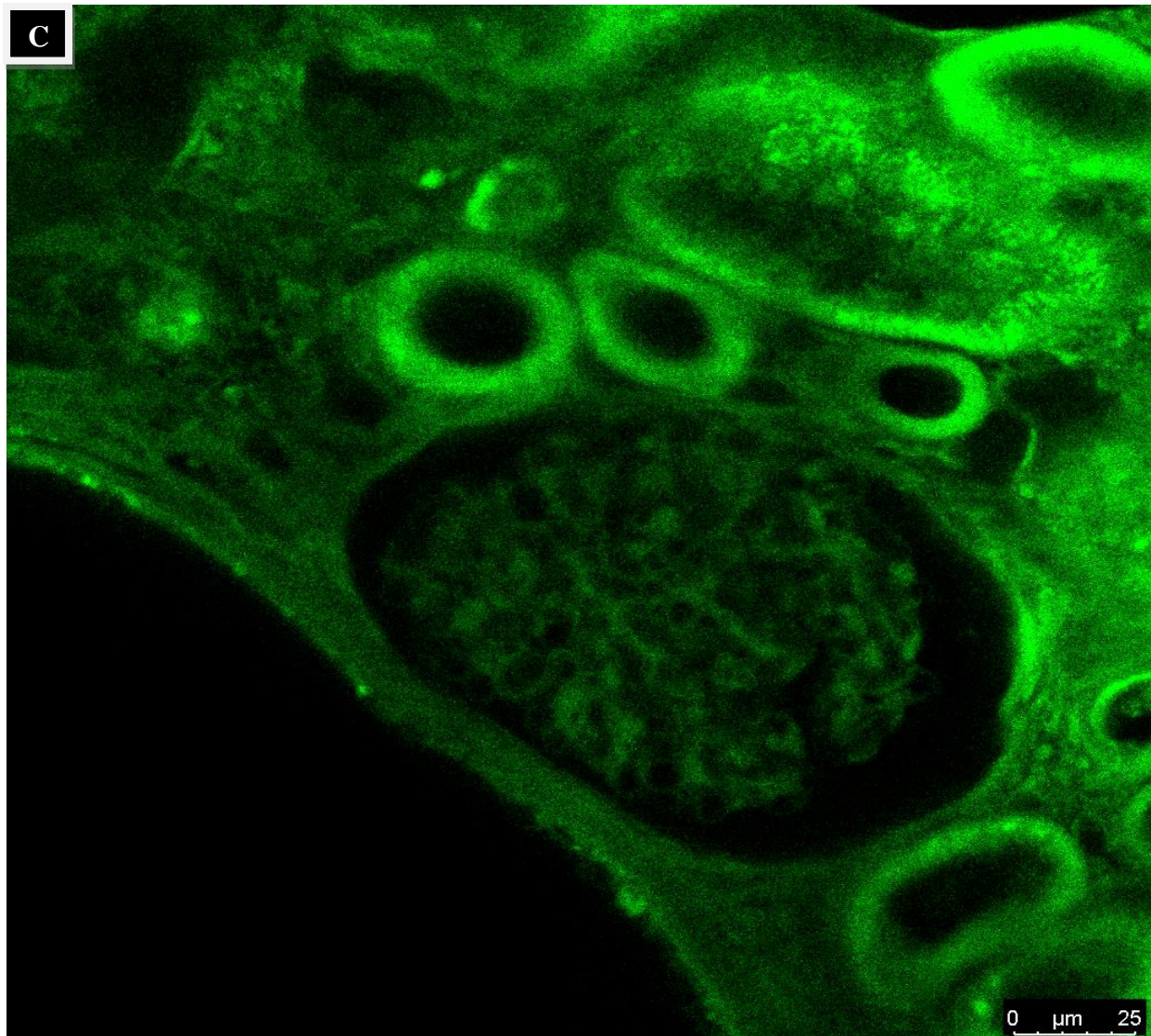
**Figure 4.39**: A de-paraffinised and cleared section from a PCK kidney rat. The original paraffin block was made in 1998 and further processed in 2018. Imaging acquired by CM, using a 20x objective in immersion oil and 488 channel for autofluorescence detection. A) 3D image. Scale bar: 200µm. B) 3D view in depth coding: as indicated by the scale on the right side of the image, this goes from the most superficial region (0-100µm in blue-light blue), middle part (100-200µm in green) up to the deepest part (200-250µm, in yellow-red). Scale bar: 200µm. C) 2D zoomed in view of a glomerulus Scale bar: 25 µm.

After the clearing procedure and before the imaging, the PCK rat lung shown in Figure 4.40 was stored in ECi for 6 days and, furthermore, imaged by CM using only autofluorescence for structures detection. The 3D images in A) and B) show the pulmonary artery and all the alveolar structures, indicated in the figure. Figure 4.40 C) underlines, in 2D, also the presence of some erythrocytes, which have their own strong autofluorescence.
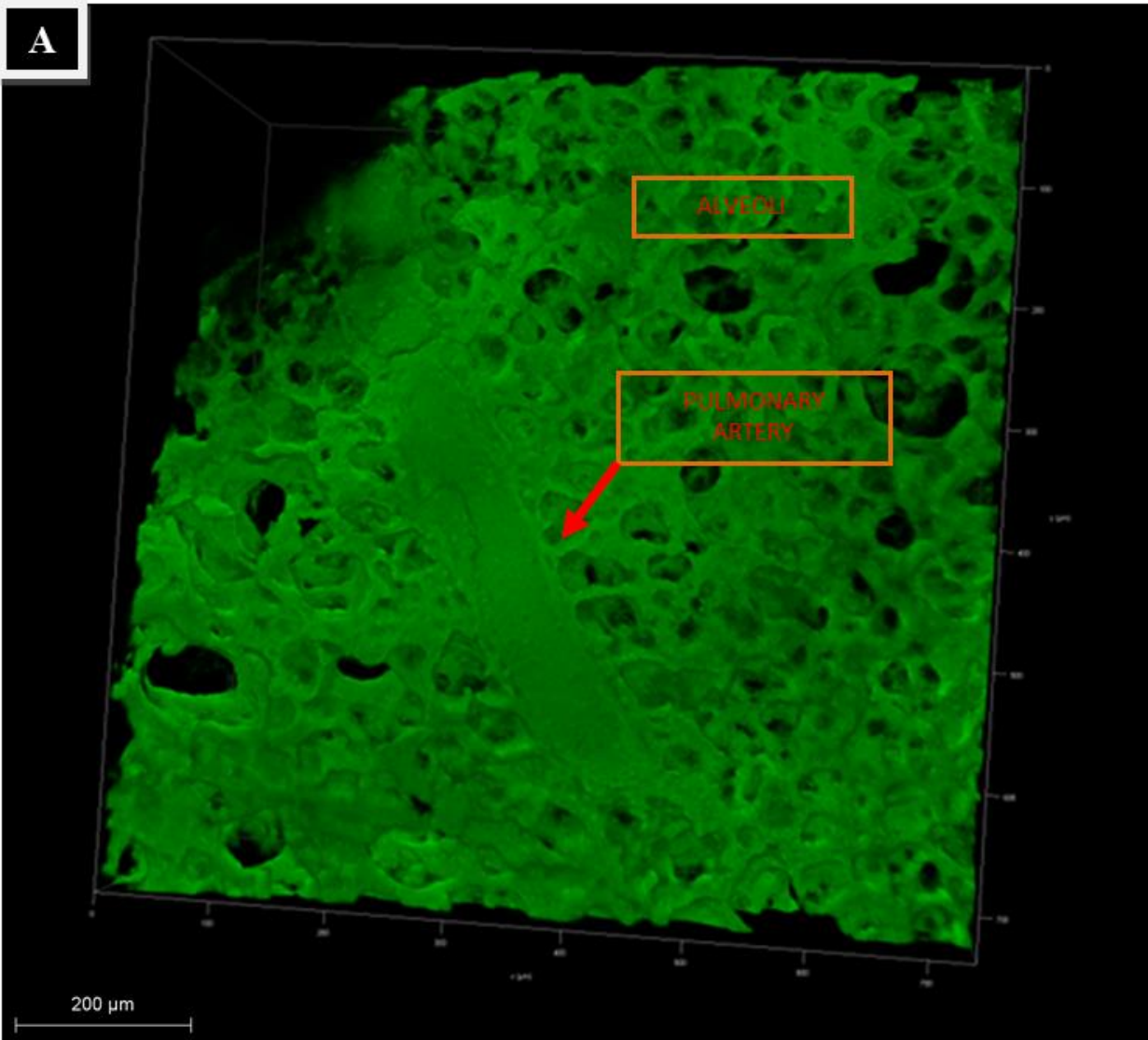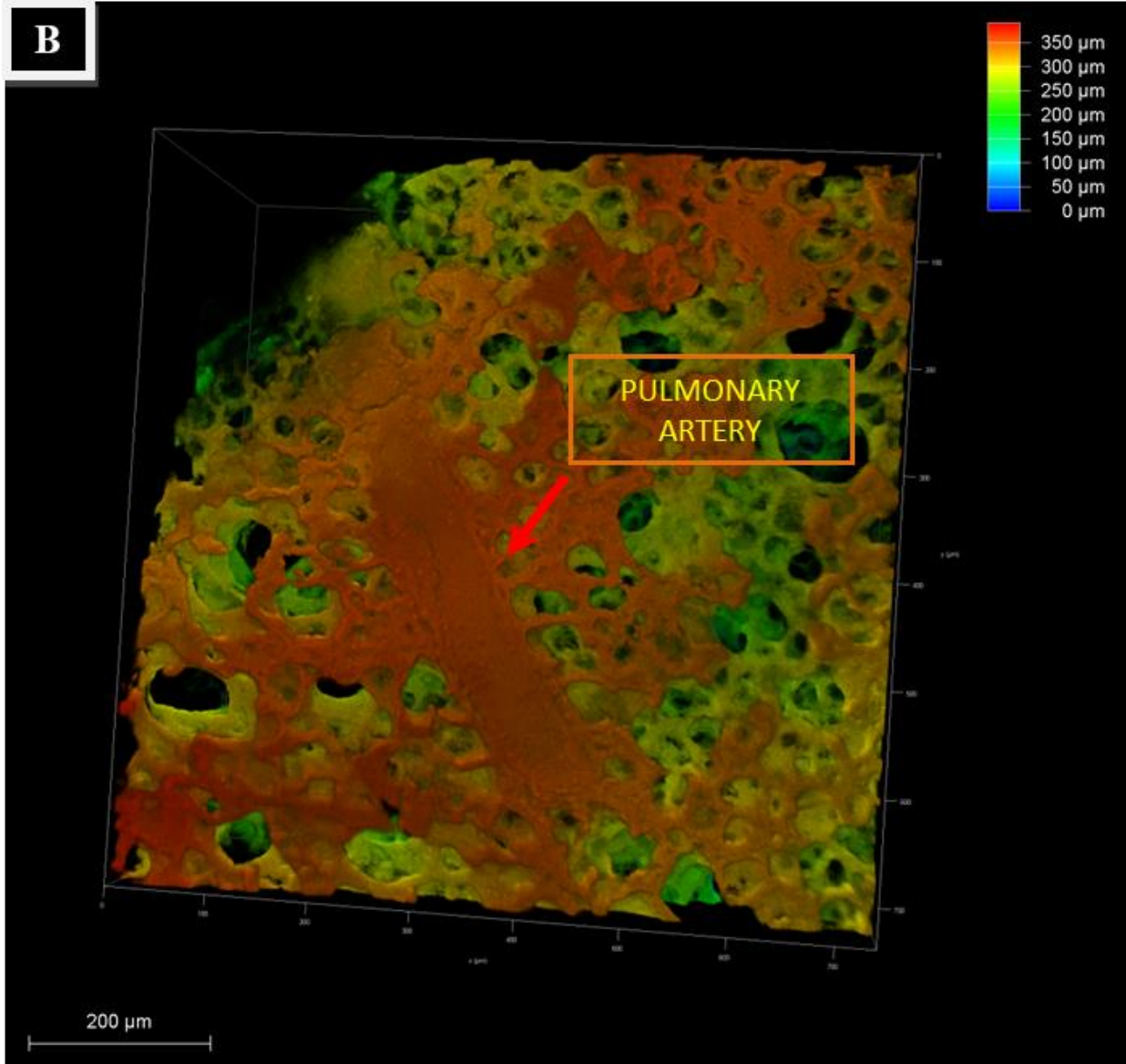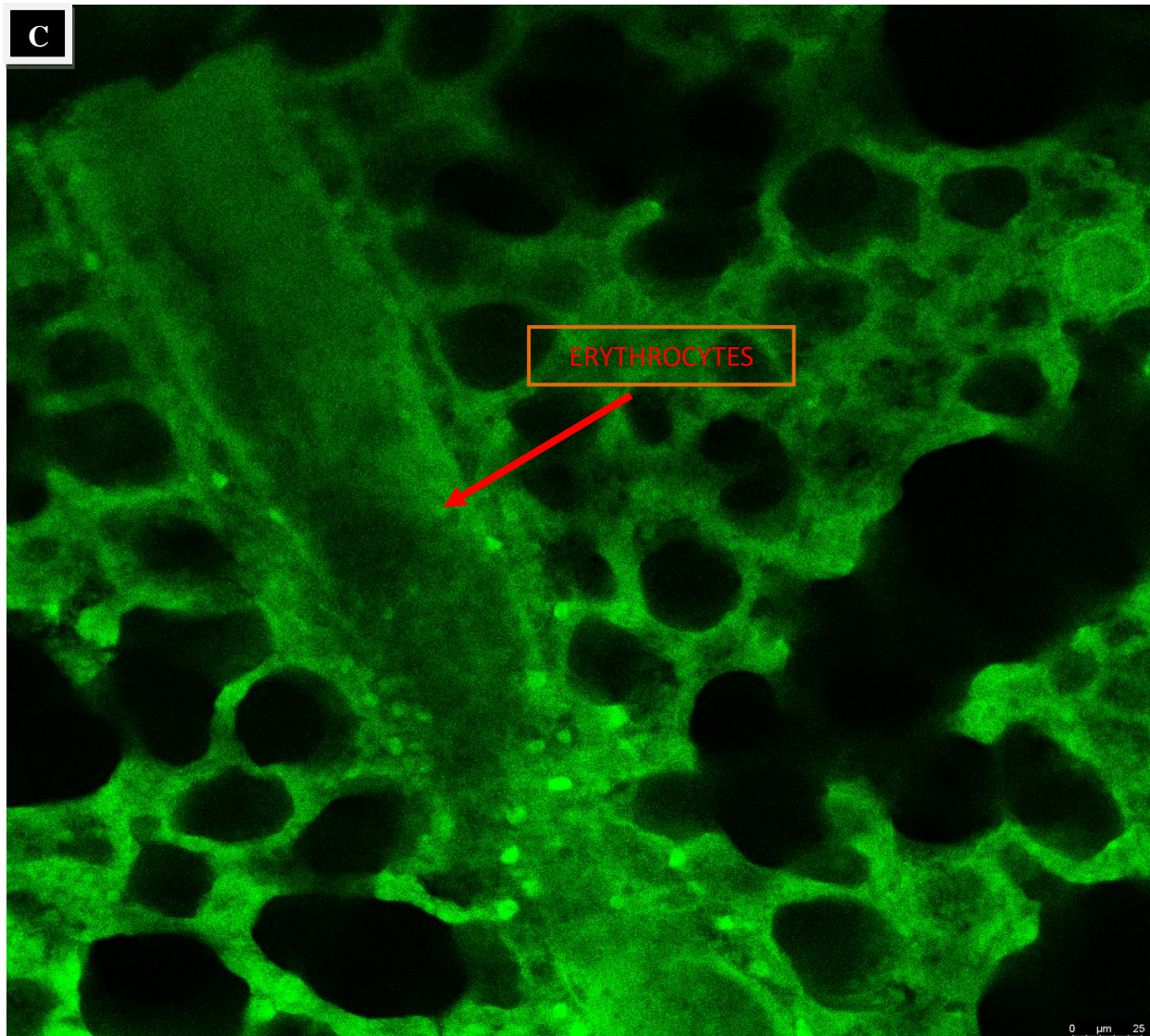
**Figure 4.40**: A de-paraffinised and cleared section from a PCK rat lung. The original block was made in 1999 and further processed in 2019. Imaging acquired by CM, using a 20x objective in immersion oil and 488 channel for autofluorescence detection. A) Scale bar: 200µm. B) 3D view in depth coding: as indicated by the scale on the right side of the image, this goes from the most superficial region (0-100µm in blue-light blue), middle part (100-300µm in green - yellow) up to the deepest part (300-350µm, in orange-red). Scale bar: 200µm. C) Zoomed in view of the pulmonary artery, with erythrocytes in there. Scale bar: 25µm

Figure 4.41 depicts a de-paraffinised and further cleared slice of heart from a PCK rat. After the clearing protocol and before the imaging, the sample was stored 3 days in ECi. Only autofluorescence was used to detect the structures. As indicated by the red arrows, it is possible to easily and clearly distinguish muscle fibres as well as erythrocytes.
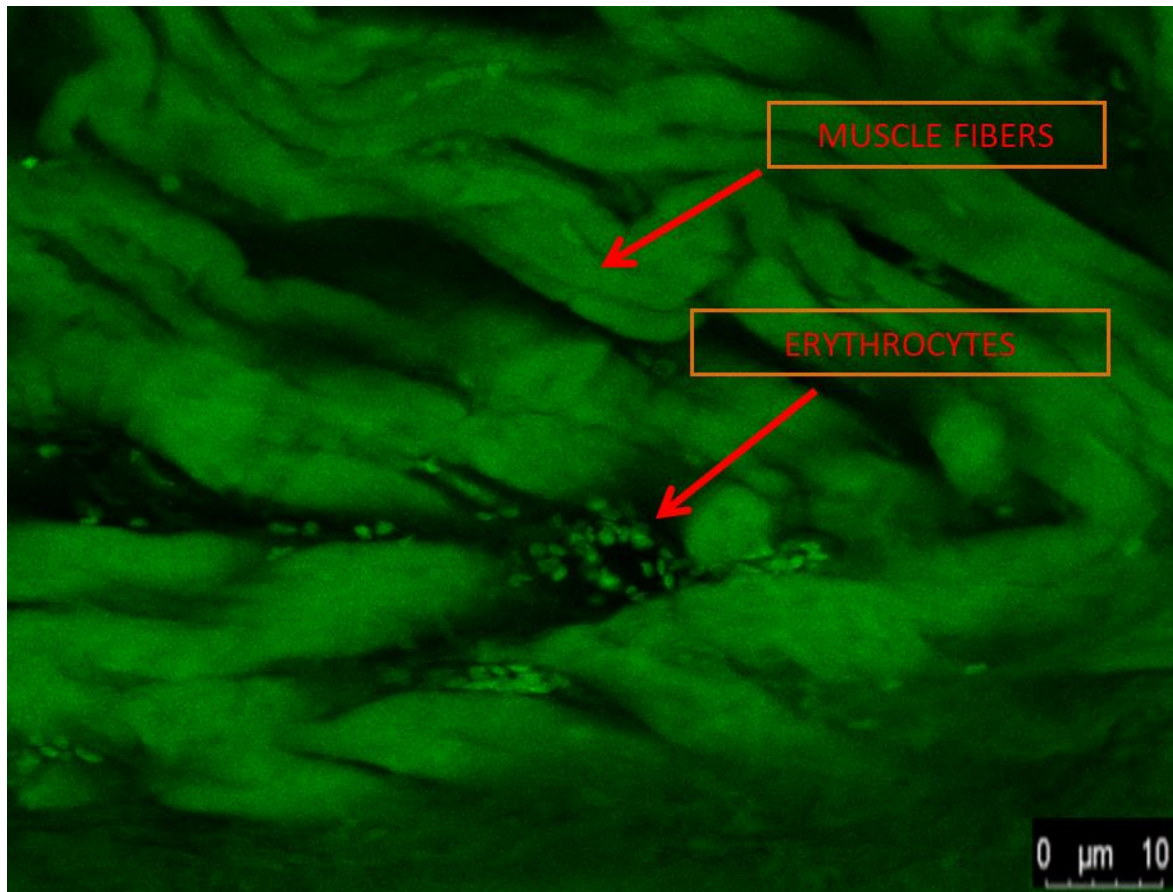


**Figure 4.41**: A de-paraffinised and cleared slice from a PCK heart rat. The original block was made in 1999 and further processed in 2019. Imaging acquired by CM, using a 20x objective in immersion oil and 488 channel for autofluorescence detection. Scale bar: 10μm

**Human Kidney**

In collaboration with the Pathology Department of the Universitäts Klinikum of Mannheim, some human kidneys were obtained to be de-paraffinised and treated with ECi-based OTC, as shown in Figure 4.42. After a nephrectomy, a paraffin block was prepared. Furthermore, it was de-paraffinised and made ready for the OTC, but without staining. Nevertheless, the only autofluorescence detection allowed the visualisation of some renal structure. In fact, in A), it is possible to visualise a glomerulus and its Bowman's space, which is enlarged because of

the disease. Even a set of tubules is recognisable. In B), "empty" cysts and renal tubuli are displayed.
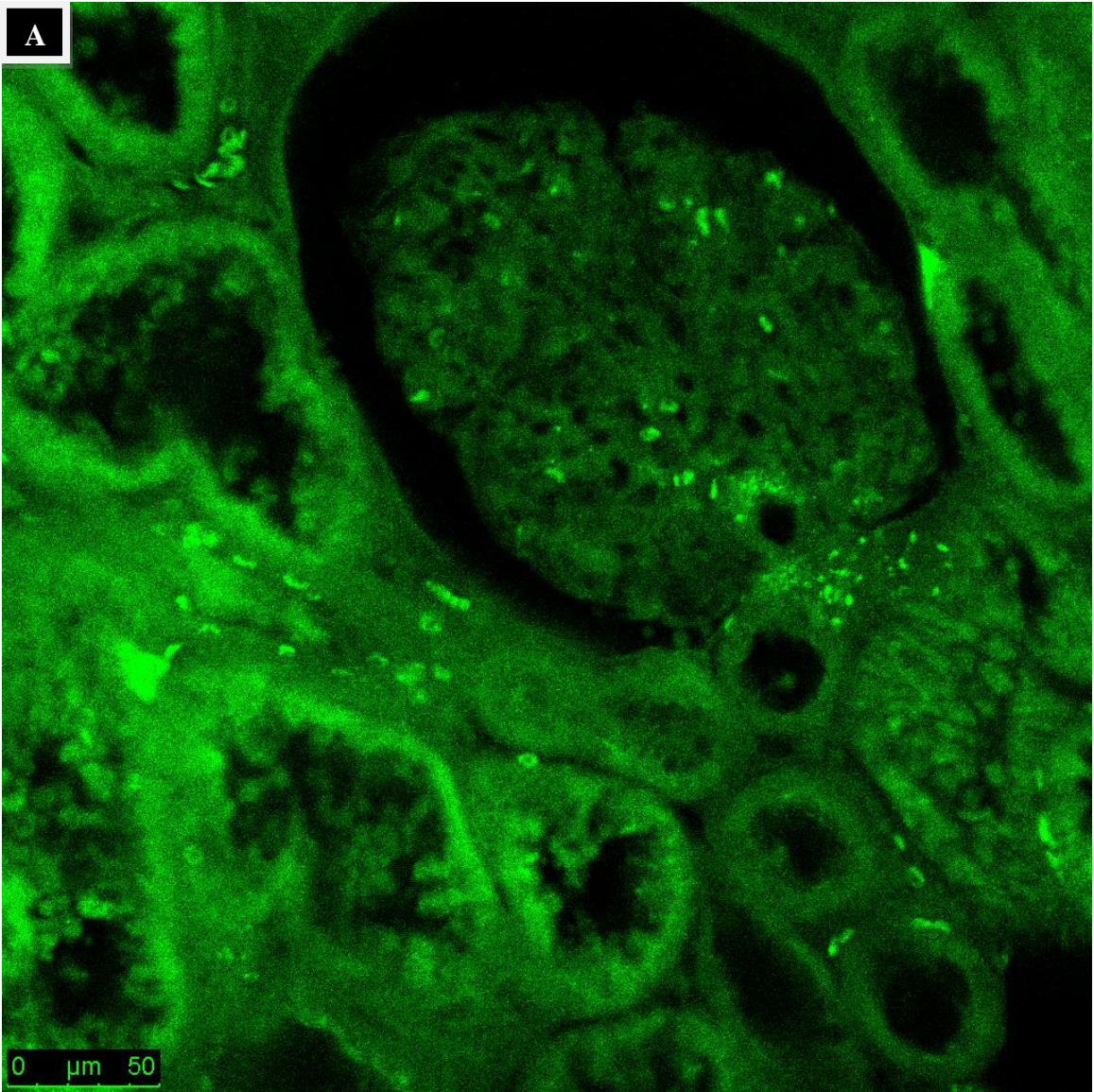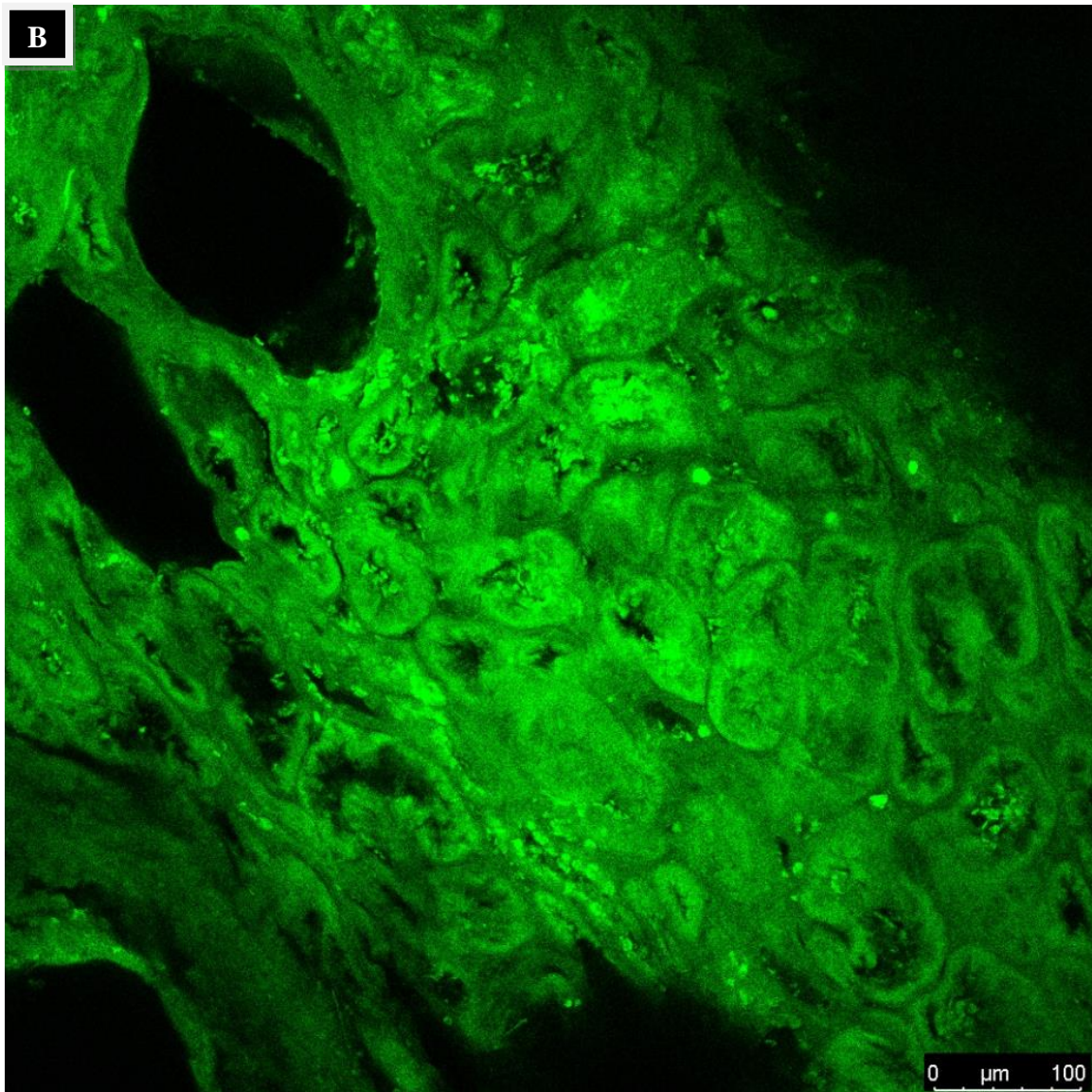
**Figure 4.42**: Human kidney section, from human kidney biopsy. After de-paraffinisation and clearing, this was imaged by CM, using a 20x objective in immersion oil and 488 channel for autofluorescence detection. A) Glomerulus and enlarged Bowman's space. Scale bar: 50μm. B) A set of renal tubuli and empty cysts. Scale bar: 100μm

### 4.8.2 ECi removal and 3D Immunohystochemistry

In the following paragraph, images regarding ECi removal by high ethanol concentrations, followed by rehydration and further 3D-IHC, will be listed and described. All the following images will report results obtained following the protocol described in the paragraph 3.5.2. After proceeding with ECi removal by high ethanol concentrations and further rehydration, 3D-IHC was performed.

Figure 4.43 A) and B) reports the results obtained by the imaging of 1mm slide from mouse kidney stained with an antibody against nephrin as primary and Anti Goat Secondary Antibody AlexaFluo 647 conjugated. Figure 4.43 A) defines a tile scan, where the red colour refers to AlexaFluo 647 detection, which worked to identify glomeruli, in high number, for a total depth of 350µm (depth coding not shown). The autofluorescence was useful to distinguish the renal tubuli, and, in this way, a good combination for the visualization of all main structures was obtained. In B), the glomerulus is very distinct: the slit membrane is well structured and recognisable. Although not completely defined, this is surrounded by renal tubuli, in which, by a negative contrast some cells nuclei are also easy to follow.
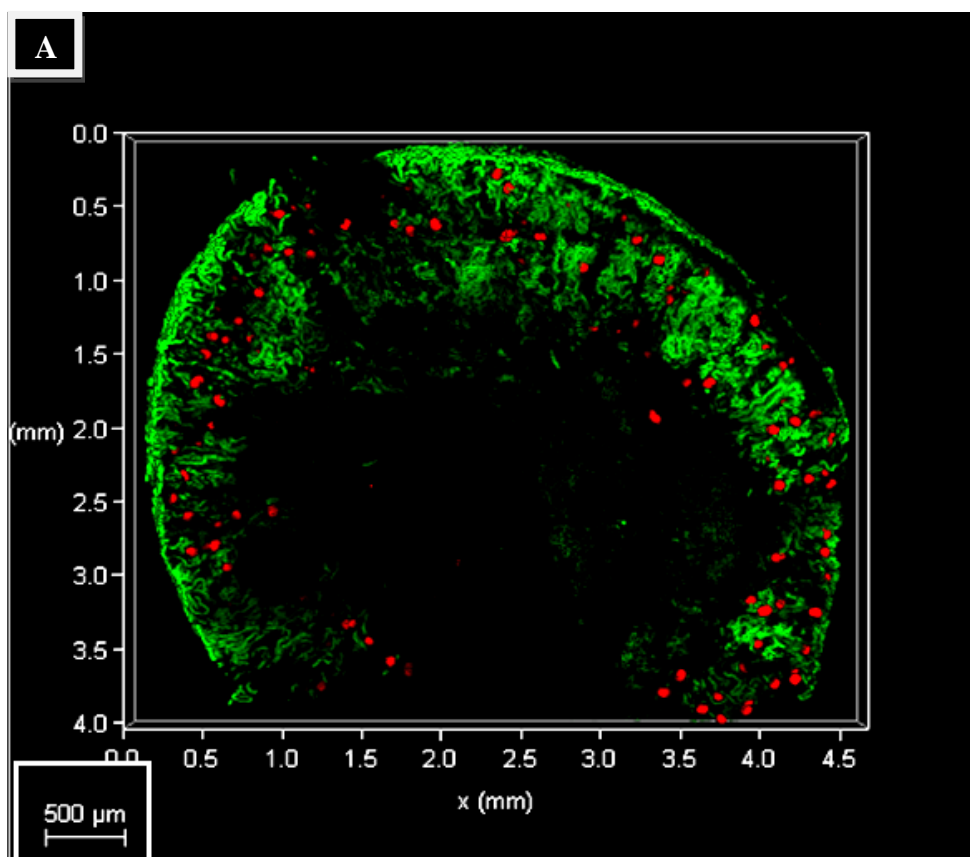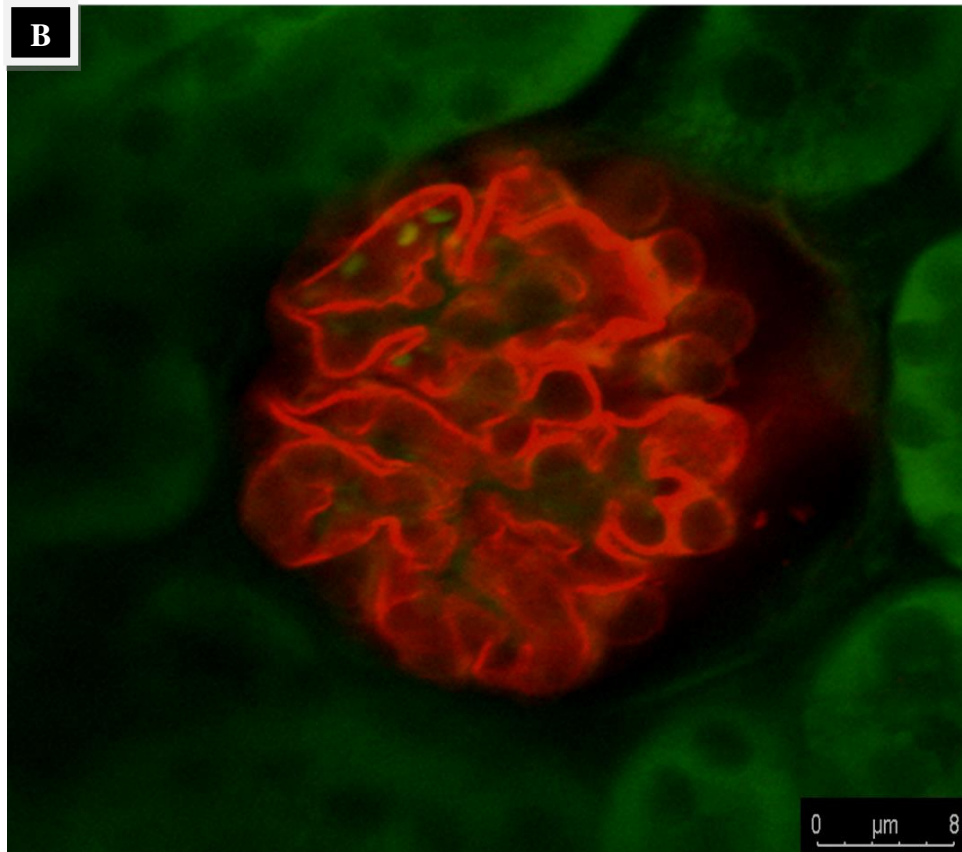
**Figure 4.43**: Mouse kidney section (1mm) cleared and rehydrated to remove the ECi, stained with primary antibody against nephrin and Chicken Anti Goat Secondary Antibody-AlexaFluo 647 conjugated. This was imaged by CM, using a 20x objective in 88% glycerol and 638 and 488 channels, respectively for AF647 and autofluorescence detection. A) Tile scan of the whole section. Scale bar: 1mm. B) A zoomed in view from A), where a glomerulus is displayed. Scale bar: 8μm

Figure 4.44 A) and B) presents the results of a second experiment, performed keeping the same experimental setup as the previous one. As in the previous images, the glomeruli (in red) are evident and well-shaped and the renal tubuli were detected by autofluorescence (in green). Within them, it is also possible to recognize epithelial cells nuclei, represented as dark dots, due to the negative contrast.
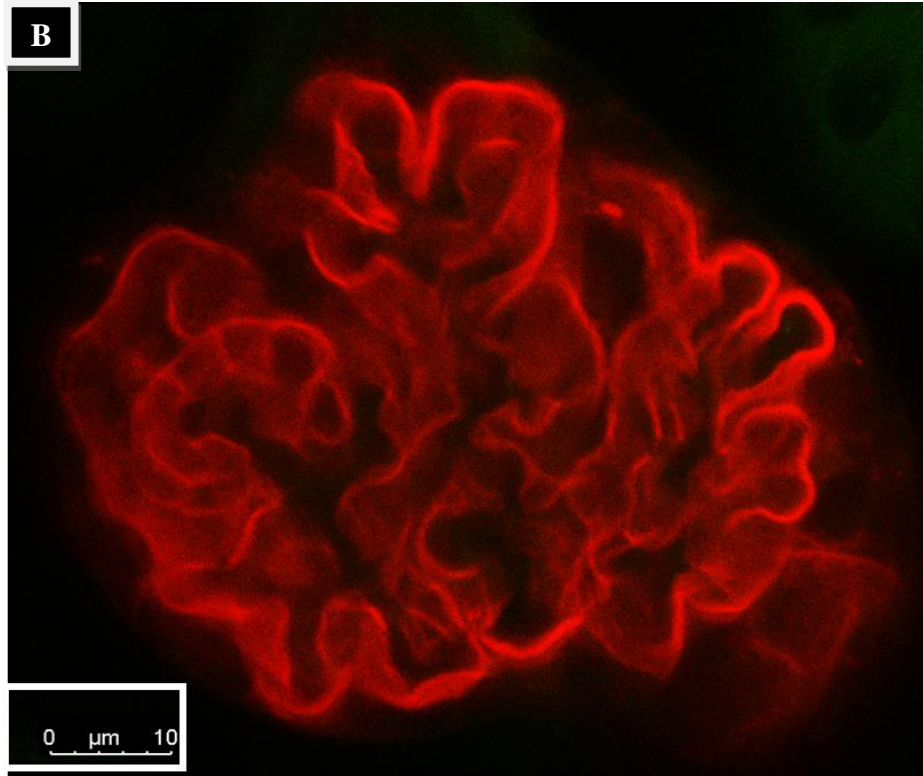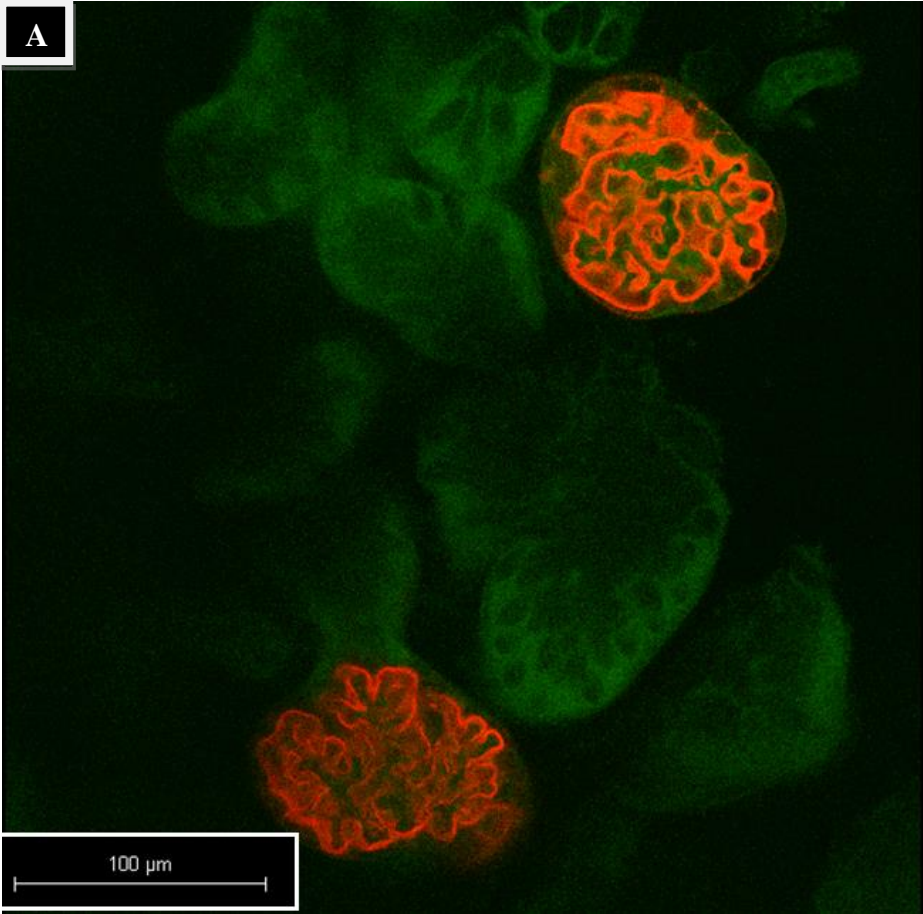
**Figure 4.44**: Mouse kidney section (1mm) cleared, rehydrated to remove ECi, stained with primary antibody against nephrin and Chicken Anti Goat Secondary Antibody AlexaFluo 647 conjugated. This was imaged by CM, using a 20x objective in 88% glycerol and 638 and 488 channels, respectively for AlexaFluo 647 and autofluorescence detection. A) Scale bar 100µm. B) Zoomed in view from A). Scale bar: 10µm

In Figure 4.45 results concerning nuclear staining are reported. In fact, in the following images, in addition to glomeruli, nuclei from epithelial cells were stained. In A) the results from the only nuclear staining (made with Sytox™ Green) are presented; in B) the red channel (anti-nephrin AlexaFluo 647 conjugated) related to the only glomeruli and in C) the overlay is depicted. However, due to the same wavelength spectrum range between autofluorescence and Sytox™ Green, it was possible to detect and reveal also renal tubuli, providing an almost complete overview regarding all the renal structures. In addition, the background noise level is very low, demonstrating the high specificity of both staining. The 63x objective was required in order to obtain a better quality of the cellular nuclei, which are completely visible and detectable. The total depth reached (here not shown) is equal to 90µm. This value is significantly lower than the depth reached in other images and this is due to the working distance of the 63x, equal to 0.14mm.
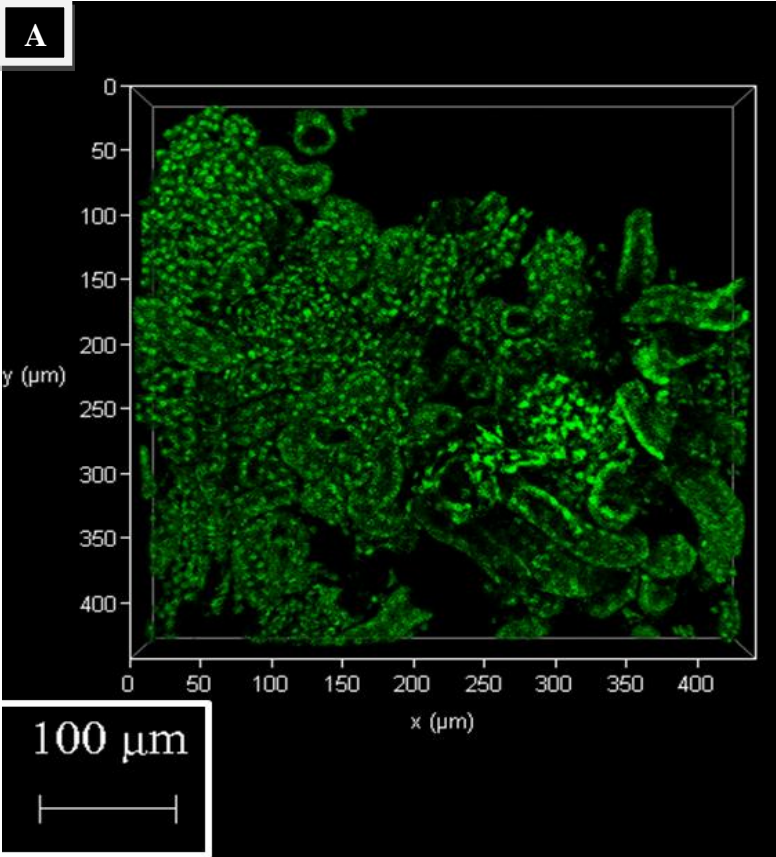
**Figure 4.45**: 3D Mouse kidney section (1mm) cleared, rehydrated and stained with primary antibody against nephrin, chicken anti goat secondary antibody AF647 conjugated and counterstained with Sytox$^{TM}$ Green for cellular nuclei detection, imaged by CM, using a 63x objective in 88% glycerol and 488 and 632 channels, respectively for AlexaFluo 647 and Sytox$^{TM}$ Green detection. A) Green channel detecting Sytox$^{TM}$ Green (epithelial cell nuclei). B) Red channel detecting AlexaFluo 647 (glomeruli). C) Image in overlay. Scale bars: 100µm
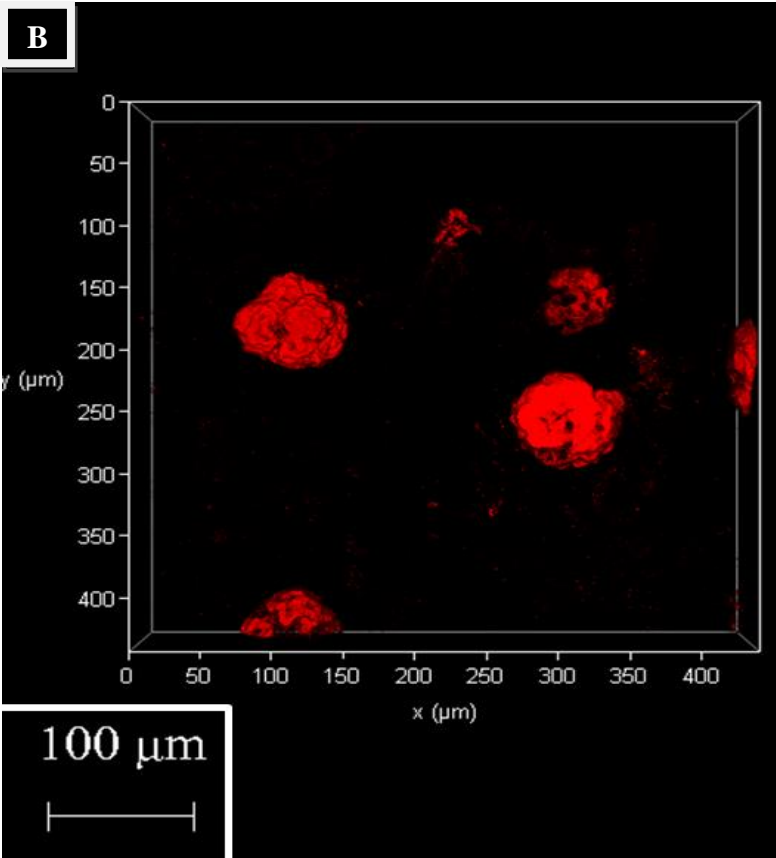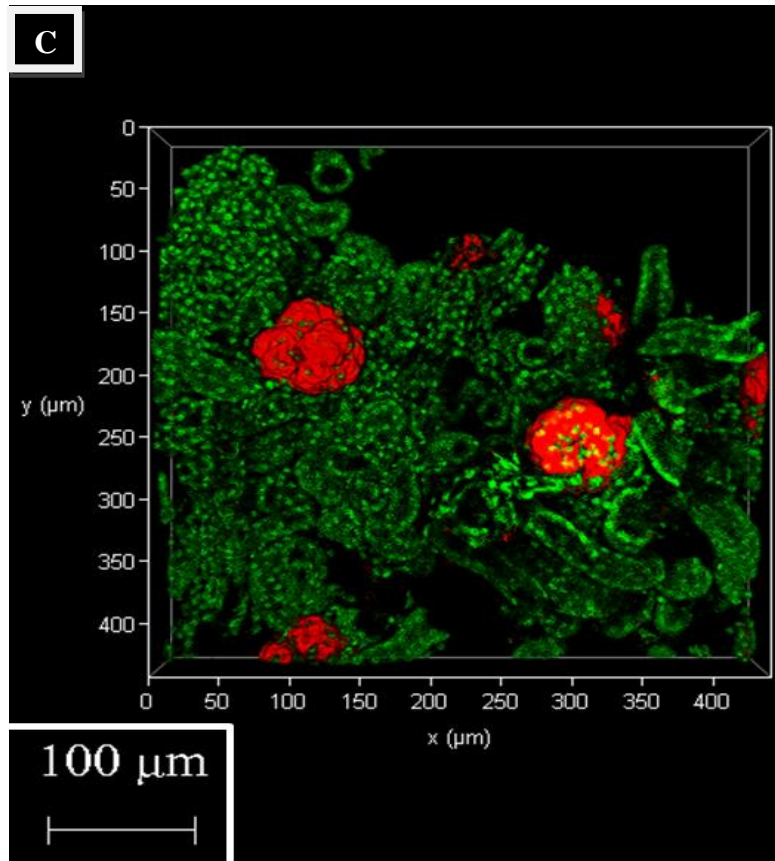
In order to evaluate the physical modifications and glomerular size changing after perfusion, clearing and ECi removal/rehydration, some experiments were performed. First, after each step some pictures were taken, as reported in Figure 4.46; second different measurements were performed on glomeruli diameter by using the Las X software and taking the largest point in a z-scan, as reference (Fig. 4.47).
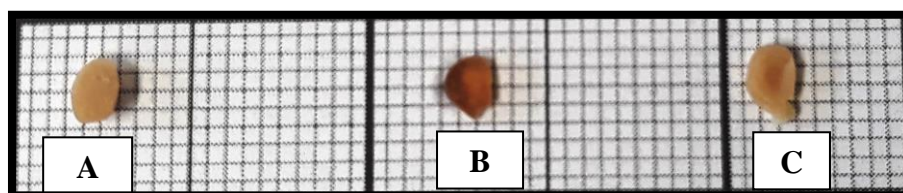


**Figure 4.46**: Mouse kidney slices (1mm) after perfusion (A), ECi-based OTC (B), ECi removal and rehydration (C). This picture shows the appearance of the mouse kidney slices after each step prior to the antibody staining itself. Sqare paper unit of measurement: 1mm. Images acquired by Samsung SM-J53F
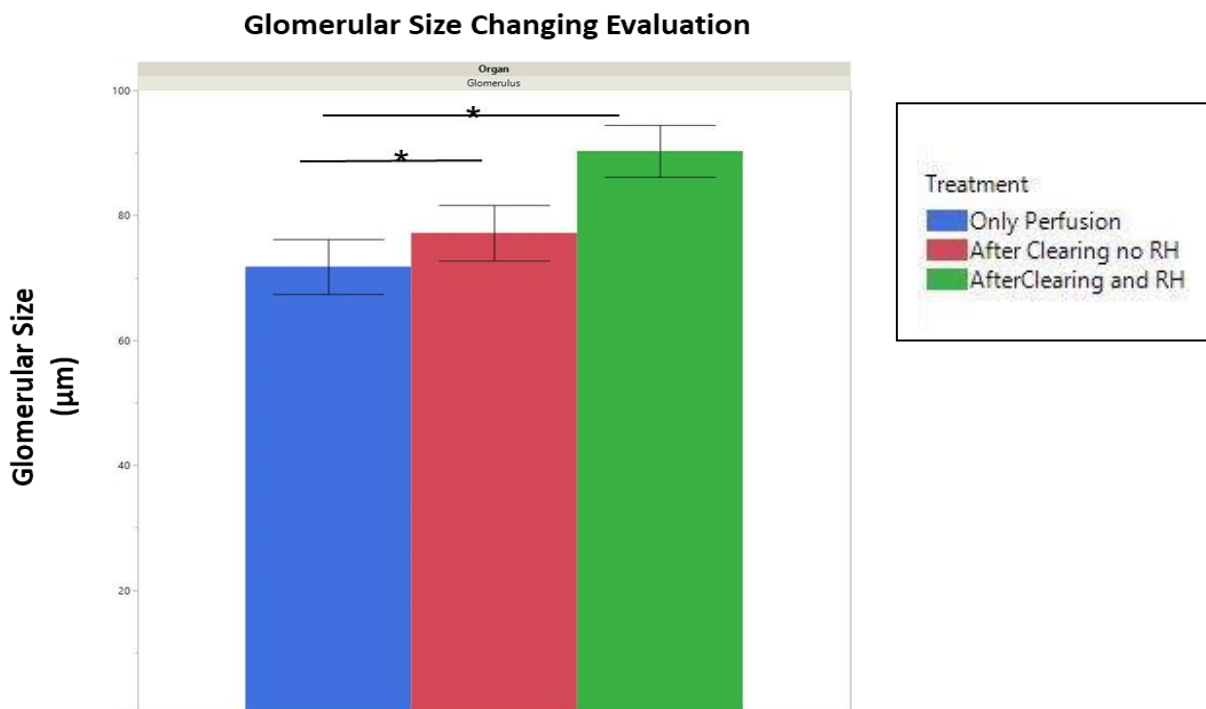
**Figure 4.47**: Glomerular size changing based on diameter measurement (Las X software). Bar plot show the measurement immediately after the perfusion (on the left-group a), after the clearing procedure (center- group b) and after the rehydration step (on the right- group c). An oneway ANOVA test was performed to compare the mean values for the three groups. The asterisk denotes significance ($p < 0.05$) in paired t tests and error bars denote SD. The sample size is n=6. RH= Rehydration.

As shown from the graph, an increase of the glomerular size was noticed: 1) between group c) and a): +18.50µm; 2) between group c) and b): +13.12µm; 3) between group b) and a) +5.38µm.

# 5. Discussion

Starting from the original ECi-based OTC protocol[52], a new optimized procedure was developed. This optimization consisted in: a) strongly shortening the times, by optimizing the protocol steps. In fact, the timing of the protocol was reduced from 16 hours (as described in the published protocol[52]) down to 5 hours (although the samples may stay longer in the ECi solution, for example overnight); b) completely automating the procedure with the use of the tissue processor, where all the settings may be easily programmed and it is possible to clear many samples in one run, without affecting the efficacy of the clearing. Moreover, the tissue processor assures the presence of a negative pressure, which prevents the formation of air bubbles in the samples; c) making the dehydration step faster and shorter. By skipping the step with 30% and 70% ethanol (as described by Klingebrg[52]), in this optimization, the samples were brought from 50% directly to 80% ethanol, ensuring a stronger and faster dehydration, before immersing the samples into absolute ethanol; d) changing the temperature from 4°C to RT, in order to improve the diffusion coefficient of the substances, so that they may better penetrate and diffuse into or out of the tissues. Two of the mainstays of this protocol are the speed of action and the low harmfulness of the ECi, being also a FDA-approved food flavor and additive for cosmetic products since 2007[54]. Furthermore, different toxicity studies were conducted on ECi (oral, dermal, intramuscular studies, both on animals and humans), demonstrating that the use of ECi is not toxic and it can be used in different preparations of daily life (e.g. body lotions, face creams, bath products)[64].

By contrast, many other OTC protocols, which have been described during the last years, are highly time-consuming, being based on very long incubation times (days to weeks). Moreover, they also require very expensive, harmful and hard to handle clearing solution, as, for instance, in ACT (active clearing technique), X-Clarity, Scal*e*, BABB, CUBIC[23-25, 65, 66]. In addition, substances with high RI values are considered better to obtain an optimal tissue clearing, as they can easier match with the RI of the biomolecules, where the RI overall tissue is generally defined in a range of 1.4-1.5[4, 9, 10]. However, one of the most important drawbacks of these high RI clearing solutions is their toxicity and harmfulness[1]. The high ECi RI, together with its no-toxicity, makes that an optimal clearing solution, given its ability to homogenize the tissue RI, with a strongly reduced risk for the operator. In addition, the use of ethanol is strongly recommended to remove membrane-associated lipids[67]. In fact, due to their chemical properties (presence of hydrogen bindings, electrostatic and hydrophobic interactions), the ethanol is the best candidate for the removal of lipids from cell bilayers

membranes[67]. Therefore, the speed of action ensured by the automation, high RI combined to the low harmfulness and economy of the product, make our ECi-based optimized OTC one of the best choice in this scenario.

## 5.1. Advantages of a retrograde perfusion

In the blood circulation, different molecules (as haemoglobin and myoglobin) contribute to a strong light absorption and, consequently, to the autofluorescence phenomenon, which may interfere with further analyses of the samples[2]. In order to reduce this inconvenience, the perfusion technique aims to remove blood from the body of the animal, under anesthesia. Depending on the purpose, two main approaches of perfusion have been described, retrograde and antegrade perfusion. In particular, the first one was described by Langendorff in 1895[68]. He established a retrograde way to perfuse animals, so that the perfusion buffer may flow retrogradely up the aorta, in an opposite way than the normal physiologic flow[68]. With that it is possible to perfuse by using either constant pressure or constant flow[68, 69], and a cheap equipment. In Langendorff's original work, the constant pressure was achieved by using a pressurized chamber connected to a manometer[68, 69]. Other reasons for the longevity of the retrograde perfusion are the simplicity of the preparation and the reproducibility of the method. The constant pressure/flow assures the integrity of the organs, after their harvesting from the animal body[69].

On the other hand, in the antegrade perfusion the perfusate is injected from the apex of the left ventricles[70].

Regarding the efficiency of either retrograde or antegrade perfusion, although there are conflicting opinions, the best choice depends on the experimental set-up[69-71].

Our group established a retrograde perfusion protocol, which is suitable for the use with OTC and microscopic analysis[53]. It allows the circulation of the dye in all the organs of the body so that it becomes possible to stain and harvest all organs in one run. One of the most important advantages of this method is the strong reduction of the number of animals used in the experiments, as it becomes possible to use all organs in one single go and to comply with the 3Rs animal research principle (Replacement, Reduction and Refinement)[72].

Moreover, the pressure and the perfusate volume, kept constant by the use of a compressor and a syringe pump, assure the optimal quality of the samples. For a mouse, the amount of dye, injected per minute, was set to be 1ml; this is quite in accordance with Langendorff's procedure, who, initially, had set the amount of the perfusate, for a mouse, at 2ml/min[68].

Also, the retrograde way of perfusing is applicable to different strains of animals, such as mouse, rat, rabbit[69]. Lastly, the efficiency of our protocol is given also by the economy of the equipment, as well as the rapidity by which it is performed. In fact, for a mouse, without considering the dye injection, the whole procedure would take only 12 minutes (6 min. for saline and 6 min. for 4%PFA).

## 5.2. Main differences between the original and optimized ECi-based OTC

This paragraph illustrates the main differences between the two ECi/based protocols.

Firstly, the shrinkage rate: as indicated in Figures 4.32, 4.33, 4.34, the shorter dehydration of the optimised protocol, although stronger, reduces, with some exceptions, the shrinkage rate in terms of weight, area and volume of the tissues.

An eventual event of shrinkage/swelling, after a general OTC procedure, could affect the integrity of the inner structures and, consequently, the quality of the imaging. This is the reason why a good OTC protocol should not provoke a pronounced shrinkage or expansion. Although avoiding completely this phenomenon is not possible, it is however crucial to minimize it. The different organs present unique properties of swelling/shrinking[73].

The shrinkage studies conducted indicate that in terms of weight, the organs under discussion lost more weight after the ECi-based OTC described by Klingberg[52] as well as in our optimised protocol. The different concentrations and timing for each ethanol step, in the two different protocols, play an important role. The incubation time for each passage in ethanol, described by Klingberg and coworkers, lasts 4 hours at 4°C [52]. Indeed, in our optimised protocol, each ethanol step lasts only 45 minutes. Moreover, skipping one step reduces the risk of a pronounced shrinkage. The only exception regards the lung, which seems to gain weight after both procedures and that could be explained by its soft and sponge-like structure, which could enhance the gain of weight by absorbing solutions[73], causing a swelling phenomenon. This is also confirmed from the surface area evaluation: if after our protocol, the lung seems to loose almost 60% in surface, after the original one, the gain in surface is roughly of 50%. Once again, due to its structure, the ethanol timing could have provoked a bigger absorption and, consequently, an increase of the surface.

A different trend has been described for the changes in volume in heart, kidney and liver. The optimized protocol seems to have provoked less shrinkage compared to the original protocol, although for lung and spleen the situation seems to be the opposite. In addition, the comparison performed on the amount of lipids extracted, before and after both the ECi-based OTC protocols, revealed no significant differences: both the procedures remove lipids with

the same efficacy. As already mentioned, lipids from cell membranes are one of the most prominent causes of light scattering, which should be removed in order to reach a good quality in OTC. Moreover, membrane-associated lipids are characterized by hydrogen bonds, electrostatic and hydrophobic interactions, which allow them to be linked to membrane-associated proteins[67]. Due to this chemical architecture, the most suitable way of extraction is the use of polar solvents, as ethanol or methanol, in order to disrupt these types of chemical bonds[67]. Another important parameter to take into account is the temperature by which the lipid extraction occurs. To achieve an optimal rate of extracted lipids, the temperature should be kept at RT or even lower, whenever required[67].

In terms of quality of imaging, we can state that the optimized procedure improved and ameliorated the previous one, making it available even for other different aims.

## 5.3. Stability of the dye

As demonstrated by Figures 4.35, 4.36, 4.37, long time storage (years) of the samples in ECi affects only partially the fluorescence of the dyes. This is in contrast, for instance, to the 3DISCO, where one of the drawbacks is given by a fast degradation of the fluorescent signal due to the clearing solution. Because of that, the sample should be imaged as soon as possible after the clearing [21]. Our findings are in accordance with Klingberg's protocol[52]. Considering also the use of different dyes (nanoparticles, WGA Alexa Fluo 488 conjugated, H&E), the evidence is that a) many and different dyes may be perfused accordingly to our protocol which guarantees their survival; b) a long storage in ECi affects only partially the fluorescence of the dyes perfused, allowing a second imaging even after two years. This could give the opportunity to create archives of cleared tissues, suitable for long-term studies, without sacrificing a big number of animals (even when not necessarily needed), in accordance with the 3Rs animal research principle[72].

## 5.4. Imaging

In the imaging context, all the parameters were tailored, in order to acquire the best 3D image possible. First of all, samples <u>RI correction</u>: in order to achieve the optimal RI matching between the samples and the mounting media, the cleared specimens were stored in the chosen mounting medium for 24-48 hours before the imaging (except for the ECi), in the same microscope environment at RT. This was important, as the RIs of the most used mounting media were evaluated at temperatures near to RT: immersion oil (R.I.1.518 at

23°C), 88% glycerol (R.I.1.475 at 20°C[55]) and ECi (R.I. 1.558 at 25°C[57]). These 2 precautions contributed to an optimal matching of the diverse RIs.

Another important aspect was the <u>choice of the dyes and/or fluorochromes</u>. Although very different in their mode of operation, the two microscopes (CM or LSM) have some parameters in common, to be taken in consideration. In fact, in case of a double or multiple staining, it is important to choose dyes with well-separated excitation and emission spectra, to avoid overlapping and, thus, cross-talk[74]. For this reason, in our experiments, when a multiple staining was required, dyes with distinct spectra were used, such as Cy-7-PEI in combination with WGA-AlexaFluo 488 conjugated or for the 3D-IHC, AlexaFluo 647 in combination with Sytox Green. To avoid the overlapping and cross-talk phenomena a NIR and green region dyes were used. Additionally, to further bypass that, in case of double staining, a <u>sequential scanning</u> was used[75].

As already explained, immersion oil was used as mounting solution, for confocal analysis. This helped in:

a) Circumventing the risk of ECi evaporation, caused by the long timing if imaging on CM. Due to that, as substitute of ECi, a mounting solution with a similar value of RI was required. In fact, the RIs mismatch between the clearing and mounting solutions results in a very strong reduction of axial resolution, where one of the worst consequences is the distortion of the z-axis and, therefore, loss of structural data[75-77]. In addition, the achievement of the best resolution (in terms of optical aberrations and out-of-focus, which may negatively affect the signal-to-noise ratio) is only possible by working in a very homogeneous RI environment[78];

b) enhancing both the optical transparency and, consequently, the axial resolution, as recently demonstrated by Fouquet and co-workers[76]. According to them, the use of high RIs (≥1.5) is considered much better for achieving a very good quality of tissue transparency and for the improvement of the axial resolution in the imaging[76].

On the other hand, for LSM analysis, a change in the mounting solution was not necessary. The speed of imaging of this microscope allowed us to use ECi, even as mounting solution, without facing the danger of a quick evaporation and a RI mismatch.

In order to prevent the z-axis distortion also the way of placing the sample on a specific support should be considered. To image the samples by CM, a 60mm Petri dish was chosen. This was completely filled with immersion oil and the organ anchored in the center of the dish, by a needle and adhesive paste. In this way, the sample was held securely, unable to move, allowing the perfect imaging of all the axes, especially of the z-axis, without losing structural data and information.

For this purpose and considering also the hardware of the Light Sheet (for example the space between the mirrors and their orientation as well as the working distance of the objective), the placing of the sample was an essential step to prevent the out-of-focus and the consequences of this. So, any sample was placed in a glass bottom Petri dish. Thanks to this glass bottom, it was possible to avoid the eventual corrosion of the standard plastic dish caused by ECi. In addition, to prevent the breaking of the dish, the specimen was used to be pasted on a little piece of parafilm. This helped in raising the organ up, without affecting the matching of the RIs. All of these experimental conditions assured a successful imaging.

Lastly, for both microscopes, the acquisition settings were established in a way to reduce the time of acquisition, without influencing the quality of the final result. However, the acquisition time depends also on several other criteria, such as the number of tiles (marked by the stage overview option, tool of Las-X software), the depth (z-size) assigned as well as the type of objective used. For instance, the acquisition time, from CM, for a sample of 25 tiles and 446.53µm of z-size, imaged by a 20x objective, lasted 90 minutes. Due to all of these criteria, the acquisition time represents a very variable parameter. In addition to that, in every single experiment, the laser intensity, pinhole and the choice of the depth to be imaged had to be adjusted in order to prevent pixel oversaturation or low signal, which could have otherwise diminished the quality of the pictures[74].

Moreover, the LSM settings required also to optimize the binning value, defined as a process by which the signals from close pixels are combined into one value[74]. A small binning value results in a phenomenon known as "oversampling", which may prolong the acquisition time and increase the risk of photobleaching of the specimen[74]. Another problem is in the amount of generated data, which strongly increases when a small binning value is used. In fact, for a high resolution (no binning) tile scan, made by both mirrors, the range of generated data was between ~300 and ~600 GB. Indeed, by reducing the resolution to 2*2 binning, the data amount for a both mirrors tile scan was estimated to be in medium range of 100 GB (in some cases, even less). These data refer to tile scan of mouse pole kidney and mouse spleen.

Similarly to what happens for the confocal imaging, the acquisition time is dependent on these working conditions. For instance, the imaging of the pole of a mouse kidney (corresponding to 1/3 of the whole organ), with the highest resolution, two different channels and both mirrors, total depth 1.5mm, lasted 2 hours and 20 minutes, plus some additional time for the merging step. On the other hand, the imaging of the same sample, at the same conditions as before, with a lower resolution (2*2 binning), lasted 1 hour less, plus some additional time for the merging step. Considering that, a 2*2 binning value, in combination

with a 600Hz of speed of imaging, was established as optimal value to guarantee a good imaging in a reasonable time and amount of generated data.

## 5.5. Analysis of pathological samples

In order to extend our protocol on the diagnostic field, some pathological rat kidneys were cleared and imaged. The two pathologies investigated were cisplastin and genetic PCK nephrotoxicity.

Cisplatin is a chemotherapeutic drug used in the treatment of a wide variety of neoplasias[49, 79]. The nephrotoxicity induced by cisplatin has been recognized and evaluated since its introduction[80]. The consequences of cisplatin-induced AKI and CKI were discovered both on molecular and histological levels[49, 79, 80]. The 2D and 3D images acquired from these specimens confirm the presence of cisplatin-induced AKI, especially in terms of as tubular dilatation and inflammatory infiltrate, clear signs of injury. Moreover, considering the injection time (the perfusion occurred 14 days after the first cisplatin injection), these findings are also in accordance with data of other authors, who stated to have found all of these symptoms after the fourth day of the injection, more and more increasing until six months later[49].

Also the imaging of PCK rat kidney confirmed what was described by Wilson and co-workers[50, 51].

Therefore, it is possible to ascertain that our protocol is able to distinguish among physiologic and pathologic animal samples. Hence, this could become a useful tool also for human diagnostic field.

## 5.6. "Re-vitalization" of histology samples from paraffin blocks

We found that it is possible to re-vitalize even samples from 20 years old paraffin blocks, giving the opportunity to re-use the old paraffin blocks as archives of structural information.

Recent publications have highlighted that liquid paraffin might play a very important role in OTC[81, 82]. Considering also its RI, which is equal to 1.4691+0.0003 at 20°C[81], it has been possible to create a mixture 1:1 of liquid paraffin and glycerol (RI: 1.475+0.0003 at 20°C), which worked as optical reagent, in order to clear both fresh and de-paraffinised tissues[81, 82]. Furthermore it has been clarified how mixtures between lipophilic and hydrophilic substances could improve the OTC, in a synergic way, as liquid paraffin enhances the glycerol penetration into the tissues[82] and, in the meantime, glycerol acts as optical clearing reagent. In

addition, glycerol can reduce the discontinuity in the RIs, improving the quality of the OTC and, blocking the evaporation of water, which prevents the tissue shrinkage[81]

In our group, a method to "re-vitalize" and clear the old paraffin blocks, including de-paraffinization in xylene, dehydration and clearing in ECi, has been established. In addition, this method has been also automated, by using the Leica EMTP, which can easily be programmed. With that, it is possible to de-paraffinize and clear in one run old samples and use the autofluorescence as an alternative staining, in order to visualize inner structures. Kidney, lung, heart from ADPCK rats were treated and microscopically analyzed, obtaining promising results: in fact, blood vessels with erythrocytes inside were clearly visible. Even paraffin embedded human renal biopsies were treated in this way: the complexity of the human morphology might cause a wider light-scattering[81]. However, the re-vitalization of old paraffin blocks might provide a solution in order to clarify those dubious pathologic situations and make more accurate diagnosis, which could not be done by using only standard histology and slides of a few μm[82]. Additionally, paraffin-embedded archives could also be used in order to intensify the field of research. This is especially true if data integration centers are build up (BMBF funding) and deep learning techniques are used.

Another big advantage of this technique is the use of label-free samples: the use of autofluorescence as alternative staining could give the opportunity to visualize 3D tissue architecture and to easily differentiate between healthy and pathological situations[82] . Moreover, it would be also possible to use the autofluorescence from erythrocytes to track and follow the blood vessels.

## 5.7. ECi-OTC and 3D immunohistochemistry (3D-IHC)

Another important step onwards has been the establishment of a 3D-IHC protocol, after the removal of ECi during a rehydration step.

Compared to the previous procedure, where the antibody was injected intravenously in mice, during their sacrifice[52], in our lab a method to remove the ECi from samples using a rehydration step was developed, allowing the staining of renal glomeruli as well as epithelial cell nuclei. There are many advantages in using this procedure:

1) In the original protocol, more generic antibodies were used, such as CD11 and CD31[52], in order to allow them to be spread in the whole mouse body before the perfusion. With our method it is possible to fine stain single structures, as the renal glomeruli, with a more specific antibody, as, in our case, the one against nephrin.

The large amount of solutions and the duration required for the whole procedure was identified as drawbacks for this staining: in reality, these two aspects assure both the specificity of the staining and a low level of background and noise.

Furthermore, all the steps of our procedure are easy to handle, without using harmful substances;

2) Despite some changing in the color, after the ECi removal and the following rehdration (as reported in Fig. 4.46), this process does not reduce the efficacy of the tissue clearing. In fact, the color of the samples, after the rehydration remains the one that the samples have immediately after the perfusion, which is due to the re-gain of water. The crucial point is the loss of the lipids after the clearing process: despite the re-gain of water, the optical transparency of the tissues does not change. Moreover, the rehydration step enhances the efficiency of the 3D-IHC, which could not be performed in the lipophilic ECi environment;

3) In the imaging context, coming back to the aqueous RIs provides the opportunity to use a more versatile mounting solution, such as glycerol. In fact, given its more compatibility with different objectives, it is possible to facilitate the imaging procedure, without using an objective with a specific RI, as it is needed for ECi.

Additionally, the preliminary incubation into glycerol, prior to the imaging, does not only permit a better RIs matching, but also a better diffusion of the mounting solution, which is reflected in clearer and sharper final results;

4) The reversibility of ECi-based clearing process has also been proven, by following this new protocol. That means it is possible to optically clear samples with ECi and keep the efficacy of the clearing, although it is removed and "substituted" with other solutions.

As reported in Figure 4.47, after the rehydration step, a little expansion of the tissue was noticed. However, the structures of interest appeared not affected by the ECi removal with the rehydration step. Also, this increase, combined with the use of the 63x objective helped in defining microstructures such as, for instance, the foot processes in the glomeruli. As conclusion, it is possible to state that: 1) the rehydration phase does not provoke a wide enlargement of the structures, so that it is possible to stain them without facing this issue; 2) this protocol could also be used for all the specimens that cannot be perfused, as, for instance, human samples from biopsies.

In addition, with this new protocol, we also proved the reversibility of the ECi-based OTC.

# 6. Summary

OTC defines a large group of techniques, aiming to make the tissues optically transparent, in order to be microscopically analysed. This is considered an important tool in the progress of the biology, as with that it is possible to reconstruct in 3D physiologic and pathological processes at different levels, from whole animals, organs down to a subcellular level.

The optical transparency is an important pre-requisite to achieve the 3D reconstruction. Every living specimen is characterized by a set of highly light-absorbing molecules, where the most important are considered the blood molecules (haemoglobin, myoglobin), which provoke the autofluorescence phenomenon that may negatively interfere with the microscopic analysis. Another important class of biomolecules considered to be a negative factor for the OTCs are the bilayer membrane associated lipids. In fact, these molecules, together with other components, contribute to create the milky and opaque appearance, which does not allow an effective 3D imaging. In addition, due to their chemical structure, these molecules enhance the event of light scattering. In order to reduce as much as possible this combination of factors and to reach the optical transparency and, thus, make the 3D imaging possible, the main principle of OTCs is to remove lipids from the sample. However, in order to reduce also the autofluorescence phenomenon, a preliminary action is often required, that is the perfusion aiming to remove blood (and, therefore, blood molecules) from the body of the animal. Additionally, one of the most important parameter to take into account is the RI of the different solutions, as it also defines the quality of the 3D imaging. In fact, as the OTCs are based on the use of clearing solutions and the 3D imaging on mounting solutions where the different objectives are immersed in, the perfect matching of both RIs is of primary importance, to obtain images with high resolution. Actually, clearing solutions with high RIs are considered optimal, as these can match better with the RIs of biomolecules.

Our OTC approach is divided into three steps: a pre-processing, that is the perfusion (removal of blood and staining of all organs), the OTC processing and the post-processing, as the microscopic analysis.

Our work aimed at the optimization of all the three steps. In fact, we worked in order to: 1) speed up the perfusion procedure. Moreover, our perfusion approach works in a way that is possible to stain all the body of the animal in one run, so that the collection and harvesting of all organs becomes easier. This also helps in reducing the number of animals used for *in vivo* experiments; 2) optimize a pre-existent ECi-based OTC[52]. ECi is a lypophylic solution, with high RI, that can better match with the RI of biomolecules. Our optimization consisted in

accelerating all the procedures and automating them, using a tissue processor, which allows the run of multiple samples in one go; 3) optimize the settings of the imaging in terms of samples mounting, image acquisition time and amount of generated data.

By optimizing all three steps, it was possible to establish an entirely new process also suitable for different and many samples (from mouse, rat, until human samples).

Although many dyes were tested, the most used staining was the Cy7-PEI, a dye previously synthetized at the ZMF department of the Universitäts Klinikum of Mannheim, Germany. This was injected during the perfusion, in order to fluorescently stain and to microscopically detect fine structures, such as renal glomeruli and blood vessels.

The optimized clearing procedure was amply tested, before going on and implementing that, in order to make that available also for other studies, such as the "re-vitalization" and further analysis of old histology samples from paraffin blocks as well as for 3D-IHC. Especially this latter implementation proved that the ECi-based OTC is a reversible process, as the 3D-IHC was preceeded by a removal of the ECi by a rehydration step and we demonstrated that this did not affect the quality of the clearing and, also, further staining and analysis were possible.

Compared to other OTCs, our ECi optimization was safer, as ECi is a no-toxic reagent, faster, since the whole procedure takes 4 hours (although the samples may stay longer in the solution) and cheaper, especially concerning the price of the ECi for 1 liter.

# 7. References

1. Ariel, P: A beginner's guide to tissue clearing. *Int J Biochem Cell Biol,* 84**:** 35-39, 2017.

2. Richardson, DS, Lichtman, JW: Clarifying Tissue Clearing. *Cell,* 162**:** 246-257, 2015.

3. Yu, T, Qi, Y, Gong, H, Luo, Q, Zhu, D: Optical clearing for multiscale biological tissues. *J Biophotonics,* 11**:** 170-187, 2018.

4. Seo, J, Choe, M, Kim, SY: Clearing and Labeling Techniques for Large-Scale Biological Tissues. *Mol Cells,* 39**:** 439-446, 2016.

5. Toga, AW, Goldkorn, A, Ambach, K, Chao, K, Quinn, BC, Yao, P: Postmortem cryosectioning as an anatomic reference for human brain mapping. *Comput Med Imaging Graph,* 21**:** 131-141, 1997.

6. Oh, SW, Harris, JA, Ng, L, Winslow, B, Cain, N, Mihalas, S, Wang, Q, Lau, C, Kuan, L, Henry, AM, Mortrud, MT, Ouellette, B, Nguyen, TN, Sorensen, SA, Slaughterbeck, CR, Wakeman, W, Li, Y, Feng, D, Ho, A, Nicholas, E, Hirokawa, KE, Bohn, P, Joines, KM, Peng, H, Hawrylycz, MJ, Phillips, JW, Hohmann, JG, Wohnoutka, P, Gerfen, CR, Koch, C, Bernard, A, Dang, C, Jones, AR, Zeng, H: A mesoscale connectome of the mouse brain. *Nature,* 508**:** 207, 2014.

7. Tsai, PS, Blinder, P, Migliori, BJ, Neev, J, Jin, Y, Squier, JA, Kleinfeld, D: Plasma-mediated ablation: an optical tool for submicrometer surgery on neuronal and vascular systems. *Current opinion in biotechnology,* 20**:** 90-99, 2009.

8. Toga, AW, Ambach, KL, Schluender, S: High-resolution anatomy from in situ human brain. *NeuroImage,* 1**:** 334-344, 1994.

9. Tuchin, VV: Tissue Optics and Photonics: Light-Tissue Interaction. *J Biomed Photonics Eng,* 1**:** 98-134, 2015.

10. P. Bolin, F, E. Preuss, L, C. Taylor, R, J. Ference, R: Refractive index of some mammalian tissue using fiber optic cladding method. *Appl Opt,* 28**:** 2297-2303, 1989.

11. Spalteholz, WJH, Leipzig: Uber das Durchsichtigmachen von menschlichen und tierischen Praparaten (About the transparency of human and animal preparations), S. 1914.

12. Silvestri, L, Costantini, I, Sacconi, L, Pavone, FS: Clearing of fixed tissue: a review from a microscopist's perspective. *J Biomed Opt,* 21**:** 1-8, 8, 2016.

13. Meglinski, I, Churmakov, DY, Bashkatov, A, Genina, E, Tuchin, V: The Enhancement of Confocal Images of Tissues at Bulk Optical Immersion. *Laser Phys,* 13**:** 65-69, 2003.

14. Kuwajima, T, Sitko, AA, Bhansali, P, Jurgens, C, Guido, W, Mason, C: ClearT: a detergent- and solvent-free clearing method for neuronal and non-neuronal tissue. *Development,* 140**:** 1364-1368, 2013.

15. Ke, MT, Fujimoto, S, Imai, T: SeeDB: a simple and morphology-preserving optical clearing agent for neuronal circuit reconstruction. *Nat Neurosci,* 16**:** 1154-1161, 2013.

16. Costantini, I, Ghobril, JP, Di Giovanna, AP, Allegra Mascaro, AL, Silvestri, L, Mullenbroich, MC, Onofri, L, Conti, V, Vanzi, F, Sacconi, L, Guerrini, R, Markram, H, Iannello, G, Pavone, FS: A versatile clearing agent for multi-modal brain imaging. *Sci Rep,* 5**:** 9808, 2015.

17. Yang, B, Treweek, JB, Kulkarni, RP, Deverman, BE, Chen, CK, Lubeck, E, Shah, S, Cai, L, Gradinaru, V: Single-cell phenotyping within transparent intact tissue through whole-body clearing. *Cell,* 158**:** 945-958, 2014.

18. Hou, L, Marsh, JH: 1.55 μm DFB laser monolithically integrated with 3-stage power amplifier array. *2015 IEEE High Power Diode Lasers and Systems Conference (HPD).* 2015 pp 19-20.

19. Chiang, A-S, Lin, W-Y, Liu, H-P, Pszczolkowski, MA, Fu, T-F, Chiu, S-L, Holbrook, GL: Insect NMDA receptors mediate juvenile hormone biosynthesis. *Proc Natl Acad Sci U S A,* 99**:** 37-42, 2002.

20. Hou, B, Zhang, D, Zhao, S, Wei, M, Yang, Z, Wang, S, Wang, J, Zhang, X, Liu, B, Fan, L, Li, Y, Qiu, Z, Zhang, C, Jiang, T: Scalable and DiI-compatible optical clearance of the mammalian brain. *Front Neuroanat,* 9**:** 1-11, 2015.

21. Ertürk, A, Becker, K, Jahrling, N, Mauch, CP, Hojer, CD, Egen, JG, Hellal, F, Bradke, F, Sheng, M, Dodt, HU: Three-dimensional imaging of solvent-cleared organs using 3DISCO. *Nat Protoc,* 7**:** 1983-1995, 2012.

22. Susaki, EA, Tainaka, K, Perrin, D, Kishino, F, Tawara, T, Watanabe, TM, Yokoyama, C, Onoe, H, Eguchi, M, Yamaguchi, S, Abe, T, Kiyonari, H, Shimizu, Y, Miyawaki, A, Yokota, H, Ueda, HR: Whole-brain imaging with single-cell resolution using chemical cocktails and computational analysis. *Cell,* 157**:** 726-739, 2014.

23. Hama, H, Kurokawa, H, Kawano, H, Ando, R, Shimogori, T, Noda, H, Fukami, K, Sakaue-Sawano, A, Miyawaki, A: Scale: a chemical approach for fluorescence imaging and reconstruction of transparent mouse brain. *Nat Neurosci,* 14**:** 1481-1488, 2011.

24. Chung, K, Deisseroth, K: CLARITY for mapping the nervous system. *Nat Methods,* 10**:** 508-513, 2013.

25. Tomer, R, Ye, L, Hsueh, B, Deisseroth, K: Advanced CLARITY for rapid and high-resolution imaging of intact tissues. *Nat Protoc,* 9**:** 1682-1697, 2014.

26. Marx, V: Optimizing probes to image cleared tissue. *Nat Methods,* 13**:** 205, 2016.

27. Petty, HR: Fluorescence microscopy: established and emerging methods, experimental strategies, and applications in immunology. *Microsc Res Tech,* 70**:** 687-709, 2007.

28. Stockert, JC, Blazquez-Castro, A: *Fluorescence Microscopy in Life Sciences*, Bentham, 2017.

29. Sanderson, MJ, Smith, I, Parker, I, Bootman, MD: Fluorescence microscopy. *Cold Spring Harb Protoc,* 10, 2014.

30. Reichman, J: *Handbook of optical filters for fluorescence microscopy.* 2000. Online: https://loci.wisc.edu/sites/default/files/2016-09/HandbookofOpticalFilters, CHROMA TECHNOLOGY CORP; Stand: 2012

31. Ragazzi, M, Piana, S, Longo, C, Castagnetti, F, Foroni, M, Ferrari, G, Gardini, G, Pellacani, G: Fluorescence confocal microscopy for pathologists. *Mod Pathol,* 27**:** 460-471, 2014.

32. Hell, SW: Toward fluorescence nanoscopy. *Nat Biotechnol,* 21**:** 1347, 2003.

33. Huisken, J, Stainier, DYR: Selective plane illumination microscopy techniques in developmental biology. *Development,* 136**:** 1963-1975, 2009.

34. Keller, PJ, Schmidt, AD, Wittbrodt, J, Stelzer, EHK: Reconstruction of Zebrafish Early Embryonic Development by Scanned Light Sheet Microscopy. *Science (New York, NY),* 322**:** 1065-1069, 2008.

35. Keller, PJ, Ahrens, MB, Freeman, J: Light-sheet imaging for systems neuroscience. *Nat Methods,* 12**:** 27, 2014.

36. Taormina, MJ, Jemielita, M, Stephens, WZ, Burns, AR, Troll, JV, Parthasarathy, R, Guillemin, K: Investigating bacterial-animal symbioses with light sheet microscopy. *Biol Bull,* 223**:** 7-20, 2012.

37. Desgrange, A, Cereghini, S: Nephron Patterning: Lessons from Xenopus, Zebrafish, and Mouse Studies. *Cells,* 4**:** 483-499, 2015.

38. Denic, A, Lieske, JC, Chakkera, HA, Poggio, ED, Alexander, MP, Singh, P, Kremers, WK, Lerman, LO, Rule, AD: The Substantial Loss of Nephrons in Healthy Human Kidneys with Aging. *J Am Soc Nephrol,* 28**:** 313-320, 2017.

39. Pollak, MR, Quaggin, SE, Hoenig, MP, Dworkin, LD: The glomerulus: the sphere of influence. *Clin J Am Soc Nephrol,* 9**:** 1461-1469, 2014.

40. Rodriguez, ER, Tan, CD: Structure and Anatomy of the Human Pericardium. *Prog Cardiovasc Dis,* 59**:** 327-340, 2017.

41. Braunwald, E: Structure and function of the normal myocardium. *Br Heart J,* 33**:** 3-8, 1971.

42. Fiocca, S, Netter, FH: *Fondamenti di anatomia e fisiologia umana,* Napoli, Sorbona, 1990.

43. Schittny, JC: Development of the lung. *Cell Tissue Res,* 367**:** 427-444, 2017.

44. Tomashefski, JF, Farver, CF: Anatomy and Histology of the Lung. In: *Dail and Hammar's Pulmonary Pathology.* Springer, 2008, pp 20-48.

45. Elias, H, Bengelsdorf, H: The structure of the liver of vertebrates. *Cells Tissues Organs,* 14**:** 297-337, 1952.

46. Abdel-Misih, SR, Bloomston, M: Liver anatomy. *Surg Clin North Am,* 90**:** 643-653, 2010.

47. Kmiec, Z: Cooperation of Liver Cells in Health and Disease. *Adv Anat Embryol Cell Biol,* 161**:** III-XIII, 1, 2001.

48. Mebius, RE, Kraal, G: Structure and function of the spleen. *Nat Rev Immunol,* 5**:** 606, 2005.

49. Sharp, CN, Doll, MA, Megyesi, J, Oropilla, GB, Beverly, LJ, Siskind, LJ: Subclinical kidney injury induced by repeated cisplatin administration results in progressive chronic kidney disease. *Am J Physiol Renal Physiol,* 315**:** 161-172, 2018.

50. Wilson, P: Polycystic Kidney Disease. *N Engl J Med,* 350**:** 151-164, 2004.

51. Wilson, P, Falkenstein, D: *The Pathology of Human Renal Cystic Disease,* Berlin, Heidelberg, 1995.

52. Klingberg, A, Hasenberg, A, Ludwig-Portugall, I, Medyukhina, A, Mann, L, Brenzel, A, Engel, DR, Figge, MT, Kurts, C, Gunzer, M: Fully Automated Evaluation of Total Glomerular Number and Capillary Tuft Size in Nephritic Kidneys Using Lightsheet Microscopy. *J Am Soc Nephrol,* 28**:** 452-459, 2017.

53. Huang, J, Brenna, C, Khan, AuM, Daniele, C, Rudolf, R, Heuveline, V, Gretz, N: A cationic near infrared fluorescent agent and ethyl-cinnamate tissue clearing protocol for vascular staining and imaging. *Sci Rep,* 9**:** 521, 2019.

54. Wang, Y, Zhang, DH, Zhang, JY, Chen, N, Zhi, GY: High-yield synthesis of bioactive ethyl cinnamate by enzymatic esterification of cinnamic acid. *Food Chem,* 190**:** 629-633, 2016.

55. Lide, DR: CRC Handbook of Chemistry and Physics, 88th ed Editor-in-Chief. *J Am Chem Soc,* 130**:** 382-382, 2008.

56. Hecht, E: *Optics*, Addison-Wesley, 2002.

57. Krauter, P, Nothelfer, S, Bodenschatz, N, Simon, E, Stocker, S, Foschum, F, Kienle, A: Optical phantoms with adjustable subdiffusive scattering parameters. *J Biomed Opt,* 20**:** 1-10, 10, 2015.

58. Monsigny, M, Roche, AC, Sene, C, Maget-Dana, R, Delmotte, F: Sugar-Lectin Interactions: How Does Wheat-Germ Agglutinin Bind Sialoglycoconjugates? *Eur J Biochem,* 104**:** 147-153, 1980.

59. Titford, M: The long history of hematoxylin. *Biotech Histochem,* 80**:** 73-78, 2005.

60. Kay, AB: The early history of the eosinophil. *Clin Exp Allergy,* 45**:** 575-582, 2015.

61. Araujo, LMGd, Serigiolle, LC, Gomes, HMP, Rodrigues, DAB, Lopes, CM, Leme, PLS: Volume calculation of rats' organs and its application in the validation of the volume relation between the abdominal cavity and the hernial sac in incisional hernias with "loss of abdominal domain" *Arq Bras Cir Dig,* 27**:** 177-181, 2014.

62. Dickie, R, Bachoo, RM, Rupnick, MA, Dallabrida, SM, DeLoid, GM, Lai, J, DePinho, RA, Rogers, RA: Three-dimensional visualization of microvessel architecture of whole-mount tissue by confocal microscopy. *Microvasc Res,* 72**:** 20-26, 2006.

63. Gleave, JA, Lerch, JP, Henkelman, RM, Nieman, BJ: A Method for 3D Immunostaining and Optical Imaging of the Mouse Brain Demonstrated in Neural Progenitor Cells. *PLoS One,* 8**:** 72039, 2013.

64. Bhatia, SP, Wellington, GA, Cocchiara, J, Lalko, J, Letizia, CS, Api, AM: Fragrance material review on ethyl cinnamate. *Food Chem Toxicol,* 45**:** 90-94, 2007.

65. Nojima, S, Susaki, EA, Yoshida, K, Takemoto, H, Tsujimura, N, Iijima, S, Takachi, K, Nakahara, Y, Tahara, S, Ohshima, K, Kurashige, M, Hori, Y, Wada, N, Ikeda, J-i, Kumanogoh, A, Morii, E, Ueda, HR: CUBIC pathology: three-dimensional imaging for pathological diagnosis. *Sci Rep,* 7**:** 9269, 2017.

66. Lee, E, Choi, J, Jo, Y, Kim, JY, Jang, YJ, Lee, HM, Kim, SY, Lee, H-J, Cho, K, Jung, N, Hur, EM, Jeong, SJ, Moon, C, Choe, Y, Rhyu, IJ, Kim, H, Sun, W: ACT-PRESTO: Rapid and consistent tissue clearing and labeling method for 3-dimensional (3D) imaging. *Sci Rep,* 6**:** 18631, 2016.

67. Work, TS, Work, E: Chapter 3 Lipid extraction procedures. In: *Laboratory Techniques in Biochemistry and Molecular Biology.* edited by COMPANY, N.-H. P., Elsevier, 1972, pp 347-353.

68. Langendorff, O: Untersuchungen am überlebenden Säugethierherzen. *Arch Gesamte Psychol,* 61**:** 291-332, 1895.

69. Bell, RM, Mocanu, MM, Yellon, DM: Retrograde heart perfusion: The Langendorff technique of isolated heart perfusion. *J Mol Cell Cardiol,* 50**:** 940-950, 2011.

70. Omatsu-Kanbe, M, Yoshioka, K, Fukunaga, R, Sagawa, H, Matsuura, H: A simple antegrade perfusion method for isolating viable single cardiomyocytes from neonatal to aged mice. *Physiolo Rep,* 6**:** 1-9, 2018.

71. Yerlioglu, ME, Wolfe, D, Mezrow, CK, Weisz, DJ, Midulla, PS, Zhang, N, Shiand, HH, Bodian, C, Griepp, RB: The effect of retrograde cerebral perfusion after particulate embolization to the brain. *J Thorac Cardiovasc Surg,* 110**:** 1470-1485, 1995.

72. Russell, WMS, Burch, RL, Hume, CW: *The principles of humane experimental technique*, Methuen London, 1959.

73. Kim, JH, Jang, MJ, Choi, J, Lee, E, Song, K-D, Cho, J, Kim, K-T, Cha, H-J, Sun, W: Optimizing tissue-clearing conditions based on analysis of the critical factors affecting tissue-clearing procedures. *Sci Rep,* 8**:** 12815, 2018.

74. North, AJ: Seeing is believing? A beginners' guide to practical pitfalls in image acquisition. *J Cell Biol,* 172**:** 9-18, 2006.

75. Hell, S, Reiner, G, Cremer, C, Stelzer, EHK: Aberrations in confocal fluorescence microscopy induced by mismatches in refractive index. *J Microsc,* 169**:** 391-405, 1993.

76. Fouquet, C, Gilles, J-F, Heck, N, Dos Santos, M, Schwartzmann, R, Cannaya, V, Morel, M-P, Davidson, RS, Trembleau, A, Bolte, S: Improving axial resolution in confocal microscopy with new high refractive index mounting media. *PLoS One,* 10**:** 1-9, 2015.

77. Diaspro, A, Federici, F, Robello, M: Influence of refractive-index mismatch in high-resolution three-dimensional confocal microscopy. *Appl Opt,* 41**:** 685-690, 2002.

78. Schermelleh, L, Heintzmann, R, Leonhardt, H: A guide to super-resolution fluorescence microscopy. *J Cell Biol,* 190**:** 165-175, 2010.

79. Perse, M, Veceric-Haler, Z: Cisplatin-Induced Rodent Model of Kidney Injury: Characteristics and Challenges. *Biomed Res Int,* 2018**:** 29, 2018.

80. Miller, RP, Tadagavadi, RK, Ramesh, G, Reeves, WB: Mechanisms of Cisplatin nephrotoxicity. *Toxins (Basel),* 2**:** 2490-2518, 2010.

81. Wang, J, Liang, Y, Zhang, S, Zhou, Y, Ni, H, Li, Y: Evaluation of optical clearing with the combined liquid paraffin and glycerol mixture. *Biomed Opt Express,* 2**:** 2329-2338, 2011.

82. Wilson, JW, Degan, S, Warren, WS, Fischer, MC: Optical clearing of archive-compatible paraffin embedded tissue for multiphoton microscopy. *Biomed Opt Express,* 3**:** 2752-2760,2012

# 8. Curriculum vitae

| Personal information | |
|---|---|
| First name/Surname | **Cinzia Brenna** |
| Date and Place of birth | 27.03.1986, Rome (Italy) |
| Gender | Female |

| Education and training | |
|---|---|
| Date | **June 2016- August 2019** |
| Title of qualification awarded | PhD student at Heidelberg University (DE); PhD Thesis entitled: Optimization of Optical Tissue Clearing Protocols Supervision: Prof. Dr. N. Gretz |
| Date | **October 2010 – July 2013** |
| Title of qualification awarded | Master's Degree in Biotechnologies for medical, pharmaceutical and veterinary diagnostic at Università degli Studi di Basilicata (PZ), Italy. Master Thesis entitled: Extraction and recovery of the soluble protein fraction from the green microalgae Chlorella saccharophila Supervision: Dr. R. Rossano Final mark:110/110 |
| Date | **October 2004 – July 2010** |
| Title of qualification awarded | Bachelor's Degree in Biomedical Biotechnologies at Università degli Studi di Basilicata (PZ), Italy. Bachelor Thesis entitled: Medical and Diagnostic Path of sterile people Supervision: Dr. A. Ostuni; Dr. A. Ferri Final Mark 105/110 |
| Date | **September 1999 – July 2004** |
| Title of qualification awarded | Classic High School Diploma at Liceo Classico "G.Fortunato", Rionero in V. (PZ), Italy Final mark: 96/100 |

| Work experience | |
|---|---|
| Date | **01.06.2016-31.08.2019** |
| Position held | Researcher at Universitäts Klinikum in Mannheim (DE). |
| Date | **01.02.2016-31.05.2016** |
| Position held | Administrative employee at AMA s.r.l. (in house company), Atella (PZ), Italy |

| Further Information | **14-17.09.2017**: Poster presenting and Participation to the International Congress of Nephrology in Mannheim (DE) |
|---|---|
| | **14-25.11.2016**: Participation to the FELLASA COURSE – Laboartory Animal Science- University of Heidelberg DE) |

| Publications and Patents | **24.01.2019:** A cationic near infrared fluorescent agent and ethyl-cinnamate tissue clearing protocol for vascular staining and imaging. J.Huang et al., *Sci Rep*, 9**:** 521, 2019 |
|---|---|
| | **15.06.2018**: Stem/Stromal Cells for Treatment of Kidney Injuries With Focus on Preclinical Models. A.T.Crigna, C.Daniele et al., *Front Med (Lusanne)*, 5:179, 2018 |
| | **07.06.2018**: Publication of the patent "Means and Methods for Visualization of Tissue Structures" (WO 2018/100089) |

# Abbreviations

1) 2D             Two Dimensions;

2) 3D             Three Dimensions;

3) 3D-IHC       3D immunohistochemistry;

4) ACT           Active Clearing Technique;

5) ADPCK       Autosomal Dominant Polycystic Kidney;

6) AKI            Akute Kidney Injury;

7) BABB         Benzyl Alcohol/ Benzyl Benzoate;

8) CKI            Chronic Kidney Injury;

9) CLARITY     Clear Lipid-exchange Acrylamide-hybridized Rigid imaging in situ hybridization-compatible Tissue Hydrogel;

10) CM            Confocal Microscopy;

11) Cy7-PEI (opt)    MHI148-PEI (opt);

12) CUBIC        Clear unobstructed brain imaging cocktails and computational analysis;

13) DBE           Dibenzyl ether;

14) DISCO:       Dimensional Imaging of Solvent-Cleared Organs;

15) DLSM        Digital Scanned Laser Light Sheet Fluorescence Microscopy;

16) ECi           Ethyl Cinnamate;

17) FDA           Food and Drug Administration;

18) FP(s)          Fluorescent Protein(s);

19) GAG          Glycosaminoglycan;

20) GBM          Glomerular Basement Membrane;

21) GFP           Green Fluorescent Protein;

22) H&E           Hematoxylin-Eosin;

23) LSM           Light Sheet Microscopy;

24) NIR            Near Infra-red region of visible spectrum;

25) Opt            Optimized Protocol;

26) Org            Original Protocol;

27) OTC           Optical Tissue Clearing;

28) PACT         Passive Clarity technique;

29) PFA           Paraformaldehyde;

30) PKD          Polycystic Kidney Disease;

| | | |
|---|---|---|
| 31) | PMT | Photomultiplier tube; |
| 32) | RH | Rehydration; |
| 33) | RI | Refractive Index; |
| 34) | RIMS | Refractive Index Matching Solution; |
| 35) | RT | Room Temperature; |
| 36) | SD | Sprague Dawley; |
| 37) | SDS | Sodium Dodecyl Sulphate; |
| 38) | SDS | Scientific data Storage; |
| 39) | SeeDB | See Deep Brain; |
| 40) | THF | Tetrahydrofuran; |
| 41) | WFM | Wide Filed Microscopy; |
| 42) | WGA | Wheat Germ Agglutin; |
| 43) | WT | Wild Type; |
| 44) | ZMF | Zentrum für Medizinische Forschung |

# Acknowledgments